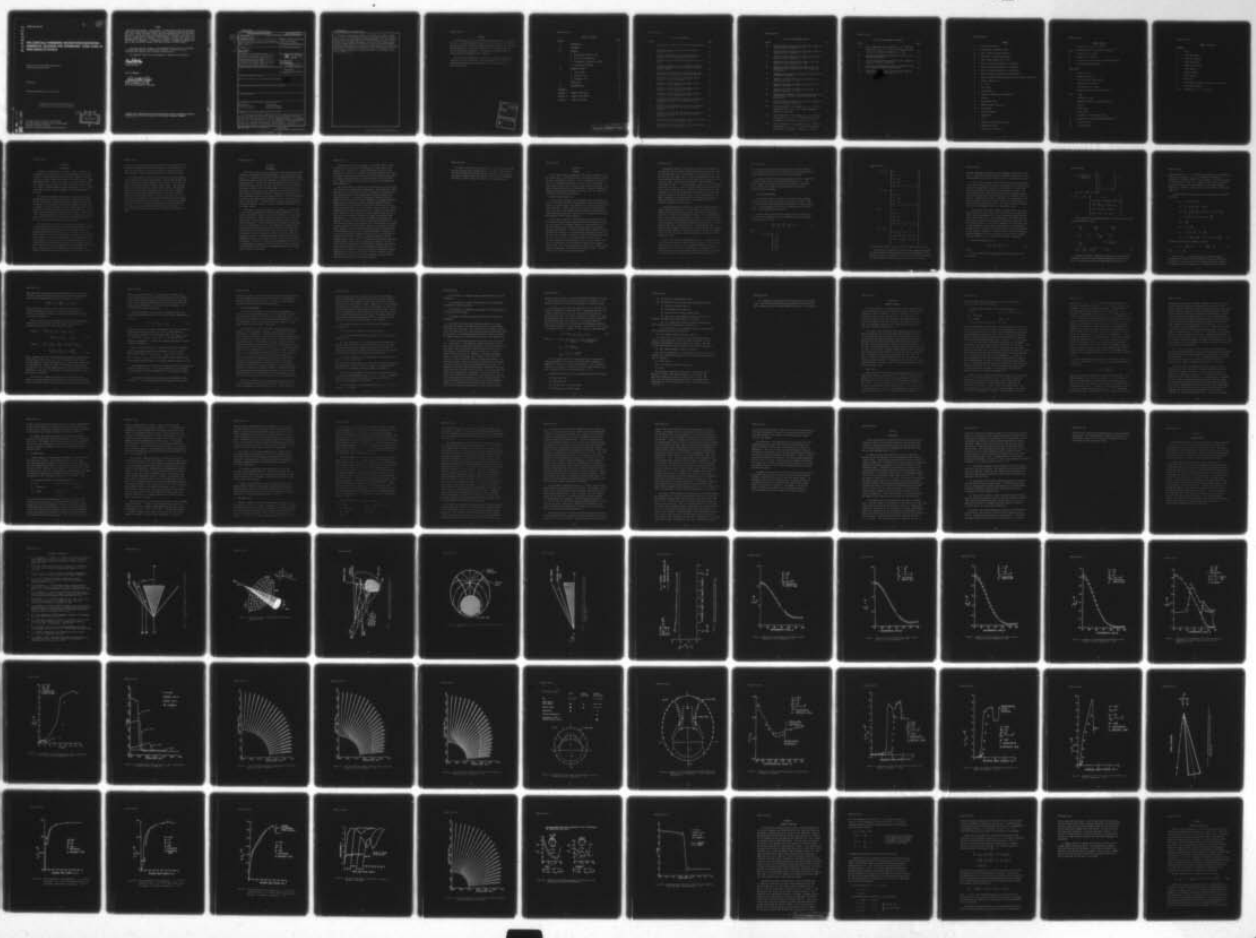
AD-A042 072 AIR FORCE FLIGHT DYNAMICS LAB WRIGHT-PATTERSON AFB OHIO F/G 20/4
THE CONICALLY SYMMETRIC NAVIER STOKES EQUATIONS: NUMERICAL SOLU--ETC(U)
MAR 77 D S MCRAE
AFFDL-TR-76-139

UNCLASSIFIED NL

1 OF 2
ADA042072



AD A042072

AFFDL-TR-76-139

(12)

THE CONICALLY SYMMETRIC NAVIER STOKES EQUATIONS: NUMERICAL SOLUTION FOR HYPERSONIC CONE FLOW AT HIGH ANGLE OF ATTACK

AERODYNAMICS AND AIRFRAME BRANCH
AERO MECHANICS DIVISION

MARCH 1977

TECHNICAL REPORT AFFDL–TR–76–139

Approved for public release; distribution unlimited

DDC FILE COPY

DDC
RECEIVED
JUL 27 1977
F

AIR FORCE FLIGHT DYNAMICS LABORATORY
AIR FORCE WRIGHT AERONAUTICAL LABORATORIES
AIR FORCE SYSTEMS COMMAND
WRIGHT–PATTERSON AIR FORCE BASE, OHIO 45433

NOTICE

When Government drawings, specifications, or other data are used for any purpose other than in connection with a definitely related Government procurement operation, the United States Government thereby incurs no responsibility nor any obligation whatsoever; and the fact that the government may have formulated, furnished, or in any way supplied the said drawings, specifications, or other data, is not to be regarded by implication or otherwise as in any manner licensing the holder or any other person or corporation, or conveying any rights or permission to manufacture, use, or sell any patented invention that may in any way be related thereto.

This report has been reviewed by the Information Office (IO) and is releasable to the National Technical Information Service (NTIS). At NTIS, it will be available to the general public, including foreign nations.

This technical report has been reviewed and is approved for publication.

David D McRae

D. McRAE, Maj., USAF
Project Engineer

FOR THE COMMANDER

Robert D McKelvey

ROBERT D. McKELVEY, Col, USAF
Chief, Aeromechanics Division
Air Force Flight Dynamics Laboratory

Copies of this report should not be returned unless return is required by security considerations, contractual obligations, or notice on a specific document.

AIR FORCE - 14 JUL 77 - 200

UNCLASSIFIED

SECURITY CLASSIFICATION OF THIS PAGE *(When Data Entered)*

REPORT DOCUMENTATION PAGE	READ INSTRUCTIONS BEFORE COMPLETING FORM
1. REPORT NUMBER: AFFDL-TR-76-139	2. GOVT ACCESSION NO. / 3. RECIPIENT'S CATALOG NUMBER
4. TITLE *(and Subtitle)*: The Conically Symmetric Navier Stokes Equations: Numerical Solution for Hypersonic Cone Flow at High Angle of Attack	5. TYPE OF REPORT & PERIOD COVERED: Technical Report. / 6. PERFORMING ORG. REPORT NUMBER
7. AUTHOR(s): David S. McRae, Major, USAF	8. CONTRACT OR GRANT NUMBER(s) / 61102F
9. PERFORMING ORGANIZATION NAME AND ADDRESS: Aerodynamics and Airframe Branch (AFFDL/FXM), Air Force Flight Dynamics Laboratory, Wright-Patterson Air Force Base, OH 45433	10. PROGRAM ELEMENT, PROJECT, TASK AREA & WORK UNIT NUMBERS: Project 230704
11. CONTROLLING OFFICE NAME AND ADDRESS: Aerodynamics and Airframe Branch (AFFDL/FXM), Air Force Flight Dynamics Laboratory, Wright-Patterson Air Force Base, OH 45433	12. REPORT DATE: March 1977 / 13. NUMBER OF PAGES: 105 / 104 P.
14. MONITORING AGENCY NAME & ADDRESS *(if different from Controlling Office)*	15. SECURITY CLASS. *(of this report)*: UNCLASSIFIED / 15a. DECLASSIFICATION/DOWNGRADING SCHEDULE

16. DISTRIBUTION STATEMENT *(of this Report)*

Approved for public release; distribution unlimited.

17. DISTRIBUTION STATEMENT *(of the abstract entered in Block 20, if different from Report)*

18. SUPPLEMENTARY NOTES

19. KEY WORDS *(Continue on reverse side if necessary and identify by block number)*

Aerodynamics	Gas Dynamics
Numerical Analysis	Applied Mathematics
Reentry Aerodynamics	MacCormack's Method

20. ABSTRACT *(Continue on reverse side if necessary and identify by block number)*

Solutions were obtained for hypersonic flow over sharp cones at high angle of attack by numerically integrating through use of MacCormack's method the Navier-Stokes equations subject to a conical symmetry assumption. The boundary conditions for the integration were chosen to match the experimental conditions of Tracy (M = 7.95), Stetson (M = 14.2), and McElderry (M = 6.05). A technique (normal stress damping) was developed to provide damping of the numerical oscillations occurring at shock discontinuities during the integration.

DD FORM 1 JAN 73 1473 EDITION OF 1 NOV 65 IS OBSOLETE

UNCLASSIFIED

SECURITY CLASSIFICATION OF THIS PAGE *(When Data Entered)*

012070

The general features which appeared in experiment were shown to appear in the results of the integration, including the proper behavior, in laminar flow, of the viscous layer and the vertical singularity. The results agreed quite well with the experimental data of Tracy and agreed less with the experimental data of Stetson. A thinner calculated lee side viscous layer for Stetson's case was attributed to failure of the present technique to model non-conical nose effects. A solution obtained just upstream of boundary layer transition at the experimental conditions of McElderry agreed with experiment when conically projected into the turbulent regime. The adequacy of the conical symmetry assumption is therefore indicated for the turbulent regime on conical bodies.

FOREWORD

The author would like to acknowledge the guidance of Dr. W. L. Hankey and Dr. M. E. Franke throughout the course of this research. The research was performed at the Theoretical Aerodynamics Research Laboratory, Aerospace Research Laboratories and at the Aerodynamics and Airframe Branch, Air Force Flight Dynamics Laboratory. This report was prepared under Task 2307/04 entitled Aeromechanics Basic Research.

The material reported herein is based on the author's dissertation submitted in partial fulfillment of the requirements for the Doctor of Philosophy degree at the Air Force Institute of Technology, Wright-Patterson AFB, Ohio.

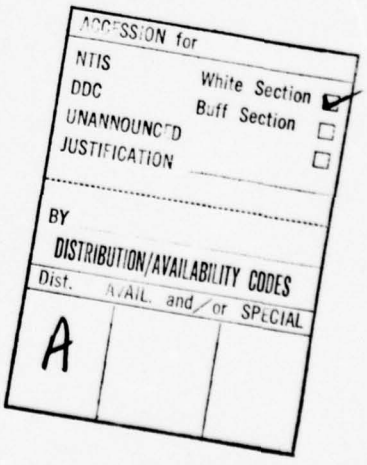


TABLE OF CONTENTS

SECTION		PAGE
I	INTRODUCTION	1
II	BACKGROUND	3
III	APPROACH	6
	1. Description of Conical Flow	6
	2. The Fluid Flow Equations	8
	3. The Numerical Integration Scheme	13
	4. The Solution Procedure	17
IV	NUMERICAL RESULTS	23
	1. Tracy's Data	23
	2. Stetson's Data	29
	3. McElderry's Data	31
V	CONCLUSIONS	37
VI	RECOMMENDATIONS	40
REFERENCES		41
APPENDIX A.	BOUNDARY CONDITIONS	79
APPENDIX B.	NORMAL STRESS DAMPING	83
APPENDIX C.	STABILITY CRITERIA	87

PRECEDING PAGE BLANK-NOT FILMED

LIST OF ILLUSTRATIONS

FIGURE		PAGE
1	Cross Section of Supersonic Inviscid Flow About Cone at $\alpha = 0°$	44
2	Coordinate System and Computational Mesh Shown in Relation to Cone	45
3	Cutaway Drawing Showing Typical Particle Paths for Supersonic Inviscid Flow About Cone at High α	46
4	Approximate Cross-Flow Streamline Pattern for Cone at High α	47
5	Physical Implications of Conical Symmetry Assumption Illustrating Relationship of Viscous Layer Edge and Spherical Radius	48
6	Comparison of Calculated Cone Surface Pressure with that Obtained from Hypersonic Weak Interaction Theory	49
7	Comparison of Calculated and Experimental Surface Pressure at Tracy's Conditions, $\alpha = 8°$	50
8	Comparison of Calculated and Experimental Surface Pressure at Tracy's Conditions, $\alpha = 12°$	51
9	Comparison of Calculated and Experimental Surface Pressure at Tracy's Conditions, $\alpha = 20°$	52
10	Comparison of Calculated and Experimental Surface Pressure at Tracy's Conditions, $\alpha = 24°$	53
11	Comparison of Circumferential Pitot Pressure Surveys at Constant Height Above the Cone Surface at Tracy's Conditions, $\alpha = 12°$	54
12	Comparison of Circumferential Pitot Pressure Surveys at Constant Height Above the Cone Surface at Tracy's Conditions, $\alpha = 20°$	55
13	Comparison of Circumferential Pitot Pressure Surveys at Constant Height Above the Cone Surface at Tracy's Conditions, $\alpha = 24°$	56
14	Comparison of Pitot Pressure Survey Along Lee Centerline ($\phi = 180°$) at Tracy's Conditions, $\alpha = 24°$	57
15	Calculated Static Pressure Along θ at 60° Circumferential Intervals at Tracy's Conditions, $\alpha = 12°$	58

LIST OF ILLUSTRATIONS (CONT'D)

FIGURE		PAGE
16	Cross-Flow Velocity Vectors Plotted as Seen on Spherical Surface at Tracy's Conditions, α = 12°	59
17	Cross-Flow Velocity Vectors Plotted as Seen on Spherical Surface at Tracy's Conditions, α = 20°	60
18	Cross-Flow Velocity Vectors Plotted as Seen on Spherical Surface at Tracy's Conditions, α = 24°	61
19	Comparison of Calculated and Experimental Flow Field Features at Tracy's Conditions, α = 12°	62
20	Comparison of Calculated and Experimental Flow Field Features at Tracy's Conditions, α = 24° (Legend Given in Figure 19)	63
21	Comparison of Calculated and Experimental Surface Pressure at Stetson's Conditions	64
22	Comparison of Pitot Pressure Survey at Constant ϕ at Stetson's Conditions, ϕ = 180°	65
23	Comparison of Pitot Pressure Survey at Constant ϕ at Stetson's Conditions, ϕ = 160°	66
24	Comparison of Pitot Pressure Survey at Constant ϕ at Stetson's Conditions, ϕ = 140°	67
25	Experimentally Determined Shock Position Showing Effective Nose Blunting at Stetson's Conditions (Taken from Reference 22)	68
26	Cross-Flow Velocity Vectors Plotted as Seen on Spherical Surface at Stetson's Conditions	69
27	Conical Comparison of Calculated ($Re_x = 1.5 \times 10^6$) and Experimental ($Re_x = 15.0 \times 10^6$) Surface Pressure at McElderry's Conditions	70
28	Conical Comparison of Calculated ($Re_x = 1.5 \times 10^6$) and Experimental ($Re_x = 15.0 \times 10^6$) Pitot Pressure Survey at Constant ϕ at McElderry's Conditions, ϕ = 180°	71
29	Conical Comparison of Calculated ($Re_x = 1.5 \times 10^6$) and Experimental ($Re_x = 15.0 \times 10^6$) Pitot Pressure Survey at Constant ϕ at McElderry's Conditions, ϕ = 160°	72

LIST OF ILLUSTRATIONS (CONCLUDED)

FIGURE		PAGE
30	Conical Comparison of Calculated ($Re_x = 1.5 \times 10^6$) and Experimental ($Re_x = 15.0 \times 10^6$) Pitot Pressure Survey at Constant ϕ at McElderry's Conditions, $\phi = 140°$	73
31	Calculated Mach Number Distributions at Constant ϕ at McElderry's Conditions	74
32	Cross-Flow Velocity Vectors Plotted as Seen on Spherical Surface at McElderry's Conditions	75
33	Comparison of Experimental Laminar and Turbulent Viscous Layer Features (Taken from Reference 33)	76
34	Demonstration of the Effect of Normal Stress Damping on Calculated Static Pressure Along θ, $\alpha = 0°$	77

SYMBOLS

c = Local speed of sound

C_v = Specific heat at constant volume

C_p = Specific heat at constant pressure

$\vec{D}$ = Time vector in governing equations

e = Total internal energy $(C_v T + V^2/2)$

$\vec{E}$ = Vector in governing equations (r coordinate)

$\vec{F}$ = Vector in governing equations (θ coordinate)

$\vec{G}$ = Vector in governing equations (ϕ coordinate)

$\vec{H}$ = Vector in governing equations (constant terms)

$\vec{J}$ = Vector resulting from application of conical symmetry assumption

K = Thermal conductivity

k = $(\gamma - 1)/2\gamma$

L = Cone length

m = Courant number

P = Pressure in damping scaling equations

p = Pressure

$\dot{q}$ = Heat transfer rate

Re = Reynolds number $(V_{max}\rho_{t_\infty} r)/\mu$

R_g = Gas constant

r = Radial coordinate

T = Temperature

t = Time

U = Velocity in linear wave equation

$\tilde{U}$ = Predicted velocity

u = Velocity in r direction

SYMBOLS (CONT'D)

V = Total velocity $(u^2 + v^2 + w^2)^{1/2}$

V_{max} = Maximum adiabatic velocity $(2\gamma/(\gamma-1)R_g T_{t\infty})^{1/2}$

v = Velocity in θ direction

w = Velocity in ϕ direction

x = Distance along cone surface, measured from vertex

y = Distance above cone surface

GREEK SYMBOL

α = Angle of attack

β = Damping multiplier

γ = Ratio of specific heats (C_p/C_v)

δ = Boundary layer thickness

θ = Coordinate, conical angle

λ = Second coefficient of viscosity $(-2/3\ \mu)$

λ_{Re} = $-\frac{2}{3_{Re}}$

μ = Absolute viscosity

ν = Maximum eigenvalue of coefficient matrix

ρ = Density

σ = Normal stress

τ = Shear stress

ϕ = Coordinate, circumferential angle

$\overline{\chi}$ = Hypersonic similarity parameter $(M_\infty^3/(Re_x)^{1/2})$

ψ_A = Flow streamline

ψ_B = Flow streamline

SYMBOLS (CONCLUDED)

SUBSCRIPTS

c	=	Cone
i	=	Time step number
j,k	=	Mesh point location
n	=	Normal direction
η	=	Mesh point location
p	=	Pitot quantity
s	=	Surface quantity
t	=	Total quantity
w	=	Wall value
x	=	Local quantity based on distance from cone vertex
∞	=	Free stream quantity
1,2,3	=	Pertaining to r, θ, ϕ, direction

SUMMARY

Solutions were obtained for hypersonic flow over sharp cones at high angle of attack which include the viscous effects present in experiment. These solutions were obtained by integrating the Navier-Stokes equations subject to a conical symmetry assumption. The integration technique used was MacCormack's method with boundary conditions chosen to match available experiments. The experimental conditions were: (1) Those of Tracy for a 10° half angle cone at angles of attack of 0°, 8°, 12°, 20°, and 24° in M = 7.95 flow at Re = 4.2×10^5. (2) Those of Stetson for a 5.6° half angle cone at 10° angle of attack in M = 14.2 flow at Re = 7.9×10^5. (3) Those of McElderry for a 6° half angle cone at 12° angle of attack in M = 6.05 flow at Re = 1.5×10^6. A physically based technique (normal stress damping) was demonstrated for controlling starting transients and for reducing or eliminating numerical oscillations occurring at shock discontinuities during the integration.

The general features which appeared in experiment were shown to appear in the results of the integration, including the proper behavior, in laminar flow, of the viscous layer and the vortical singularity. The results agreed quite well with the experimental data of Tracy (hypersonic similarity parameter $\overline{\chi} \simeq 1$) except for a discrepancy in pitot pressure in the viscous layer evident in a small region near the leeward centerline of the cone. The agreement with the experimental data ($\overline{\chi} \simeq 3$) of Stetson was less adequate. Surface pressure agreement in this instance was quite reasonable. However, a somewhat thin lee side viscous layer resulted in a calculated bow shock wave position 27% closer to the cone surface at the lee centerline. It was concluded that the lee side viscous layer discrepancies at both experimental conditions were primarily due to lack of any mechanism in the present technique to model the non-conical flow near the nose of the cone. A solution obtained just upstream of the beginning of boundary layer transition at the experimental conditions of McElderry agreed well with experiment when conically projected far into the turbulent regine. The adequacy of the conical symmetry assumption is therefore indicated for the turbulent regime on conical bodies.

In summary, the results show good agreement with experiment for values of the hypersonic similarity parameter ($\overline{\chi} \leq 1.0$) and less adequate agreement at higher $\overline{\chi}$. Angle of attack limitations encountered in previous inviscid cone flow calculations were not encountered in the present study.

SECTION I

INTRODUCTION

Supersonic flow about cones has been a subject of interest to aerodynamicists for many years. Cones comprised one of the earliest attempts to streamline such items as fuel tanks, weaponry, and fuselages, with locally conical nose shapes still in use on today's modern high-speed aircraft. The missile era has also seen the use of cones as a primary or partial shape for reentry vehicles in current ICBMs. This study is directed toward the latter application and is in response to the need for more accurate aerodynamic prediction techniques in this area.

The two primary elements which dictate the need for increased prediction accuracy are the current high cost of wind tunnel testing and the difficulty of simulating the reentry vehicle flight regime. The advent of the high-speed, large-capacity computer in recent years has opened up a means to reduce cost both through reducing unit computational cost and through reducing the amount of experimental verification required during the systems acquisition process. The remaining task is the research necessary to develop the required numerical techniques and the verification of these techniques through comparison of numerical results with those obtained experimentally.

Particular solutions to the complete governing equations of fluid flow are available for very few sets of boundary and initial conditions. It has therefore been necessary in nearly all cases to reduce the complexity and scope of the equations through neglect of the viscous effects and/or by reduction of the number of dimensions to be considered in the problem. Prior to 1973, most attempts to solve the flow about conical bodies used inviscid forms of the governing equations. The two primary difficulties that have been encountered with these solutions are the failure of the inviscid equations to model properly the lee side flow in which viscous effects predominate and the occurrence of numerical instabilities which are encountered at high angle of attack.

If the goal of reducing the amount of experimental verification is to be attained, then improved numerical techniques must be developed to overcome these difficulties. The present study will present and compare with experiment a technique which resolved both of these difficulties.

This report contains first a brief description of the developments in the solution of flow over conical bodies. The solution approach used in the present study is then presented in four parts. First, a discussion of the general features of conical flows is given with particular emphasis on the circular sharp cone at angle of attack. The governing equations are then presented and changes due to the conical symmetry assumption are discussed. The application of MacCormack's numerical integration scheme to the equations is given in the third part. Part four describes the details of the finite difference mesh and the manner in which the integration was accomplished. The results of the numerical integration are then compared with experiment for selected conditions for which previously published experimental data were available. Conclusions drawn from these comparisons are presented to complete the study.

SECTION II

BACKGROUND

The history of the solution of supersonic cone flows has been greatly affected by and dependent on the development of high-speed digital computers. It is generally agreed that the Navier-Stokes equations in their complete form provide sufficient knowledge of the physics of the flow for nonreacting gases. However, the scope and complexity of these partial differential equations required great simplification of the set in order to obtain solutions prior to the development of the digital computer. These simplifications led to poor agreement of the solution with experiment except for restricted conditions. Although the restrictions have been considerably relaxed in more recent studies, a full three-dimensional solution of the complete governing equations is still not practical for general configurations. This section will provide a brief description of the more important supersonic cone flow solutions published prior to the present study.

The history of solution techniques for supersonic cone flow began in 1933 with the publication by Taylor and Maccoll (Reference 1) of an ordinary differential equation solution for axisymmetric inviscid flow about a sharp cone. The next significant event occurred in 1947 with publication of tabulated Taylor-Maccoll solutions by Kopal and Associates (Reference 2). These tabulations were extended to include angle of attack in References 3 and 4. Ferri (Reference 5) obtained first-order solutions for cones at small angle of attack in which he noted the properties of the vortical layer about the cone and showed the existence of a vortical singularity in the lee side flow. With this publication by Ferri, all important features (except for the lee side imbedded shock waves) of the inviscid conical flow fields were known and defined. Since Ferri's solution was demonstrated only for $\alpha/\theta_c \leq 1.6$, it remained then to increase the angle of attack for which a solution could be obtained and to account for imbedded shock waves and viscous effects present in experiment.

Improvement of the digital computer in the middle 1960's allowed the solution of the nonlinear Euler equations in more complete form. Babenko, et al. (Reference 6) obtained smooth-body solutions for the inviscid Euler equations in supersonic flow without further simplification. This work is an early example of the use of finite difference techniques to integrate the three-dimensional flow equations in their nonlinear form. Another example of this approach is the work of Bohachevsky and Rubin (Reference 7).

The finite difference scheme used in the present work can be traced back to that of Lax and Wendroff (Reference 8). This second-order scheme, when applied to the flow equations case in conservation law form allows shock discontinuities to form without special provisions during the integration process. MacCormack's (Reference 9) variant of the Lax-Wendroff scheme as applied by Kutler (Reference 10) extended the angle of attack range for which inviscid sharp cone flows could be obtained. Further applications (References 11-13) of this technique to inviscid flows were made by Kutler, et al. to allow for real gas effects, varying geometries, and passing through shock fronts. However, the inaccuracies due to neglect of viscous effects were not effectively dealt with until the work of Lin and Rubin (References 14,15) and Lubard and Helliwell (Reference 16). Lin and Rubin solved a boundary layer equation set modified to account for centrifugal force and cross flow diffusion in the weak interaction region and a parabolic set in the hypersonic tip region to obtain solutions including viscous effects up to twice the cone half angle. However, the former approach requires input of surface pressure from experiment or other source. Lubard and Helliwell utilized an implicit finite difference technique similar to that of Lin and Rubin to solve the flow equations subject to a parabolic assumption for the streamwise shear stress terms. This space marching technique required an accurate initial surface for the integration to proceed. The lack of such a surface required that the integration be started at zero angle of attack and that the angle of attack be gradually increased until the desired value is reached. The solution must then be carried far enough downstream for relaxation of the effects of this procedure to occur. The comparison with experiment for this technique at a given physical point on the cone surface is therefore uncertain.

As noted in this brief survey, solutions of viscous flow over cones have only recently been attempted (1973). The present study seeks to illustrate a technique which includes viscous effects in cone flow calculations and removes limitations present in the inviscid calculations. The details of this technique are given in the following section.

SECTION III

APPROACH

This section presents the details of the solution approach used in the present study. A brief description of the general features of conical flow is presented in part one. This is followed by a discussion in part two of the governing equations of fluid flow and the changes in these equations which result from the conical symmetry assumption. Part three describes the application of MacCormack's numerical integration scheme to the equation set obtained in part two. Part four then gives the details of the solution procedure.

1. DESCRIPTION OF CONICAL FLOW

As noted in the introduction to the present study, supersonic flow about conical bodies has been of considerable interest to aerodynamicists. Supersonic inviscid conical flows appear at first inspection to be fully three-dimensional. However, they are in reality only two-dimensional with no gradients in any quantity occurring along the third dimension. A more detailed description of these flows is presented here to promote understanding of their unique properties.

Truly conical supersonic flows are steady state solutions to the Euler equations (Navier-Stokes equations with viscous terms neglected) for a particular set of boundary conditions. These conditions are a uniform supersonic outer flow and a body generated by rays passing through a common vertex. To ensure that the flow is completely conical, the additional condition of a bow shock wave attached to the vertex of the body must be imposed. Examples of bodies which generate these flows are: (1) circular cones, (2) elliptical cones, (3) delta wings, (4) delta wing/conical body combinations, and (5) axial corners. Many variations/combinations of these bodies are possible which produce conical flows. Also, conical bodies which appear as nose shapes in more general configurations will produce locally conical flows. The characteristics of these flows are examined below.

The dominant feature of conical flow is that all fluid quantities are constant along rays passing through the vertex of the conical body. By noting that these rays are equivalent to the spherical radius r with origin at the cone vertex, conical flow can be mathematically described by stating that derivatives of all fluid quantities with respect to r are identically zero. The physical implications of this statement are illustrated in Figure 1. This figure shows a plane cut of an axisymmetric supersonic cone flow. A conical flow exists when the flow quantities at point A (along streamline ψ_A) are identical to those at point B (along streamline Ψ_B). The flow at both point A and point B can be completely described in terms of the single angle θ for this two-dimensional cut. What is apparently a two-dimensional flow is then in reality only one-dimensional (sometimes referred to as 1-1/2 dimensional, since two velocity components are still present).

Although somewhat more difficult to visualize, conical bodies at angle of attack in supersonic flow also produce conical flow fields. By analogy with the above discussion, these flows can also be described completely in terms of the independent variable θ and a circumferential angle ϕ (these angles are illustrated in Figure 2). All natural features of the flow; such as imbedded shocks, bow shocks, slip lines, etc.; form surfaces composed of rays passing through the conical vertex. An example sketch of this flow is shown in Figure 3. The streamlines shown in Figure 3 show the manner in which the flow crosses the bow shock, expands around the body, and then is turned back along the cone by the imbedded shock. It is instructive to view flow features on a spherical surface through the field.

Figure 4 illustrates the approximate cross flow streamline pattern on the spherical surface and shows relative location of the shock waves. The point at which the cross flow streamlines converge is the vortical singularity first noted by Ferri (Reference 5). The streamlines all have different values of entropy which implies that density and entropy are discontinuous at the singularity with pressure being continuous.

This singularity rests on the cone surface (in fact, Melnik (Reference 17) has shown the possibility of two singularities on the surface) at low angles of attack and lifts off as angle of attack increases.

In summary, conical flows can be completely described in a spherical coordinate system by only two independent coordinates (θ, ϕ). All natural features of the flow are also conical surfaces. These facts tend to render a very complex flow more amenable to solution by presently available techniques.

2. THE FLUID FLOW EQUATIONS

In this section, the basic equations of fluid flow are presented in complete form and the conical symmetry assumption is applied. The resulting equations allow integration to take place on a single spherical surface. The non-dimensionalization of the equations and the physical meaning of the assumptions are discussed.

The Navier-Stokes equations which describe flow of a perfect gas, can be written in conservation law form (Reference 18) for a spherical coordinate system as follows:

$$\frac{\partial \vec{D}}{\partial t} + \frac{\partial \vec{E}}{\partial r} + \frac{\partial \vec{F}}{\partial \theta} + \frac{\partial \vec{G}}{\partial \phi} + \vec{H} = 0 \qquad (1)$$

where

$$\vec{D} = r^2 \sin\theta \begin{bmatrix} \rho \\ \rho u \\ \rho v \\ \rho w \\ \rho e \end{bmatrix}$$

$$\vec{E} = r^2 \sin\theta \begin{bmatrix} \rho u \\ \rho u^2 - \sigma_{11} \\ \rho uv - \tau_{12} \\ \rho uw - \tau_{13} \\ \rho ue + \dot{q}_r - u\sigma_{11} - v\tau_{12} - w\tau_{13} \end{bmatrix}$$

$$\vec{F} = r \sin\theta \begin{bmatrix} \rho v \\ \rho uv - \tau_{21} \\ \rho v^2 - \sigma_{22} \\ \rho wv - \tau_{23} \\ \rho ve + \dot{q}_\theta - u\tau_{21} - v\sigma_{22} - w\tau_{23} \end{bmatrix}$$

$$\vec{G} = r \begin{bmatrix} \rho w \\ \rho uw - \tau_{31} \\ \rho vw - \tau_{32} \\ \rho w^2 - \sigma_{33} \\ \rho we - \dot{q}_\phi - u\tau_{31} - v\tau_{32} - w\sigma_{33} \end{bmatrix}$$

$$\vec{H} = r \sin\theta \begin{bmatrix} 0 \\ -(\rho v^2 - \sigma_{22}) - (\rho w^2 - \sigma_{33}) \\ -\cot\theta\ (\rho w^2 - \sigma_{33}) + (\rho uv - \tau_{12}) \\ \cot\theta\ (\rho vw - \tau_{23}) + (\rho uw - \tau_{13}) \\ 0 \end{bmatrix}$$

The stress tensor terms τ_{ij} and σ_{ii} will be defined in detail later.

Solution of the equation set in the form shown above would require very large amounts of machine time even for simple aerodynamic configurations. This has led researchers in the past to simplify the equation set through neglect of the stress terms (inviscid flow) and/or by

reducing the number of dimensions to be considered in the problem. One class of flows which has been extensively examined, (References 10,19,20) through neglect of the viscous terms, is that of inviscid conical flow.

A conical flow, as noted in the previous section, can be described as an inviscid steady flow in which all flow quantities are constant along rays passing through the vertex of the conical body. If a body fixed spherical coordinate system (Figure 2) centered at the vertex of the conical body is used to describe the flow, then all spherical surfaces must have the same vector and scalar values of the flow quantities for a given (θ, ϕ) point on each surface. Therefore, all derivatives of flow quantities with respect to the spherical radius (r) of these spherical surfaces from the origin must be zero. This has the effect of reducing the number of independent variables in the problem by one.

Examination of experimental studies of supersonic flow over conical bodies (References 21-23) reveals that these flows exhibit approximate conical behavior downstream from the nose region even though relatively large viscous regions exist. Cross (Reference 21) determined that the viscous layer growth on the lee side of a delta wing in supersonic flow was essentially conical. The oil flow separation traces for sharp cones in the experimental study of Stetson (Reference 22) are approximately straight (but the conical vertex of these traces is displaced downstream by nose effects). Therefore, in concert with an idea first broached by Anderson (Reference 24) for axial corner flow, the conically symmetric flow approximation ($\frac{\partial}{\partial r} \equiv 0$) is applied to all terms in Equation 1.

The resulting equation set is:

$$\frac{\partial \vec{D}}{\partial t} + \frac{\partial \vec{F}}{\partial \theta} + \frac{\partial \vec{G}}{\partial \phi} + \vec{H}' = 0 \qquad (2)$$

where:

(a) $\vec{D}$, $\vec{F}$, and $\vec{G}$ are unchanged except in the definition of the stress terms.

$$(b)\ \frac{\partial}{\partial r}\left[\frac{\vec{E}}{r^2\sin\theta}\right] = \frac{1}{r}\begin{bmatrix} 0 \\ \sigma_{11} \\ \tau_{21} \\ \tau_{31} \\ u\sigma_{11} + v\tau_{12} + w\tau_{13} \end{bmatrix} = \vec{J}$$

$$(c)\ \vec{H}' = \vec{H} + \frac{2\vec{E}}{r} + \vec{J}\, r^2\sin\theta$$

$$\text{or}\quad \vec{H}' = r\sin\theta \begin{bmatrix} 2\rho u \\ -(\rho v^2-\sigma_{22}) - (\rho w^2-\sigma_{33}) + 2\rho u^2-\sigma_{11} \\ -\cot\theta\,(\rho w^2-\sigma_{33}) + 3\rho uv - 2\tau_{12} \\ \cot\theta\,(\rho vw-\tau_{23}) + 3\rho uw - 2\tau_{13} \\ 2\rho ue - u\sigma_{11} - v\tau_{12} - w\tau_{13} \end{bmatrix}$$

These equations are non-dimensionalized as follows, with dimensional quantities denoted by primes:

$$u = \frac{u'}{V_{max}} \qquad v = \frac{v'}{V_{max}} \qquad w = \frac{w'}{V_{max}}$$

$$p = \frac{p'}{p_{t_\infty}} \qquad \rho = \frac{\rho'}{\rho_{t_\infty}} \qquad t = \frac{t'}{r/V_{max}} \qquad T = \frac{T'}{T_{t_\infty}}$$

$$e = \frac{e'}{V_{max}^2} \qquad Re = \frac{V_{max}\,\rho_{t_\infty} r}{\mu}$$

$$V_{max} = \left[\frac{2\gamma}{\gamma-1}\, R_g T'_{t_\infty}\right]^{1/2} \qquad k = \frac{\gamma-1}{2\gamma} \qquad (3)$$

Equation 3 indicates a notational change from this point onward. Hereafter, units will be specified where dimensional quantities are used. The quantities used for non-dimensionalization are due to

Kutler (Reference 10). It is significant that when time is non-dimensionalized by the parameter r/V_{max}, the r dependence in Equation 2 is contained in the Reynolds number. The net effect is that the calculation is carried out at a single (θ, ϕ) spherical surface with the distance of this surface from the cone apex determined by the Reynolds number. Therefore, all spherical radius scaling is now contained in the Reynolds number alone.

The non-dimensional stress terms for this equation set are defined as follows:

$$\tau_{12} = \tau_{21} = \frac{1}{Re} \left(\frac{\partial u}{\partial \theta} - v\right)$$

$$\tau_{13} = \tau_{31} = \frac{1}{Re \sin\theta} \left(\frac{\partial u}{\partial \phi} - w \sin\theta\right)$$

$$\tau_{23} = \tau_{32} = \frac{1}{Re \sin\theta} \left[\frac{\partial}{\partial \theta} (w \sin\theta) - 2 w \cos\theta + \frac{\partial v}{\partial \phi}\right]$$

$$\sigma_n = \lambda_{Re} \left[2 u \sin\theta + \frac{\partial}{\partial \theta} (v \sin\theta) + \frac{\partial w}{\partial \phi}\right]$$

$$\lambda_{Re} = -\frac{2}{3Re}$$

$$\sigma_{11} = -kp + \frac{\sigma_n}{\sin\theta}$$

$$\sigma_{22} = -kp + \frac{2}{Re} \left(\frac{\partial v}{\partial \theta} + u\right) + \frac{\sigma_n}{\sin\theta}$$

$$\sigma_{33} = -kp + \frac{2}{Re \sin\theta} \left(\frac{\partial w}{\partial \phi} + u \sin + v \cos\theta\right) + \frac{\sigma_n}{\sin\theta} \qquad (4)$$

The heat transfer terms are defined as follows:

$$\dot{q}_\theta = -\frac{1}{2RePr} \frac{\partial T}{\partial \theta} \quad , \quad \dot{q}_\phi = -\frac{1}{2RePr} \frac{\partial T}{\partial \phi} \qquad (5)$$

where $Pr = \frac{\mu C_p}{K}$

At this point, it is prudent to examine further the physical implications of the approximations applied to the above equation set. It should first be noted that the only approximations now inherent to the equations are that a perfect gas is required and that conically

symmetric flow is assumed at all points in the field. Figure 5 depicts a cross section through an axisymmetric cone flow with a somewhat exaggerated boundary layer thickness shown by the dashed line. The thesis is that at a given calculation surface, the viscous layer thickness will be properly scaled by the Reynolds number based on the spherical radius to that surface. The only error then would be in the local gradients of the flow quantities and would be of the order of the angle between the spherical radius and the edge of the boundary layer at the calculation surface. The same statement could be made concerning a calculation at any point along the cone downstream from the non-conical nose region. Therefore, since the growth of the viscous layer thickness will not in general be linear, the assumption in reality only implies locally conical flow.

In order to test the above hypothesis, calculations were carried out using the above equation set and the method set forth in the following sections applied to axisymmetric cone flow. The cone surface pressure resulting from these calculations is shown in Figure 6 and compared with hypersonic weak interaction theory for axisymmetric cone flow (Reference 29). The agreement shown in Figure 6 between the calculations and the weak interaction theory is quite good with divergence noted (as expected) toward the nose of the cone. In order to fully verify the hypothesis, two-dimensional calculations compared with appropriate experimental data are required. The remainder of this report will present the results of calculations carried out at selected conditions for which experimental data are available. Comparisons are made and conclusions are drawn concerning the adequacy of the hypothesis.

3. THE NUMERICAL INTEGRATION SCHEME

This section discusses the choice of MacCormack's finite difference scheme as the integration method for this problem. The scheme is illustratively applied to the one-dimensional wave equation as an example. The equations to be integrated are cast in MacCormack's predictor-corrector form, and the finite difference representation of the derivatives is shown.

The utility of MacCormack's (Reference 9) finite difference scheme for the solution of inviscid supersonic flows has been demonstrated in numerous studies (References 10-13). More recent studies have also shown it to give excellent results for two-dimensional viscous flows with separation (References 25-27). The scheme can be described as a second-order accurate predictor-corrector sequence for the integration of partial differential equations. MacCormack's scheme is a variant of the Lax-Wendroff scheme (Reference 10) and can be shown (as applied to the linear wave equation) to reduce to Lax-Wendroff form when the predictor is substituted into the corrector. Since second-order difference schemes generally give better results with fewer mesh points than first-order schemes, MacCormack's proven differencing scheme is chosen for the present study.

If an Euler predictor followed by a modified Euler corrector is applied to the 1-D wave equation $\frac{\partial U}{\partial t} + c\frac{\partial U}{\partial x} = 0$;

$$\text{Predictor:} \qquad \tilde{U}_{i+1} = U_i - c\Delta t\,(U_x)_i \tag{6}$$

$$\text{Corrector:} \qquad U_{i+1} = \frac{1}{2}\left[U_i + \tilde{U}_{i+1} - c\Delta t\,(\tilde{U}_x)_{i+1}\right] \tag{7}$$

MacCormack's scheme results when forward first spatial differences are used in the predictor and backward first differences in the corrector. The predictor corrector sequence is then (with i representing time location and j spatial location):

$$\text{Predictor:} \qquad \tilde{U}_j^{i+1} = U_j^i - \frac{c\Delta t}{\Delta x}\,(U_{j+1}^i - U_j^i) \tag{8}$$

$$\text{Corrector:} \qquad U_j^{i+1} = \frac{1}{2}\left[U_j^i + \tilde{U}_j^{i+1} - \frac{c\Delta t}{\Delta x}\,(\tilde{U}_j^{i+1} - \tilde{U}_{j-1}^{i+1})\right] \tag{9}$$

The two equations collapse, when the appropriate substitutions are made, to the following Lax-Wendroff form:

$$U_j^{i+1} = U_j^i - \frac{c\Delta t}{2\Delta x}\,(U_{j+1}^i - U_{j-1}^i) + \frac{c^2\Delta t^2}{\Delta x^2}\,(U_{j+1}^i - 2U_j^i + U_{j-1}^i) \tag{10}$$

The leading error terms which are truncated through use of this finite difference equation representation are of the form (with the derivatives evaluated at an undetermined point within the range of interest)

$$+ \frac{c\Delta t\Delta x^2}{6} U_{x^3} - \frac{c\Delta t^2\Delta x^2}{24} U_{x^4} + \frac{\Delta t^3}{6} U_{t^3}$$

which illustrates that when Δt and Δx are of the same order, the estimated truncation error must be of $O(\Delta t^3)$ and the method can be said to be second-order accurate. The stability of MacCormack's scheme is examined in Appendix C.

When the scheme is applied to Equation 2, the resulting MacCormack's predictor-corrector steps are as follows (the $\rightarrow$ used previously to indicate vector quantities is omitted here for clarity):

Predictor:
$$\tilde{D}^{i+1}_{j,k} = D^{i}_{j,k} - \frac{\Delta t}{\Delta\theta}\left(F^{i}_{j+1,k} - F^{i}_{j,k}\right) - \frac{\Delta t}{\Delta\phi}\left(G^{i}_{j,k+1} - G^{i}_{j,k}\right) - \Delta t\, H'^{i}_{j,k} \qquad (11)$$

Corrector:
$$D^{i+1}_{j,k} = \frac{1}{2}\left[D^{i}_{j,k} + \tilde{D}^{i+1}_{j,k} - \frac{\Delta t}{\Delta\theta}\left(\tilde{F}^{i+1}_{j,k} - \tilde{F}^{i+1}_{j-1,k}\right) - \frac{\Delta t}{\Delta\phi}\left(\tilde{G}^{i+1}_{j,k} - \tilde{G}^{i+1}_{j,k-1}\right) - \Delta t\, \tilde{H}'^{i+1}_{j,k}\right] \qquad (12)$$

where $\sim$ indicates that the flow quantities are evaluated at the predictor level and $D^{i}_{j,k}$ implies $D(i\Delta t, j\Delta\theta, k\Delta\phi)$. The presence of the $\vec{H}'$ matrix in these equations indicates that they are in so called "weak" conservation form (Reference 28). Numerical results in the present study reveal that no significant error in total temperature occurs across shock transitions through use of this form of the equations (implying that energy must have been properly conserved).

Since Equation 2 contains derivatives in the stress terms which remain as an integral part of the matrix terms, a value of the derivatives must be obtained at each of the mesh points used in the primary differencing.

These values must be obtained in a manner which will maintain both consistency and accuracy of the differencing equation. This was done in the present study by evaluating the interior derivative terms with respect to the same independent variable using first-order difference approximations of opposite sense to the exterior differences. An illustration follows for the predictor.

Consider the vector $\vec{F}$ which consists of functions of the flow quantities and their derivatives. The finite difference representation of $\frac{\partial \vec{F}}{\partial \theta}$ is

$$\frac{\partial \vec{F}}{\partial \theta} \simeq \frac{1}{\Delta\theta} \left(\vec{F}_{j+1,k} - \vec{F}_{j,k}\right) \tag{13}$$

Assume that the vector $\vec{F}$ contains the derivative $\frac{\partial u}{\partial \theta}$, values of which are therefore required at mesh points j,k and j+1,k in the difference representation. These values are obtained by $\frac{\partial u}{\partial \theta} \simeq \frac{1}{\Delta\theta} \left(u_{j+1,k} - u_{j,k}\right)$ at j+1,k and $\frac{\partial u}{\partial \theta} \simeq \frac{1}{\Delta\theta} \left(u_{j,k} - u_{j-1,k}\right)$ at j,k. The resulting finite difference representation for $\frac{\partial^2 u}{\partial \theta^2}$ is the standard second-order accurate difference centered at j.

When a cross derivative term is involved (say a $\frac{\partial u}{\partial \phi}$ term contained in $\frac{\partial \vec{F}}{\partial \theta}$), second order centered first differences are used. With $\frac{\partial \vec{F}}{\partial \theta}$ represented as above, $\frac{\partial u}{\partial \phi} \simeq \frac{1}{\Delta\phi} \left(u_{j+1,k+1} - u_{j+1,k-1}\right)$ at j+1,k and $\frac{\partial u}{\partial \phi} \simeq \frac{1}{\Delta\phi} \left(u_{j,k+1} - u_{j,k-1}\right)$ at j,k. This results in the standard second-order accurate second difference for the $\frac{\partial^2 u}{\partial \phi \partial \theta}$ difference centered at j+1/2.

This procedure is also used in the corrector step with all differencing reversed in the θ direction. The resulting differences, when combined with the predictor into the Lax-Wendroff form, are correct and centered at j.

This essentially completes the application of MacCormack's scheme to Equation 2. It should be apparent that throughout the analysis of

MacCormack's scheme, careful prescription of the first-order differences in the individual predictor and corrector results in a second-order accurate scheme for the entire cycle. The details of the integration procedure are described in the following section.

4. THE SOLUTION PROCEDURE

In this section, the details of the integration procedure are discussed. The finite difference mesh is first described, followed by the initialization used for the initial value problem and a brief description and discussion of the physical boundary conditions. Finally, the convergence criteria for determining when the sought-for steady state solution has been reached is described.

As stated earlier in this section the calculation takes place on a spherical surface located at a distance r from the vertex of the cone. The distance r is determined by the distance along the cone at which correlation with experiment is desired. It then appears as the characteristic length in the Reynolds number and scales the viscous effects at the calculation surface. The integration procedure, as with all finite difference techniques, requires values of the fluid flow quantities to be known at discrete points labeled as mesh points. For the present study, these points are arranged on the (θ, ϕ) calculation surface as shown in Figure 2. The mesh points are evenly spaced in the θ and ϕ directions with $\Delta\theta \neq \Delta\phi$. It should be noted that considerable advantage for viscous calculations can sometimes be obtained by varying mesh point spacing to cluster points near the surface. However, only uniform size mesh is considered here since the present study is primarily concerned with proof of an untried assumption for the flow equations. Therefore, the additional complexity involved in obtaining the uneven mesh spacing was not desirable and was not made a part of this study. The mesh spacing used was designed to give entirely adequate results on the lee side of the cone in the large viscous regions present there.

The finite difference mesh is initialized to free stream values of the flow quantities except for surface points at which the three velocity components are set identically to zero. This is physically

equivalent to bringing the cone from rest to the free stream Mach number instantaneously. As might be expected, the initial transients associated with this procedure are quite large and require numerical damping at the higher angles of attack. However, this is not considered detrimental since the damping is required continuously for most of the solutions obtained for reasons which will be discussed later. Also, a comparison between final results obtained with the impulsive start and with a solution obtained by changing slightly the boundary condition representation (thereby perturbing the flow) of a converged solution revealed no essential difference between the two solutions.

The boundary conditions, which are maintained throughout the calculation, are:

(1) All velocities identically zero at the surface.

(2) Surface temperature constant and equal to the value for the experimental case.

(3) Free stream values of all flow quantities are maintained at the outer edge of the mesh. Since the bow shock wave was very close to the cone surface on the windward side for the high α cases, an ellipse was used to provide a dummy outer edge of the mesh which would be close to the bow shock and therefore save computer time.

(4) Lateral symmetry of the flow quantities is maintained across the $\phi = 0°$ and $\phi = 180°$ lines.

The values of pressure and density at the surface are determined during the integration. A discussion of this matter, plus a more complete description of the boundary conditions, appears in Appendix A.

In this study, the predictor and corrector are swept through the (ϕ, θ) mesh in turn, beginning at the $\phi = 0°$, $\theta = \theta_c$ point. A complete traverse of the predictor and corrector constitutes one time step. Step by step, the procedure is as follows:

(1) The predictor is swept through the mesh from $\theta = \theta_c$ to $\theta = \theta_\infty$ and from $\phi = 0°$ to 180°.

(2) The $\vec{D}$ matrix is decoded to obtain updated values of the flow quantities.

(3) The corrector is swept through the mesh, using the updated flow quantities where appropriate.

(4) The $\vec{D}$ matrix is decoded to give values for the flow quantities at the end of the time step.

(5) Boundary conditions are applied where necessary during the integration.

As implied in the stated outer boundary condition, no special provisions are included to handle the bow shock wave or any imbedded shock waves which may arise. These shock waves are "captured" through use of the conservation form of the governing equations (References 10,28). This procedure is considered adequate through use of numerical damping for reducing spurious oscillations around the shock waves (Appendix B).

A criteria for determining when the steady state has been reached (i.e. "convergence") is considered an integral and necessary part of this study. Previous unpublished experience by the author with inviscid flows reveals that instabilities in the calculation can arise even after changes in the flow field pressure become small as seen on a plotter or CRT display device. Therefore, a stringent convergence criteria is used in the present study in order to insure that the solution is stable and that the results obtained are repeatable. The convergence criteria that was used required computation of differences in pressure, density, velocity, and energy between time steps and stopped the calculation when these differences reached the fifth significant figure for all points in the flow field. At the time step sizes used for runs reported here, convergence of the solution typically occurred at the physical time required for the outer flow to move four to five times the length from the nose to the calculation surface. By reducing the number of significant figures input to the convergence routine, it was found that the fifth-place criteria gave run times nearly twice as long as would have been required to obtain values of

surface pressure accurate to engineering standards (Changes of less than 3% occurred in surface pressure during the last 50% of the run). The numerical stability of the present calculations is therefore assured.

The present study did not make continuous use of a stability limit criteria to determine allowable step size. Instead, the time step size for each computer run was frozen at a value which would insure no difficulty with normal stress damping (described in Appendix B). Based on experience gained in the study, a stability criteria was postulated and confirmed by numerical experiment. This entailed repeat of a previous run with time step size automatically determined by applying the criteria noted below at each time step. This stability limit criteria is described in detail in Appendix C. The criteria is summarized here:

$$\Delta t = m \, \text{MIN} \, (\Delta t_{cfl}, \Delta t_{nsd}, \Delta t_{visc}) \tag{14}$$

where $m \leq 1$, $\Delta t_{cfl} \leq \dfrac{1}{\dfrac{|v|}{\Delta\theta} + \dfrac{|w|}{(\sin\theta\Delta\phi)} + c\dfrac{[\Delta\theta^2 + (\sin\theta\Delta\phi)^2]}{\Delta\theta(\sin\theta\Delta\phi)}}^{1/2}$

$$\Delta t_{nsd} = \text{MIN} \; \frac{\rho Re}{2} \frac{\Delta\theta^2}{\left|2 + \dfrac{\beta\lambda}{\mu}\right|}$$

$$\Delta t_{visc} = \text{MIN} \; \frac{\Delta\theta^2 \; (\rho Re \; Pr)}{2\gamma}$$

In this instance, MIN implies the minimum value of the quantity found by searching all mesh points in the flow field. Although m is theoretically limited to 1.0 (the CFL condition), it was found that a value of m = 1.2 could be used once the initial strong transients were past. Instability of the solution occurred at m = 1.4.

The operation sequence used in the computer code was the following:

(1) READ input data

(2) Initialize mesh

(3) DO time steps, 1 to input number

(4) Calculate local Reynolds number

(5) Calculate local damping coefficients

(6) DO predictor for all but free stream boundary mesh points

(a) Calculate coordinate metrics

(b) CALL boundary value subroutine

(c) Define finite difference representations

(d) CALL vector load subroutine (creates $\vec{F}$, $\vec{G}$, and $\vec{H}'$ in Equation 2 according to the requirements of (c) above)

(e) CALL integrations subroutine (creates predicted value of $\vec{D}$ at new time level by application of Equation 11

(f) CALL $\vec{D}$ vector solver subroutine (decodes flow quantities from calculated $\vec{D}$ vector at new time level)

(7) CALL symmetry boundary condition subroutine

(8) DO corrector for all but free stream boundary mesh points (This is an exact duplicate of step (6) except for changes in finite difference representations and flow quantity time levels. The code used the same subroutines for both predictor and corrector sequences.)

(9) CALL symmetry boundary condition subroutine

(10) Test for convergence. If not converged, return to step (3) and continue until convergence criteria is met or the input number of time steps is completed.

(11) Store results

(12) Print and plot results of calculation

(13) STOP

This sequence of operations may be used to integrate (by use of MacCormack's scheme) other three coordinate versions of the flow equations by appropriate changes in steps (6) (b), and (d). The restrictions are that weak conservation form be used and that the independent variable of integration be time or a coordinate direction in which $M \geq 1$.

This completes the description of the approach used in the present study. The following section describes and compares with experimental data the numerical results obtained through application of this approach.

SECTION IV

NUMERICAL RESULTS

This section presents a comparison between results obtained with the present technique, the numerical technique of Lubard and Helliwell, and selected wind tunnel experiments. The first comparison is with the experimental study of Tracy (Reference 30). This study has been a standard of comparison for other techniques (References 14-16) and is very well documented in the open literature. The second comparison is with the experimental study of Stetson (Reference 22) and the third with that of McElderry (Reference 31).

The validity of any heretofore untried assumption applied to the governing equations can only be determined through comparison of the results obtained by calculation with results of experiment. To test the validity of the present technique, experimental data were chosen which had been published and which provided a Mach number range of six to fourteen. The experimental cases chosen were for sharp cones within the limits reasonably obtainable by standard machining techniques (0.001 to 0.002 in. nose radius). Reynolds numbers, except for that of McElderry, were in the range for which laminar flow could be expected. Transition onset in McElderry's data was at approximately $Re = 2.4 \times 10^6$. The cases all have flow field probe data available for selected Reynolds numbers and angles of attack. The remainder of this section will present a detailed comparison of the results of the present calculation with the chosen experimental data.

1. TRACY'S DATA

Tracy (Reference 29) conducted an experimental study using a 10° half angle sharp (0.002 nose radius) cone in M = 7.95 flow. The wind tunnel working fluid was air with total pressure and temperature of 259.3 psia and 1360°R for the runs of interest. The resulting free stream Re was 1.25×10^6/ft. Data were taken at angles of attack of 0° to 24° in 4° increments. Measurements of surface pressure at x = 4.0 in. and surveys of pitot pressure at x = 3.45 in. (and perpendicular to the cone surface) were selected for comparison. The configuration of the model and

instrumentation prevented the acquisition of both types of data at the same x station on the cone surface.

Calculations were performed at the following conditions:

$M = 7.95$	$Re_x = 4.2 \times 10^5$ (x = 4.0 in.)
$P_{t_\infty} = 259.3$ psia	
$T_{t_\infty} = 1360°R$	$T_w/T_{t_\infty} = 0.41$
$\alpha = 0°, 8°, 12°, 20°, 20.5°, 24°$	$Pr = 0.72$

The finite difference mesh contained 48 x 50 points except for the $\alpha = 24°$ case in which a 48 x 70 mesh was used. The circumferential (ϕ) step size was 4° for all runs with the θ step size varying depending on the angle of attack and number of mesh points used. All runs in this study were converged to the fifth significant digit of the flow quantities. Computer run times for these solutions ranged from 1.4 hours ($\alpha = 12°$) to 1.6 hours ($\alpha = 24°$) on the CDC CYBER 74 (equivalent in CPU speed to a CDC 6600). The number of time steps required ranged from 1860 ($\alpha = 8°$) to 2480 ($\alpha = 12°$). The fact that the highest angle of attack run did not take the largest number of time steps is due to variance in the actual CFL condition at which each calculation was made. More consistent results are obtained through use of the stability criteria set forth in Appendix C. In order to provide comparison of both flow field and surface quantities, comparison with experimental data is shown for surface pressure and pitot pressure surveys. In addition, velocity vector plots are shown for the calculations and pictorial displays of cross flow field features are shown in order to compare the overall agreement of the calculation with experiment. (These data were also reported in (Reference 39).

Figures 7 through 10 compare the numerical results of the calculation with the surface pressure data of Tracy. At this point it should be noted that, unless otherwise stated, the discrete points shown for Tracy's data were obtained from continuous curves in Reference 30 through use of a digitizer. Figure 7 gives this comparison for $\alpha = 8°$. The calculated value can be seen to fall just at the edge of the symbols for the entire circumference of the cone. This corresponds to a local

difference of 1.6% at $\phi = 0°$, the windward centerline of the cone. The surface pressure comparison for $\alpha = 12°$ is given in Figure 8. The agreement in this case is somewhat better near the leeward centerline ($\phi = 180°$) but the local difference has increased to 2.5% at $\phi = 0$. The same type of agreement exists for the $\alpha = 20°$ (Figure 9) and $\alpha = 24°$ (Figure 10) cases with the local difference for $\alpha = 24°$ becoming 5% at $\phi = 0°$. To provide a further comparison, the surface pressure at $\phi = 0°$ obtained by Lubard and Helliwell (Reference 16) for the $\alpha = 12°$ case is identical to that obtained in the present study. The first possible reason for the discrepancy between calculation and experiment on the windward side is that Tracy noted an approximate 0.5° uncertainty in angle of attack in the wind tunnel used for the experiment. In order to test this possibility, the $\alpha = 20°$ run was reconverged at $\alpha = 20.5°$. The surface pressure at $\phi = 0°$ regained only 1/2 of the 4.7% difference between the experiment and the $\alpha = 20°$ solution, indicating that not all of the discrepancy could be due to the uncertainty in angle of attack. The second possibility which should be considered is the fact that the surface pressure taps used for the experiment were somewhat large in relation to boundary layer thickness on the windward side. In any case, an error band of at least 5% is present in most experimental studies.

Sample circumferential pitot surveys are presented in Figures 11 through 13. The angle in the θ direction for comparison with experiment is defined by

$$\theta = \theta_c + \tan^{-1}\left[\frac{y}{3.45"}\right] \tag{15}$$

where y is the normal distance above the cone surface in inches. The Reynolds number for the calculated results is 4.2×10^5. Since the pitot surveys were made at constant height above the cone surface, they will in most cases intersect the bow shock at some point in the circumferential traverse. This appears in the pitot pressure plots as a sharp rise from the free stream value (8.7×10^{-3}) to the maximum value for each trace. Probe effects cause the character of the rise of

experimental pitot pressure to appear remarkably like that of the rise of pitot pressure through the captured shock waves obtained in the present study, with decrease in transition slope and loss of peak pressure in the calculations caused by the necessary damping present. Note that the pitot pressure transition centerpoint (the shock location criteria used by Tracy) of the captured shock in all of the calculated results is virtually the same as would be determined from the experimental pitot survey and that the calculated pitot pressure quickly returns to the proper magnitude on the high pressure side of the shock. For the $\alpha = 12°$ case (Figure 11), the uppermost survey ($y = 0.4$ in.) is entirely in the inviscid flow region for both calculation and experiment. The survey nearest the cone surface ($y = 0.05$ in.) is in the viscous layer for more than 90° of the circumference of the cone. Agreement with experiment for both of these surveys is good. The calculated center survey ($y = 0.2$ in.) departs from the experimental value near the lee centerline ($\phi = 180°$). This departure is due to the smaller viscous layer present in the calculation as compared to experiment.

The $\alpha = 20°$ case (Figure 12) has essentially the same degree of agreement between the calculated results and experiment with the exception that the departure near the lee centerline is concentrated in a region of approximately 6° ($\phi = 174° - 180°$). Agreement outside this region is generally good. Figure 13 illustrates that essentially the same agreement and region of discrepancy exist for the $\alpha = 24°$ case.

The pitot pressure discrepancy near the lee centerline can be evaluated more clearly from Figure 14, which compares pitot pressure along the lee centerline for the $\alpha = 24°$ case. The discrepancy, as noted above, extends for approximately 6° to either side of the lee centerline for this angle of attack. It is attributed to a combination of locally large pitot pressure drop due to finite model nose radius and to nose effects resulting from the non-conical region at the nose. Any persistent experimental nose effects would tend to be concentrated along the lee centerline as they are swept back along the cone. This phenomenon can be observed in the experimental study of Stetson (Reference 22) through examination of the oil flow pictures presented

therein. For instance, Figure 12 of Reference 22 shows a near conical cross flow separation originating at approximately 16% of the cones length from the nose. As can be observed from the oil flow traces prior to this point, the flow originating at or near the nose has been swept around the cone to the lee side by the time the 16% point has been reached. Since the flow is primarily axial on the lee side after the cross flow separation begins, the results of the effective blunting and the non-conical region near the nose remain at or near the lee centerline as the flow continues along the cone.

To demonstrate the pressure distribution obtained through the shock layer, Figure 15 shows static pressure in the θ direction at 60° intervals around the cone for the α = 12° case. The elevation above the cone surface is given in radians in this and subsequent computer generated plots. As noted in Appendix B, the damping was not tailored in the θ direction for these runs, so excess smearing of the shock is evident on the free stream side. No appreciable harm is seen to result from this smearing.

The velocity vector plots in Figures 16 through 18 provide an indication of cross-flow streamline patterns and illustrate the relative magnitude of cross-flow velocity for all but the lowest momentum regions. The reverse flow region is thin in the α = 12° case (Figure 16) with the vortical singularity (defined for this study as the cross flow stagnation point toward which streamlines converge) occurring near the edge of the viscous layer 3.2° above the cone surface. The cross-flow separation point is at ϕ = 163° with the experimental point occurring at ϕ = 156°. This difference is attributable to lack of resolution of the reverse flow region at this angle of attack in the present study, as both Lin and Rubin, and Lubard and Helliwell obtained a separation point nearer that of the experimental data. This was supported in the present study by the fact that the separation points in the higher α runs (with more mesh points in the reverse flow regions) were virtually identical to those of experiment.

At $\alpha = 20°$ (Figure 17) the extent of the reverse flow region and the position of the cross-flow separation point have reached limiting values, as no substantial changes in these can be seen in the $\alpha = 24°$ run (Figure 18). This was noted for the separation point in both experiment and theory by Lin and Rubin (Reference 15). However, the extent of the viscous region and the location of the vortical singularity (as determined in the present study) continue to change as α increases. The vortical singularity is near the edge of the viscous layer for all cases in the present study in which it is lifted off the cone surface.

Although agreement with experiment so far has been shown to be good, perhaps the best evaluation of the validity of the conical flow assumption for engineering solutions can be made through a pictorial representation of the flow field features. Figures 19 and 20 compare the overall results of the present study with the calculation of Lubard and Helliwell and Tracy's data. As shown in Figure 19, the position of the bow shock and viscous layer edge of the present study for this case are essentially those obtained by Lubard and Helliwell. Both numerical studies result in a shock position too near the cone and a thinner viscous layer at this α when compared with experiment. This is considered to be primarily due to the failure to account for nose tip effects as noted previously. A weak supersonic region is present in the cross-flow plane and is shown by the solid lines between viscous layer and bow shock. The vortical singularity position is shown by the open oval symbol on the lee centerline. The structure of the $\alpha = 24°$ case is more interesting (Figure 20). Supersonic cross-flow is seen to exist over most of the field and is terminated by a complex sonic line/shock wave. The position of this line is nearer the lee centerline than shown by Tracy. The small amplitude oscillations present on the imbedded sonic line/shock as it nears the bow shock can be seen (through careful examination of Figure 18) to be caused by oscillations (in velocity) propagating through the supersonic cross-flow region from the vicinity of the bow shock. The ϕ grid spacing used in the present study did not give sufficient resolution to determine the existence of the lambda portion of the imbedded shock, as shown by Tracy. However, its signature may be surmised in the hump

present in the calculated viscous layer edge at an angle of approximately 30° from the lee centerline. The curious flat top present in the calculated viscous layer edge as compared to experiment is again attributed to the failure of the numerics to model non-conical nose effects.

In summary, the present technique is seen to model all features present in the experimental study, with the exception of the non-conical nose effects. The computer times are not excessive since they are based on a very stringent convergence criteria and represent an increase in time per mesh point calculated of only 40% over a comparable inviscid computer program.

2. STETSON'S DATA

Stetson (Reference 22) conducted an experimental study using a 5.6° half angle sharp (0.001 in. nose bluntness) cone in M = 14.2 flow. The wind tunnel working fluid was air with total pressure of 1600 psia and a total temperature of 2050°R. The resulting free stream Re is given as 0.62×10^6/ft. Data were taken at angles of attack of 0° to 14° in 2° increments (plus a run at 5°). Measurements of surface pressure were made at a number of stations along the cone, and pitot surveys were made perpendicular to the free stream velocity at x/L = 0.87 for $\alpha = 10°$.

A calculation was made at the following conditions:

$M = 14.2$ $\qquad$ $Re_x = 7.9 \times 10^5$ (x/L = 0.75,

$P_{t_\infty} = 1600.0$ psia $\qquad$ L = 15.37 in.)

$T_{t_\infty} = 2050°R$ $\qquad$ $T_w/T_{t_\infty} = 0.29$

$\qquad$ $Pr = 0.72$

The finite difference mesh contained 48 x 50 points with the circumferential step size being 4° as for the previous calculations. The computer run time (with convergence criteria as before) was 2.2 hours of CDC 6600 time for 2700 time steps. In order to provide comparison of both flow field and surface quantities, plots of calculated results versus experimental data are shown for surface pressure and selected cuts through the pitot pressure surveys. Also, a velocity vector plot

of the calculated results is shown. A plot of surface pressure compared with Stetson's data comprises Figure 21. The agreement with experiment is quite reasonable with the maximum difference of approximately 16% (as compared with local static pressure) occurring in the vicinity of the pressure minimum. Pressure scale expansion in Figure 21 and the low absolute magnitude of pressure in this region make the agreement appear less adequate than actually exists. The complete circumferential pressure distribution is qualitatively comparable to that of Figure 9. The surface pressure scale of Figure 21 is equivalent to 0.0 to 0.6 on Figure 6. The calculated cross-flow separation point (26° from lee centerline) agrees quite well with the experimental value (27° from lee centerline).

Pitot pressure comparisons at three ϕ stations on the lee side of the cone are given in Figures 22 through 24. The first comparison at $\phi = 180°$ (Figure 22) shows a large difference in position (approximately 27% at the bow shock) between given levels of pitot pressure for the calculation and experiment. Although the same phenomenon was noted in Tracy's $\alpha = 24°$ case (Figure 14), the difference was small at the edge of the viscous layer and the calculated bow shock was displaced very little from the experimental position. However, in the present case, the bow shock is displaced nearly as much as the edge of the viscous layer. This displacement can be seen to persist (although much smaller in magnitude) through $\phi = 160°$ (Figure 23) until by $\phi = 140°$ (Figure 24), the agreement is nearer that expected from previous results. In all three plots of pitot pressure, the trends as shown by the calculation are essentially correct. The remaining question then concerns the possible reason for the discrepancy between the calculated and experimental viscous layer thickness.

Several possibilities for the cause of the viscous layer discrepancy should be examined. It should first be noted that the perfect gas assumption results in a somewhat higher Reynolds number than is quoted in Reference 22 (0.83×10^6 vs. 0.62×10^6). Since this would result in a somewhat thinner viscous layer for the calculation, the Reynolds number was lowered 20% and the run was reconverged. The change in

shock position on the leeward side was a maximum of 0.25° (as might have been expected for this small change in Re). The resulting small change in shock position indicated that a change in Re of at least an order of magnitude would be necessary for better agreement. A more likely candidate for at least part of the discrepancy in viscous thickness is the effective viscous nose blunting present in the experiment. This is clearly shown in Figure 25 (taken from Reference 22) and would account for at least one-fourth of the discrepancy (assuming no change in bow shock angle, which of course could not be guaranteed).

The value of $\overline{\chi}$ for this calculation was 3.22. Without further information concerning the source of the viscous layer discrepancy, this higher value of $\overline{\chi}$ must be viewed as an indication that the discrepancy will be encountered. (According to Figure 6, divergence of the present technique from weak interaction theory was noted at $\overline{\chi} = 1.55$ for Tracy's conditions).

To illustrate the features of the flow, a plot of cross-flow velocity vectors comprises Figure 26. This plot illustrates that the lee side vortices and the vortical singularity which existed in Tracy's cases exist here also. The vortical singularity occurs near the edge of the viscous layer as before.

In summary, the calculation is seen to model the features and trends present in Stetson's experimental study with the only apparent difficulty being the failure to correctly predict lee side viscous layer thickness and shock position. The maximum difference of approximately 27% occurred at the lee centerline ($\phi = 180°$).

3. McELDERRY'S DATA

McElderry (Reference 31) analyzed experimental data taken for a 6° half angle sharp cone 38.06 inches in length in M = 6.05 flow. It should be noted that these data also appear in Reference 32 by Rhudy and Baker. The wind tunnel working fluid was air with total pressure of 280.0 psia and a total temperature of 850°R. The resulting free stream Re was given as 5.0×10^6/ft. Data were taken at angles of attack of 0° to 12°

in 3° increments. Surface pressure measurements were made at several locations along the cone with pitot surveys made perpendicular to the cone centerline at x/L = 0.75 and 0.97. Heat transfer data were taken on a thin walled model and were used to locate the boundary layer transition region on the cone. References to transition contained in the remainder of the discussion of these data are based on the transition location analysis presented in Reference 31. At the experimental free stream Reynolds number of 5×10^6/ft , transition was essentially complete on the lee side by x/L ≈ 0.3. Since the surface pressure measurement nearest the tip was at x/L = 0.31, nearly all lee side pressure data were taken in the turbulent flow region.

The first attempts made to calculate this case were at a Reynolds number of 15.0×10^6 which corresponds to the fully turbulent flow region near the base of the cone. As expected, the very thin boundary layer present at this Reynolds number created extreme difficulty in the vicinity of the interaction with the lee side imbedded shock wave. (The flow at this Reynolds number, when considered without provision for turbulence modeling, could be characterized as nearly inviscid and therefore contains some of the difficulties encountered with the inviscid solution). No combination of damping and step size was found which would lead to convergence at the above Reynolds number. The Reynolds number was then reduced by a factor of ten to 1.5×10^6 and the run was successfully completed. This reduced Reynolds number corresponds to a station on the cone just prior to the onset of transition (as determined in the experimental study) at the noted angle of attack and therefore was in a region where the laminar flow equations were still valid.

The conditions for the successful run were:

$M = 6.05$ $\qquad$ $Re_x = 1.5 \times 10^6$ $\quad (x \simeq 4$ in.)

$P_{t_\infty} = 280.0$ psia $\qquad$ $T_w/T_{t_\infty} = 0.61$

$T_{t_\infty} = 850°R$ $\qquad$ $Pr = 0.72$

$\alpha = 12°$

The finite difference mesh contained 48 x 50 points with the ϕ step size being 4° as before. Since considerable experimentation with time step size and damping factor was necessary during this run, the computer time of 2.3 hours was more than would be required for a rerun of this or a similar case.

The initial behavior of this solution was essentially the same as that for the higher Reynolds number mentioned above. That is, the lee side imbedded shock is strong until very near the cone surface (due to the thin viscous layer). This resulted in a strong compression in the vicinity of the cone surface which was then followed by an overexpansion and then a recompression to the cone lee centerline point (ϕ = 180°). Although this appeared to be a persistent solution to the governing equations as numerically approximated, the overexpansion became strong enough to drop pressure (and thereby temperature) below zero which then destroyed the calculation. Since normal stress damping was found to be effective in damping starting transients in the lee side region for Stetson's data, it was also tried here. After some experimentation, it was found that the overexpansion could be controlled (and eventually made to disappear entirely) by a damping factor of 225.0 in the θ direction and 100.0 in the ϕ direction. These factors are scaled by the Reynolds number and therefore correspond to factors of 63.0 and 28.0 respectively at Tracy's Reynolds number. In contrast to the use of damping to control starting transients, the damping in this case could not be removed as the overexpansion would then reappear. The above damping factors were then maintained until the solution converged. Since the maintenance of normal stress damping in the viscous layer may shift the density distribution through the layer somewhat, changes in the agreement with experiment might be expected.

Unfortunately, experimental measurements were not made far enough forward on the cone to provide comparison with the calculated solution at the same Reynolds number. The first surface pressure measurements were at x/L = 0.31 at which point transition was essentially complete on the lee side at 12° angle of attack. The dual lee side separations associated with turbulent flow were present in the experiment at the

x/L = 0.31 point indicating that the comparison could not possibly be exact as the calculation only had the single cross-flow separation which is generally associated with laminar flow. However, this calculation provides a unique opportunity to examine the adequacy of the conical symmetry assumption for turbulent flow. It can be postulated that if the conical symmetry assumption is to be valid in the turbulent regime, an examination of the flow field just prior to the start of transition would differ only in the details of the viscous layer when compared conically with a measurement far downstream of transition. To test this hypothesis, a comparison of the calculation (x/L = 0.10, Re = 1.5×10^6) to the experimental surface pressure (x/L = 0.955, Re = 15.0×10^6, Reference 31) and selected pitot surveys (x/L = 0.75, Re = 12.0×10^6, Reference 32) is shown in Figures 27 through 29. In this instance, a conical comparison implies examining flow quantities at two distinct spherical radii (points A and B of Figure 1) on each of a series of rays passing through the vertex of the cone. If the flow quantities have nearly the same vector and scalar values at points A and B on a majority of the rays, then the flow is essentially conical in character. In the present comparison, point A corresponds to the calculated values at a point on the cone upstream of transition and point B corresponds to the experimental measurements downstream of transition.

The experimental surface pressure at x/L = 0.955 is shown conically compared with the calculated values in Figure 27. The agreement is quite good in both trend and absolute value until the vicinity of the experimental primary separation at $\phi = 126°$ is reached. From this point on toward the lee centerline, the absolute value of the pressure shows varying agreement with experiment. The calculated separation point ($\phi = 163°$) is near the experimental secondary separation point ($\phi = 166°$). To place the conical comparison in perspective, the agreement of the present calculation with experiment is far better than is obtained by the inviscid techniques shown in Reference 31.

Pitot pressure surveys for both calculation and experiment normal to the cone centerline are presented in Figures 28 through 30. The first survey is at $\phi = 180°$ (Figure 28). Both experiment and calculation are

characterized by very high speed flow prevailing nearly to the cone surface. For example, the first two mesh points above the surface in the calculation have local Mach numbers of 5.0 and 5.9, respectively. The oscillations occurring between 1.0 and 2.0 inches in the calculation are numerical. However, the apparent oscillation in the calculation occurring between 0.0 and 1.0 inch is in reality the solutions reflection of the fact that a high speed "jet" of flow occurs (as evidenced by the high local Mach numbers noted above) on the lee centerline under the contra-rotating vortices. The existence of this jet is confirmed by examination of Figure 31 which shows the calculated Mach number distribution along lines of constant ϕ. The vortex structure is seen to be centered at $\phi \simeq 170°$. The local Mach number clearly increases at the first two mesh points above the surface as the lee centerline ($\phi = 180°$) is approached. The apparent oscillation on the $\phi = 180°$ line between 0.0 and 1.0 inch is in reality an indication of vortex position. This region of high speed flow can also be readily seen in the pitot maps in Reference 32 at x/L = 0.97. However, the resolution of the lines of constant pitot pressure is insufficient for the x/L = 0.75 surveys in Reference 32 to be able to plot with certainty this "jet" in the experimental data on the graph shown here. The pitot survey at $\phi = 160°$ (Figure 29) shows much the same trend as the $\phi = 180°$ survey except for lower momentum flow near the surface and a slightly thinner viscous layer in the calculation than in the experiment. At $\phi = 140°$ (Figure 30) the conical agreement of the calculation with experiment is very good.

The global conical agreement with experiment can be examined through the characteristics of the cross-flow velocity vector plot in Figure 32. One immediately obvious feature of this plot is that the vertical singularity is not lifted off the surface even though the angle of attack is twice the cone half angle. This is in reality evidence of the fact that the viscous layer instead of having a large hump on the lee side now has a "cusp" at the lee centerline with a nearly sharp local minimum in viscous layer thickness. The experimentalist have observed this behavior of the viscous layer edge and it has been noted in vapor screens and pitot surveys taken in turbulent flow on cones in References 31, 33, and 34 (see Figure 33 taken from Reference 33). Also, comparing the extent of

the lee side vortices present in the laminar region calculation with the pitot maps in References 31 and 32, it is apparent that the essential size and character of the primary vortices are maintained through transition and beyond.

The differences in the characteristics of the viscous layer and surface pressure distribution with increased Reynolds numbers are graphically and pictorially shown in Figure 33 which is taken from Reference 33. The "cusp" viscous layer structure shown in Figure 33 for Rainbird's experimental results has been considered to be primarily a turbulent flow regime phenomenon on conical bodies. However, the calculation made at McElderry's conditions in the present study demonstrates that the "cusp" is present in the viscous layer upstream of transition. The viscous layer structure of Rainbird shown in Figure 33 is therefore a phenomenon occurring in the laminar flow regime which persists into the turbulent regime.

In summary, the solution at a location on the cone just upstream of the boundary layer transition location is shown to exhibit features previously associated with turbulent flows over conical bodies. The agreement of this solution with experiment is amazingly good when it is compared conically with experimental measurements made far downstream in the turbulent flow regime. The adequacy of the conical symmetry assumption for turbulent flow is therefore assured if a reasonable means can be found to model viscous layer turbulence.

SECTION V

CONCLUSIONS

Inviscid computations for hypersonic cone flow have proven to be unstable at angles of attack greater than twice the cone half angle. In addition, previously obtained solutions including the effects of viscosity have required input of experimentally obtained data and/or have not been demonstrated for $\alpha/\theta_c > 2.0$.

In order to resolve these difficulties, solutions have been demonstrated for the complete flow field around sharp cones including viscous effects. These solutions were obtained by applying a conical symmetry assumption to the complete Navier-Stokes equations and numerically integrating the resulting equation set by use of MacCormack's finite difference scheme. Integrations were performed at selected sets of boundary conditions for which previously published experimental data were available. The solutions obtained were for a Mach number range of 6.05 to 14.2, a local Reynolds number range of 0.4×10^6 to 1.5×10^6, and angles of attack from $\alpha/\theta_c = 0.0$ to 2.4. Stability of the solutions was demonstrated through use of a stringent convergence requirement. A technique (normal stress damping) was developed and used to reduce or eliminate the numerical oscillations which developed during the integration in the vicinity of strong shock waves. The results of the integration were compared with the experimental studies of Tracy, Stetson, and McElderry. The following points are presented concerning the conduct of the integration and the comparison with experiment:

(1) Agreement with the experimental data of Tracy was generally good. The major features of the experiment (shock waves, sonic lines, and viscous layers) were present and essentially correct in location and magnitude in the results of the integration. The primary discrepancies noted in the comparison with Tracy's data were an approximate 5% difference in surface pressure near the windward centerline and an error in pitot pressure in a small region near the lee centerline for the $\alpha/\theta_c \geq 2.0$ cases. The latter discrepancy was concluded to be due to

failure of the present technique to account for non-conical nose effects. Agreement of the results of the integration with the experimental data of Stetson was less adequate than was shown to exist with the data of Tracy. The agreement with Stetson's surface pressure measurements was quite reasonable. However, the position of the lee side shock wave in the results was 27% nearer the cone surface at the lee centerline than in the experiment. This discrepancy was concluded to be primarily caused by inability of the present technique to model the effective nose blunting existing in the experiment which resulted from viscous effects at this high Mach number (14.2). The apparent effect of this nose blunting was much greater in extent in Stetson's case (hypersonic similarity parameter, $\overline{\chi} \simeq 3.0$) than in Tracy's cases ($\overline{\chi} \simeq 1.0$).

(2) The present technique removes the angle of attack limitations present in inviscid calculations. The instabilities associated with the point where the high strength lee side imbedded shock wave reaches the surface are removed by the inclusion of viscous effects in the physical modeling of the flow field.

(3) The adequacy of the conical symmetry assumption is indicated for the turbulent regime on conical bodies. A solution obtained just prior to the beginning of boundary layer transition at the experimental conditions of McElderry agrees well with experiment when conically projected far into the turbulent regime.

(4) Normal stress damping is shown to provide a physically based means to provide the necessary control of spurious numerical oscillations around shock waves without additional computer time. It is also very effective for control of overexpansion and for control of starting transients due to ill-suited initial conditions.

In summary, the present technique was shown to be a viable means of calculating the flow over cones at angle of attack including viscous effects. Agreement with experiment was quite good for $\overline{\chi} \leq 1$ with some discrepancy encountered in the lee side viscous layer as $\overline{\chi}$ increased.

Angle of attack limitations encountered with the inviscid equations were removed. This technique should therefore be considered as an alternative to the use of the inviscid flow equations for future calculations of flow over conical bodies.

SECTION VI

RECOMMENDATIONS

Three primary directions are seen for extension of the work presented in this report. The first is the confirmation of the technique for more general conical configurations, such as delta wings. The second is the extension of the Reynolds number range for which the calculations can be accomplished through inclusion of a turbulence model in the formulation of the equation set. The third is the investigation of the adequacy of the conical symmetry assumption for lower supersonic Mach numbers.

A further item pointed out by this study is the need for re-examination by the experimentalist of the techniques used for collection of experimental data. As the numerical computation capability improves, heretofore undetected discrepancies in data collection techniques may be pointed out. An example is the underestimation of surface pressure on the windward side of the cone in the present study. This underestimation in past inviscid studies was attributed to failure to include viscous effects. However, two studies (the present study and Reference 16) are available which exhibit this underestimation even though viscous effects were included in the calculated results. A third study (Reference 14) matched the windward surface pressure for Tracy's data only at a much lower Reynolds number than existed in the data. This is considered to be a clear indication that the details of the use of surface pressure taps where thin hypersonic boundary layers exist should be further studied. This also points out the need for cooperation and collaboration between the experimentalist and the numericist in the effort to improve overall aerodynamic prediction techniques.

REFERENCES

1. G. I. Taylor and J. W. Maccoll, "The Air Pressure on a Cone Moving at High Speed," Proceedings of the Royal Society (A), Vol. 139 (1933), p 278.

2. Z. Kopal, "Tables of Supersonic Flow Around Cones," M.I.T. Center of Analysis Technical Report No. 1, 1947.

3. Z. Kopal, "Tables of Supersonic Flows Around Yawing Cones," M.I.T. Center of Analysis Technical Report No. 3, 1947.

4. Z. Kopal, "Supersonic Flow Around Cones of Large Yaw," M.I.T. Center of Analysis Technical Report No. 5, 1947.

5. A. Ferri, "Supersonic Flow Around Circular Cones at Angles of Attack," National Advisory Committee for Aeronautics Report No. 1045, 1951.

6. K. I. Babenko, et al., "Three-Dimensional Flow of an Ideal Gas Past Smooth Bodies," NASA Technical Translation TT F-380, 1964.

7. I. O. Bohachevsky and E. L. Rubin, "A Direct Method for Computation of Nonequilibrium Flows with Detached Shock Waves," AIAA Journal, Vol. 4, 1966, p 600.

8. D. D. Lax and B. Wendroff, "Systems of Conservation Laws," Communications on Pure and Applied Mathematics, Vol. 13, 1960, p 217.

9. R. W. MacCormack, "The Effect of Viscosity in Hypervelocity Impact Cratering," AIAA Paper 69-354, 1969.

10. P. Kutler and H. Lomax, "A Systematic Development of the Supersonic Flow Fields Over and Behind Wings and Wing-Body Configurations Using a Shock Capturing Finite Difference Approach," AIAA 9th Aerospace Sciences Meeting, New York, AIAA Paper 71-99, 1971.

11. P. Kutler, W. A. Reinhardt, and R. F. Warming, "Numerical Computation of Multishocked Three-Dimensional Supersonic Flow Fields with Real Gas Effect," AIAA 5th Fluid and Plasma Dynamics Conference, Boston, MA, AIAA Paper 72-702, 1972.

12. P. Kutler, H. Lomax, and R. F. Warming, "Computation of Space Shuttle Flow Fields Using Noncentered Finite Difference Techniques," AIAA Journal, Vol. 11, No. 2, Feb. 1973, p 196-204.

13. P. Kutler, L. Sakell, and G. Aiello, "On the Shock on Shock Interaction Problem," AIAA 7th Fluid and Plasma Dynamics Conference, Palo Alto, CA, AIAA Paper 74-524, 1974.

14. T. C. Lin and S. G. Rubin, "Viscous Flow Over a Cone at Moderate Incidence - 1 Hypersonic Tip Region," Computers and Fluids, Vol. 1, 1973, p 37-57.

REFERENCES (CONTINUED)

15. T. C. Lin and S. G. Rubin, "Viscous Flow Over a Cone at Moderate Incidence, Part 2, Supersonic Boundary Layer," Journal of Fluid Mechanics, Vol. 69, Part 3, 1973, p 593-620.

16. S. C. Lubard and W. S. Helliwell, "Calculation of the Flow on a Cone at High Angle of Attack," AIAA 6th Fluid and Plasma Dynamics Conference, Palm Springs, CA, AIAA Paper 73-636, 1973.

17. R. E. Melnik, "Vortical Singularities in Conical Flow," AIAA Journal, Vol. 5, No. 4, April 1967, p 631-637.

18. A. M. Kuethe and J. D. Schetzer, Foundation of Aerodynamics, New York: John Wiley and Sons, Inc., 1967, p 340.

19. P. Kutler, "Numerical Solution for the Inviscid Supersonic Flow in the Corner Formed by Two Intersecting Wedges," AIAA 6th Fluids and Plasma Dynamics Conference, Palm Springs, CA, AIAA Paper 73-677, 1973.

20. C. A. J. Fletcher, "GIT Method Applied to Cones at Large Angles of Attack," Proceedings of the Fourth International Conference on Numerical Methods in Fluid Dynamics, Lecture Notes in Physics 35, Berlin: Springer Verlag, 1974, p 161-166.

21. E. J. Cross, Jr., "Experimental and Analytical Investigation of the Expansion Flow Field Over a Delta Wing at Hypersonic Speeds," ARL 68-0027, 1968, Aerospace Research Laboratories, Wright-Patterson AFB, OH, February 1968.

22. K. F. Stetson, "Experimental Results of Laminar Boundary Layer Separation on a Slender Cone at Angle of Attack at M_∞ = 14.2," ARL 71-0127, Aerospace Research Laboratories, Wright-Patterson AFB, OH, August 1971.

23. R. E. Feldhuhn, "An Experimental Investigation of the Flow Field Around a Yawed Cone," AIAA Journal, Vol. 9, No. 6, June 1971, p 1074-1081.

24. D. A. Anderson, "Comments on Numerical Solution of the Axial Corner Flow Problem for Laminar Flow," Private communication.

25. R. W. MacCormack and B. S. Baldwin, "A Numerical Method for Solving the Navier-Stokes Equations with Applications to Shock-Boundary Layer Applications," AIAA 13th Aerospace Sciences Meeting, Pasadena, CA, AIAA Paper 75-1, 1975.

26. C. M. Hung and R. W. MacCormack, "Numerical Solutions of Supersonic and Hypersonic Laminar Flows Over a Two-Dimensional Compression Corner," AIAA 13th Aerospace Sciences Meeting, Pasadena, CA, AIAA Paper 75-2, 1975.

REFERENCES (CONCLUDED)

27. J. S. Shang and W. L. Hankey, Jr., "Numerical Solution of the Navier-Stokes Equations for Supersonic Turbulent Flow Over a Compression Ramp," AIAA 13th Aerospace Sciences Meeting, Pasadena, CA, AIAA Paper 75-4, 1975.

28. M. Vinokur, "Conservation Equations of Gasdynamics in Curvilinear Coordinate System," Journal of Computational Physics 14, 1974, p 105-125.

29. R. N. Cox and L. F. Crabtree, Elements of Hypersonic Aerodynamics, London: The English Universities Press Ltd, 1965, p 195-200.

30. R. R. Tracy, "Hypersonic Flow Over a Yawed Circular Cone," California Institute of Technology, Aeronautical Laboratories Memorandum Number 69, 1963.

31. E. D. McElderry, Jr., "An Experimental Study of Sharp and Blunt 6 Degree Cones at Large Incidence with a Turbulent Boundary Layer at Mach 6," Air Force Flight Dynamics Laboratory, AFFDL-TM-74-170, 1974.

32. R. W. Rhudy and S. S. Baker, "Surface and Flow-Field Pressure and Heat-Transfer Measurements on a Yawed 6 - Deg Cone at Mach Number 6," Arnold Engineering Development Center, AEDC-TR-72-199, 1972.

33. H. Whitehead, Jr., J. N. Hefner, and D. M. Ras, "Lee Surface Vortex Effects Over Configurations in Hypersonic Flow," AIAA 10th Aerospace Sciences Meeting, San Diego, CA, 1972.

34. W. J. Rainbird, "The External Flow Field About Yawed Circular Cones," AGARD Conference Proceedings Number 30, AGARD Specialists Meeting on Hypersonic Boundary Layers and Flow Fields, The Royal Aeronautical Society, London, 1-3 May 1968, p 19-1 to 19-19.

35. W. F. Ames, Nonlinear Partial Differential Equations in Engineering, New York: Academic Press, 1965, p 478.

36. R. W. MacCormack, "Numerical Solution of the Interaction of a Shock Wave with a Laminar Boundary Layer," Lecture Notes in Physics, Vol. 8, New York: Springer-Verlag, 1971, p 151.

37. R. D. Richtymer and K. W. Morton, Difference Methods for Initial Value Problems, 2nd Edition, New York: Interscience Publishers, 1967.

38. P. J. Roache, Computational Fluid Dynamics, Hermosa Publishers, P. O. Box 8172, Albuquerque, NM, 1972.

39. D. S. McRae, "A Numerical Study of Supersonic Viscous Cone Flow at High Angle of Attack," AIAA 14th Aerospace Sciences Meeting, Washington, DC, AIAA Paper 76-97, 1976.

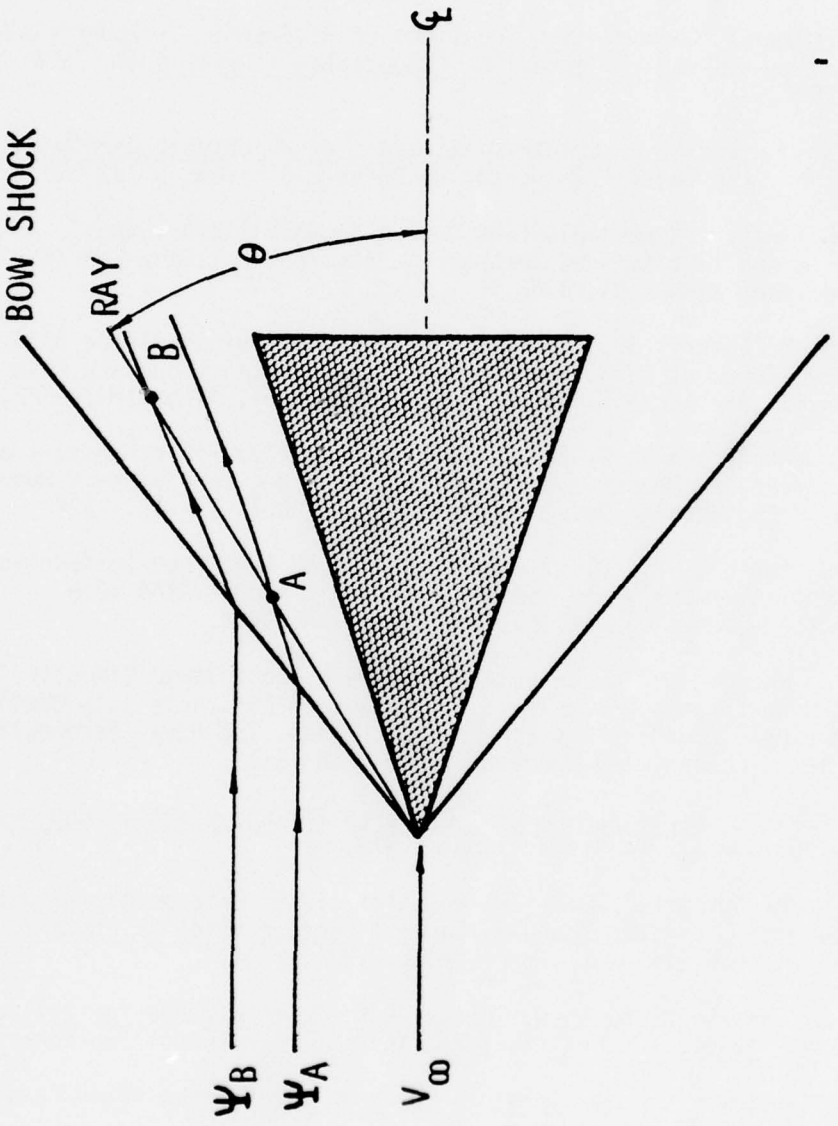


Figure 1. Cross Section of Supersonic Inviscid Flow About Cone at $\alpha = 0°$

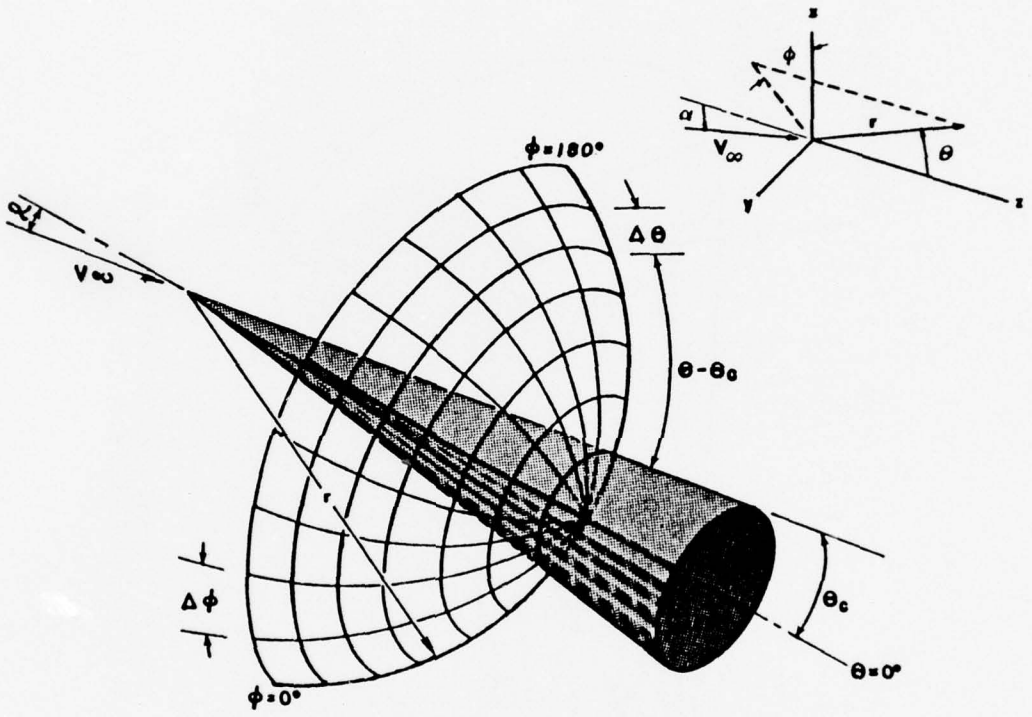


Figure 2. Coordinate System and Computational Mesh Shown in Relation to Cone

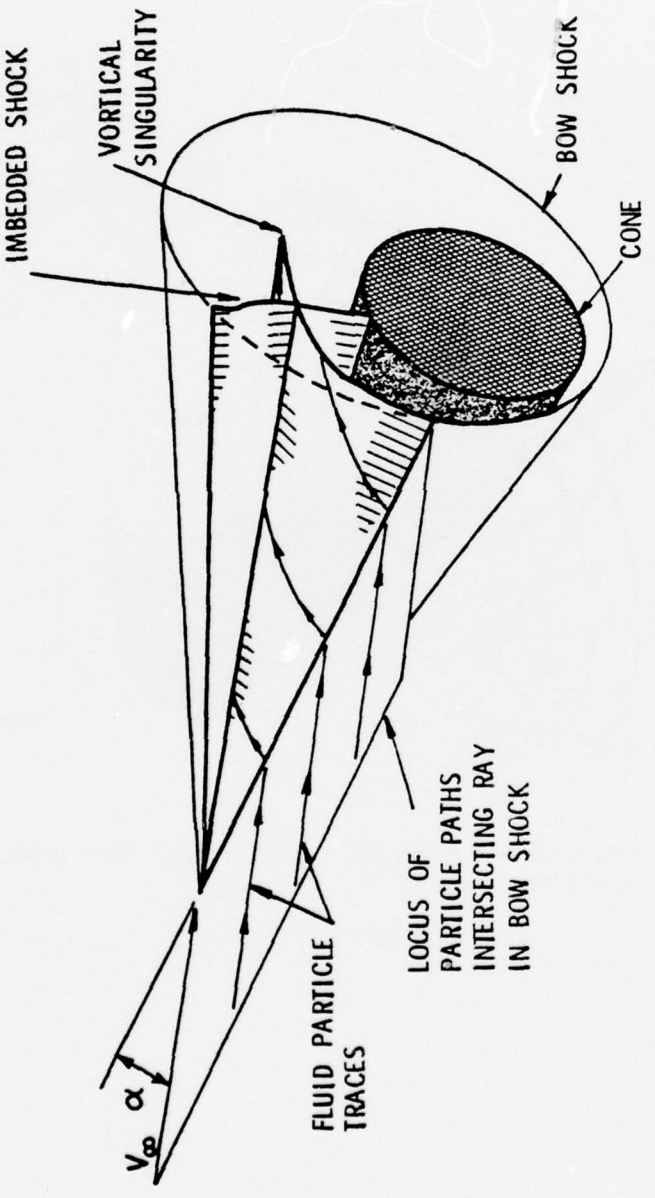


Figure 3. Cutaway Drawing Showing Typical Particle Paths for Supersonic Inviscid Flow About Cone at High α

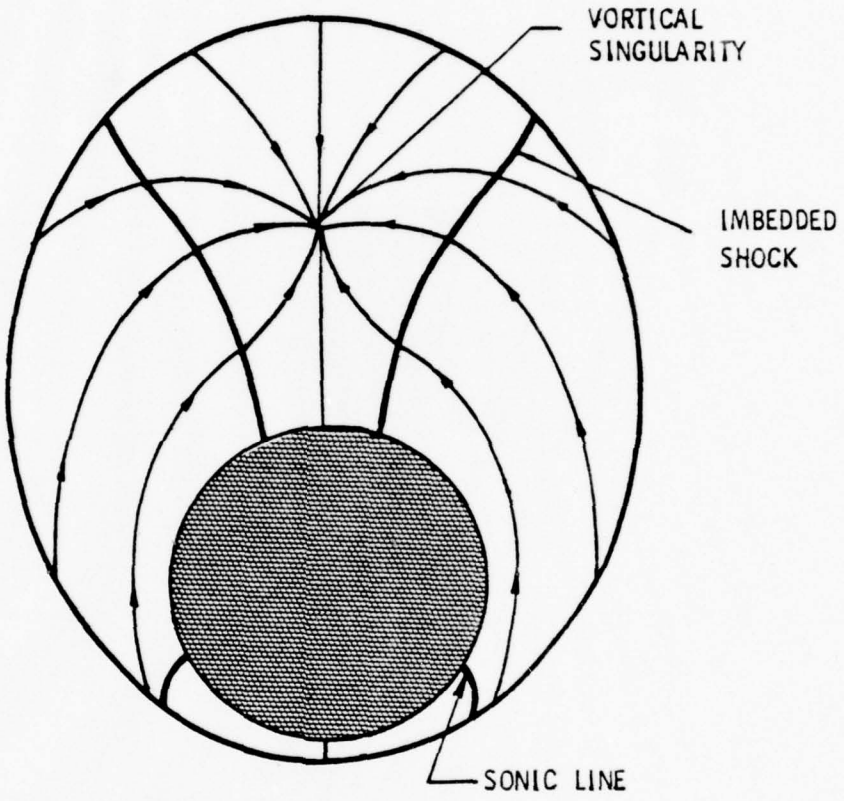


Figure 4. Approximate Cross-Flow Streamline Pattern for Cone at High α

Figure 5. Physical Implications of Conical Symmetry Assumption Illustrating Relationship of Viscous Layer Edge and Spherical Radius

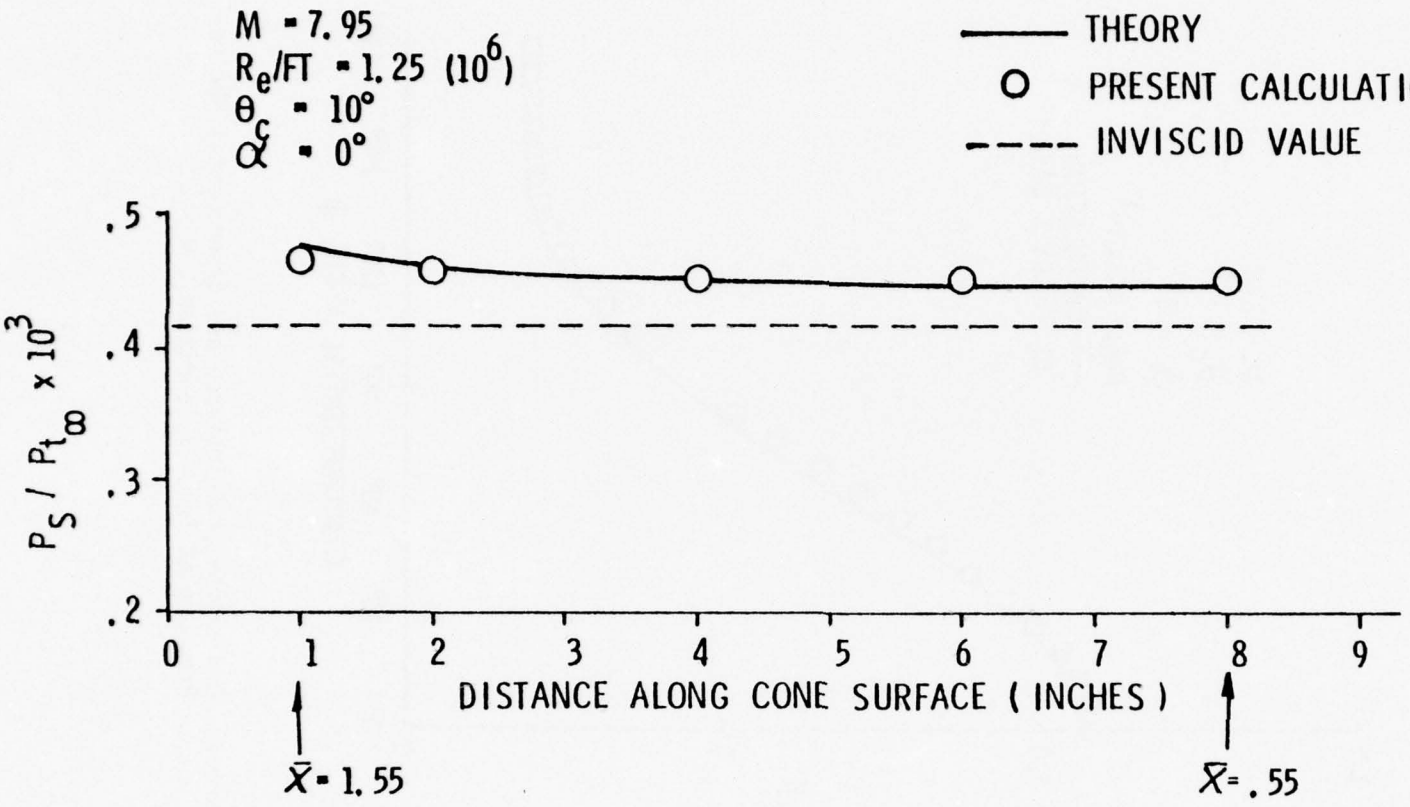


Figure 6. Comparison of Calculated Cone Surface Pressure with that Obtained from Hypersonic Weak Interaction Theory

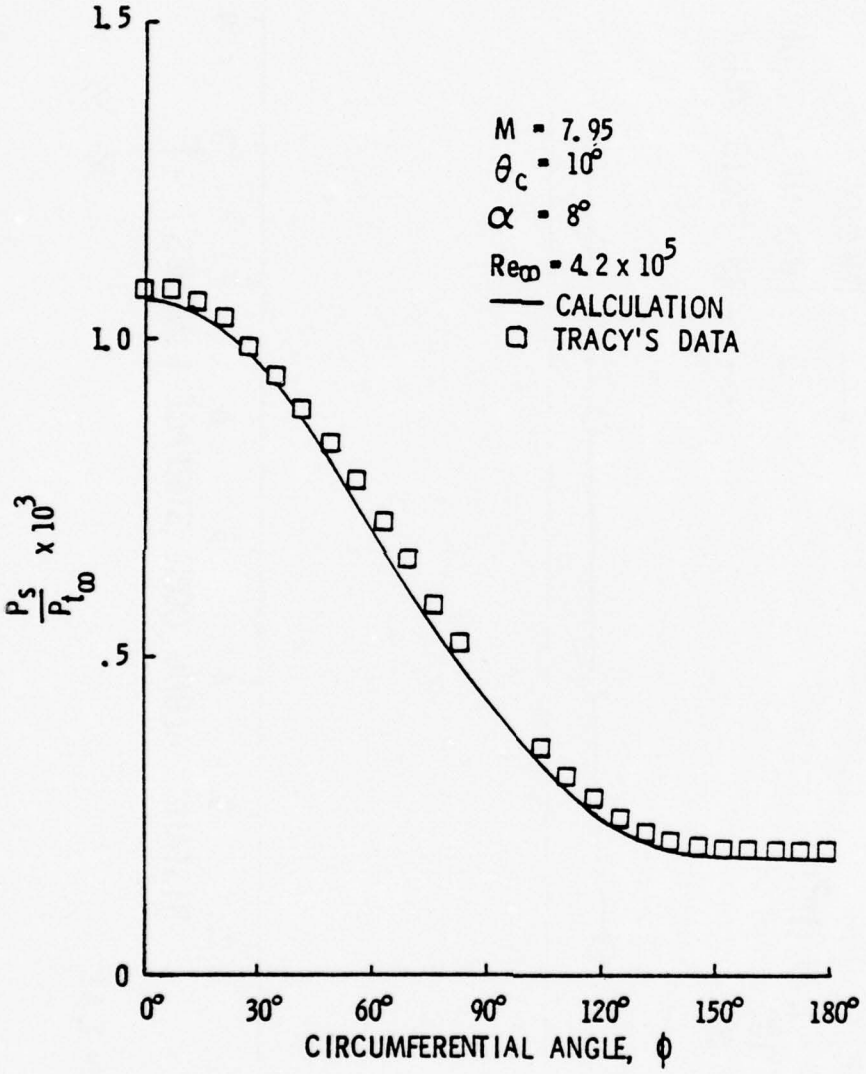


Figure 7. Comparison of Calculated and Experimental Surface Pressure at Tracy's Conditions, α = 8°

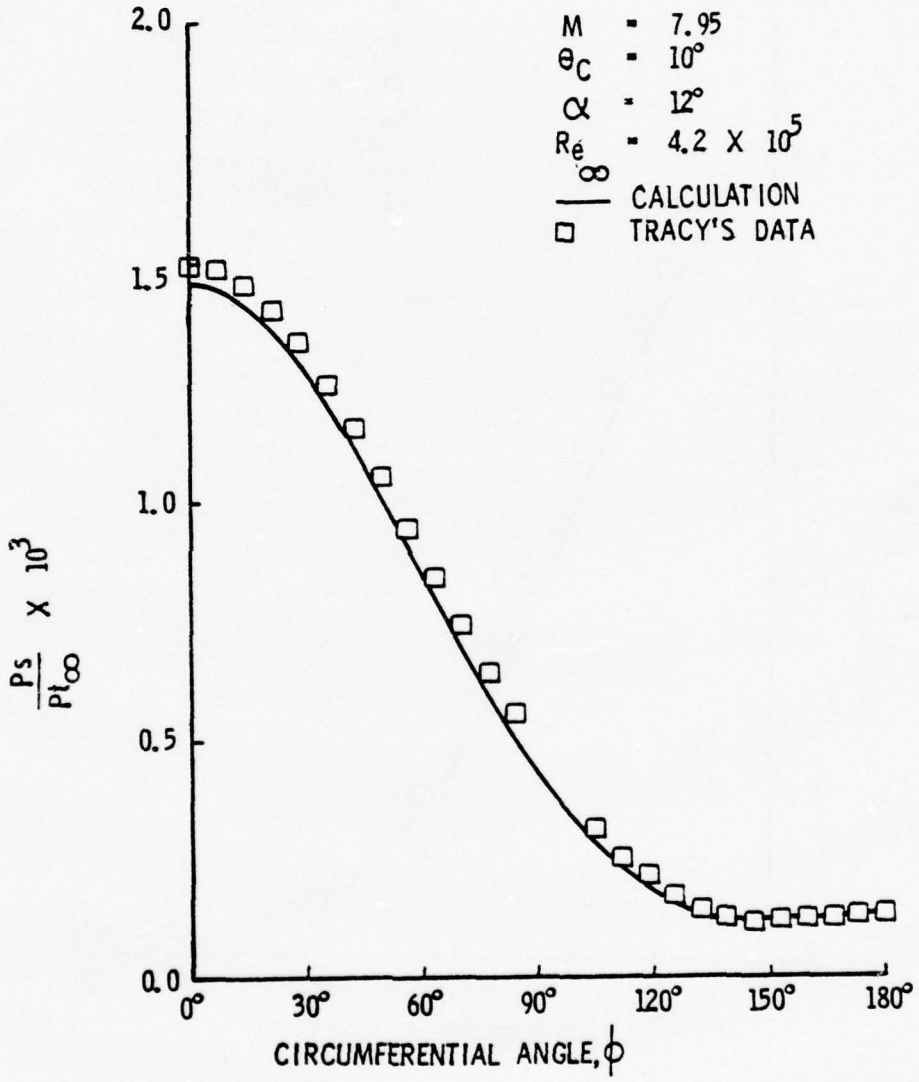


Figure 8. Comparison of Calculated and Experimental Surface Pressure at Tracy's Conditions, α = 12°

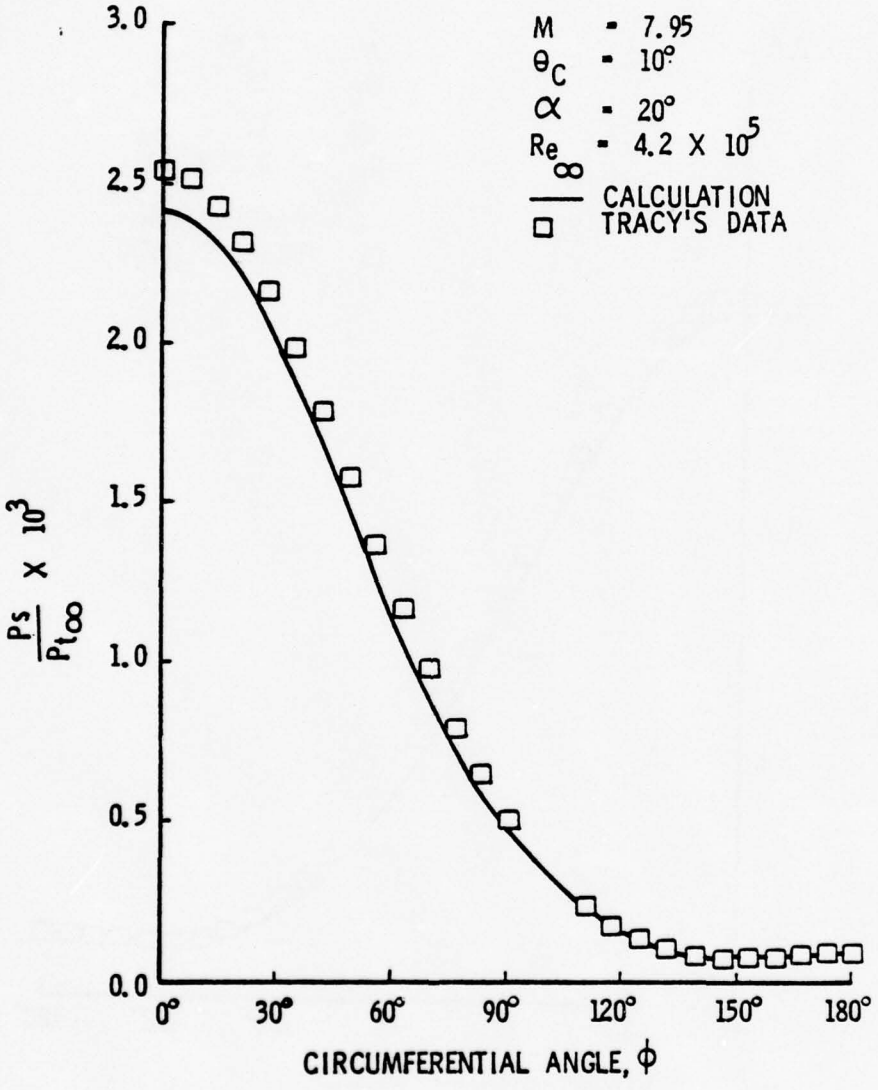


Figure 9. Comparison of Calculated and Experimental Surface Pressure at Tracy's Conditions, α = 20°

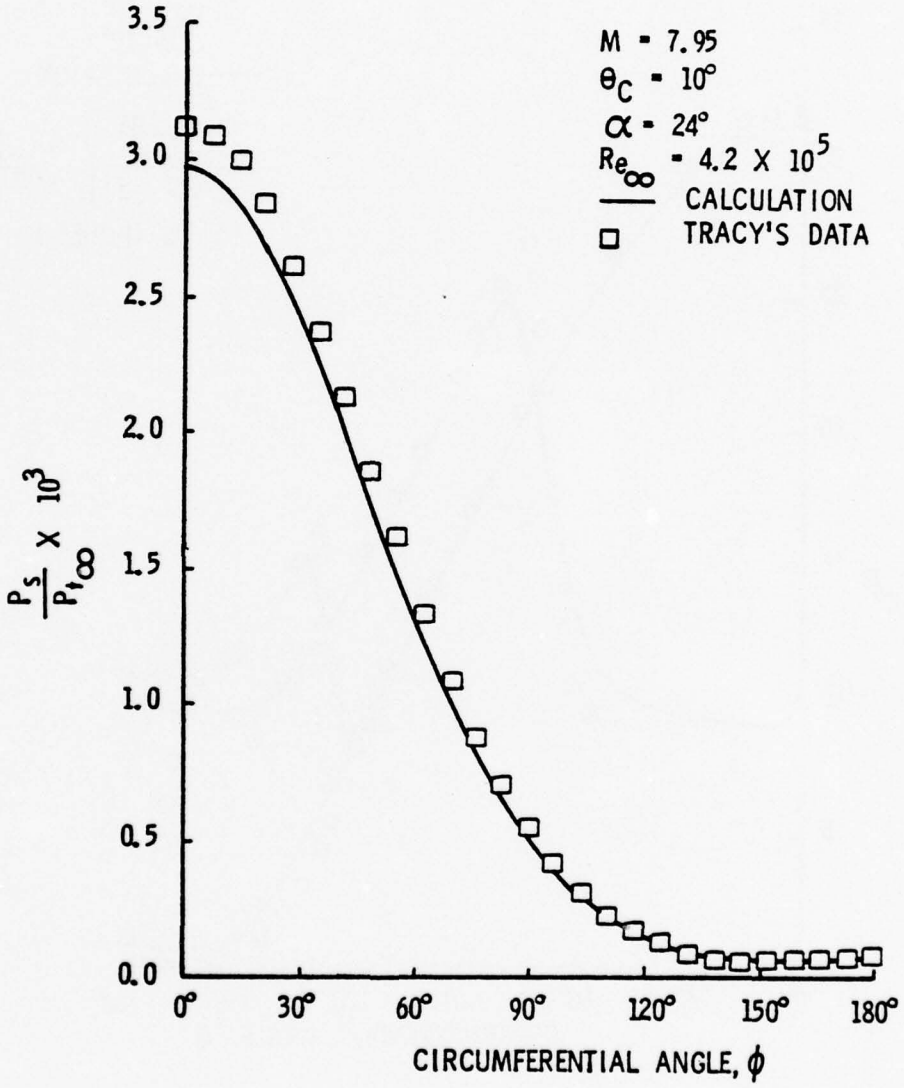


Figure 10. Comparison of Calculated and Experimental Surface Pressure at Tracy's Conditions, α = 24°

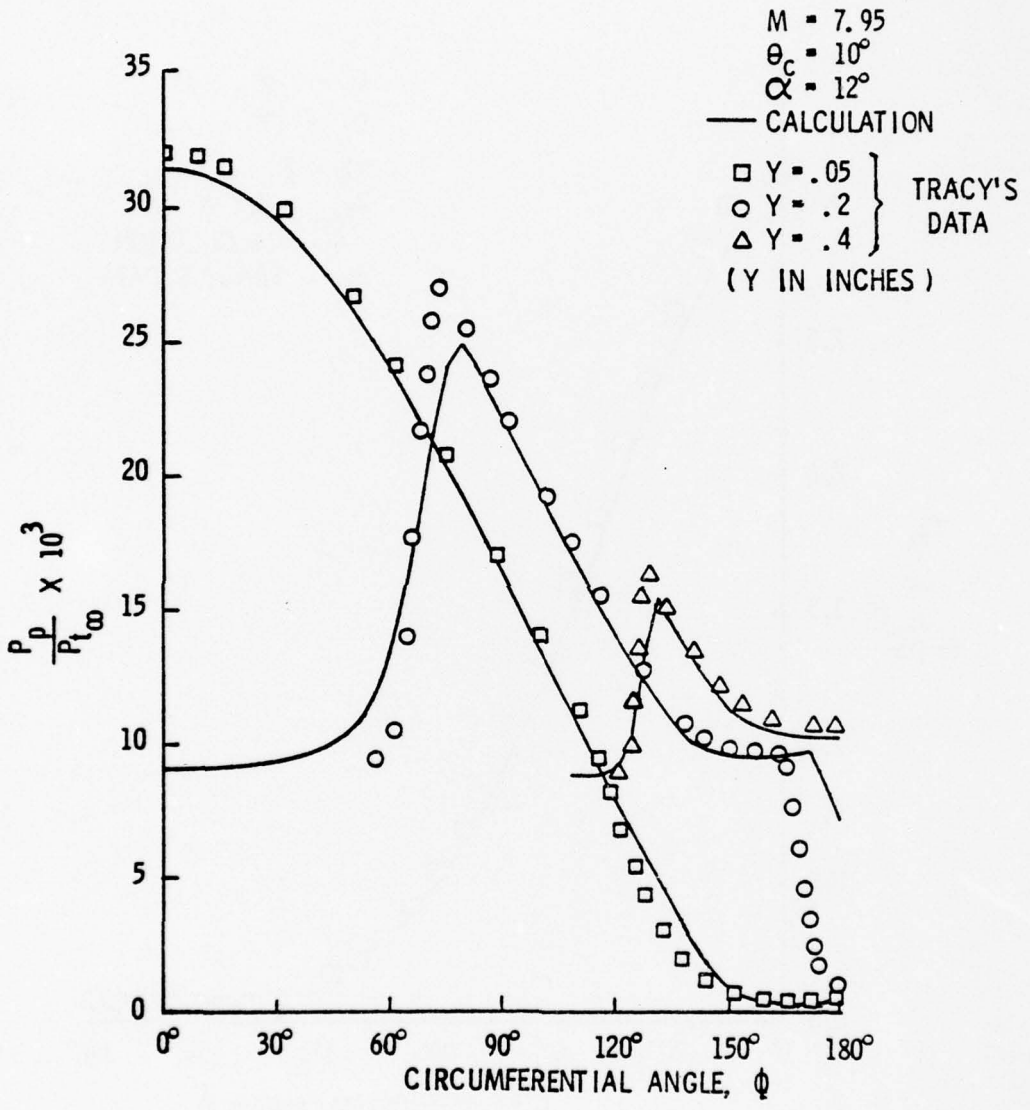


Figure 11. Comparison of Circumferential Pitot Pressure Surveys at Constant Height Above the Cone Surface at Tracy's Conditions, α = 12°

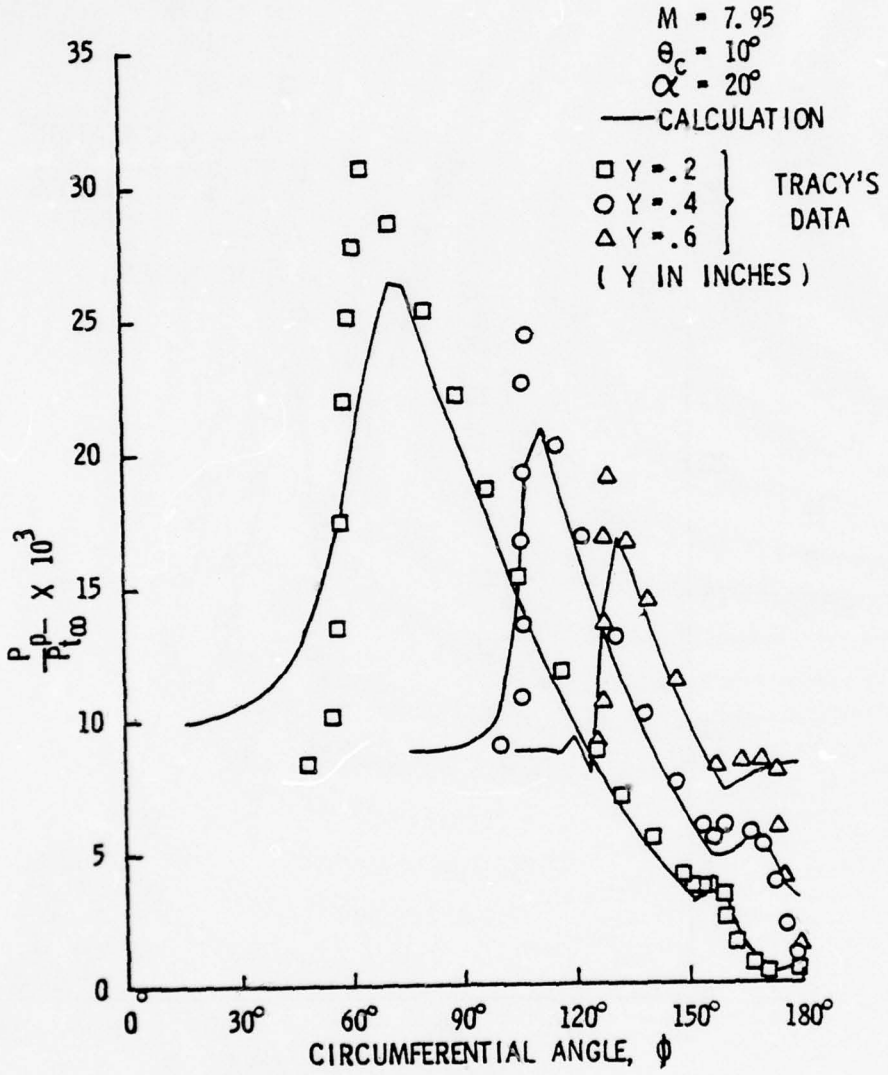


Figure 12. Comparison of Circumferential Pitot Pressure Surveys at Constant Height Above the Cone Surface at Tracy's Conditions, $\alpha = 20°$

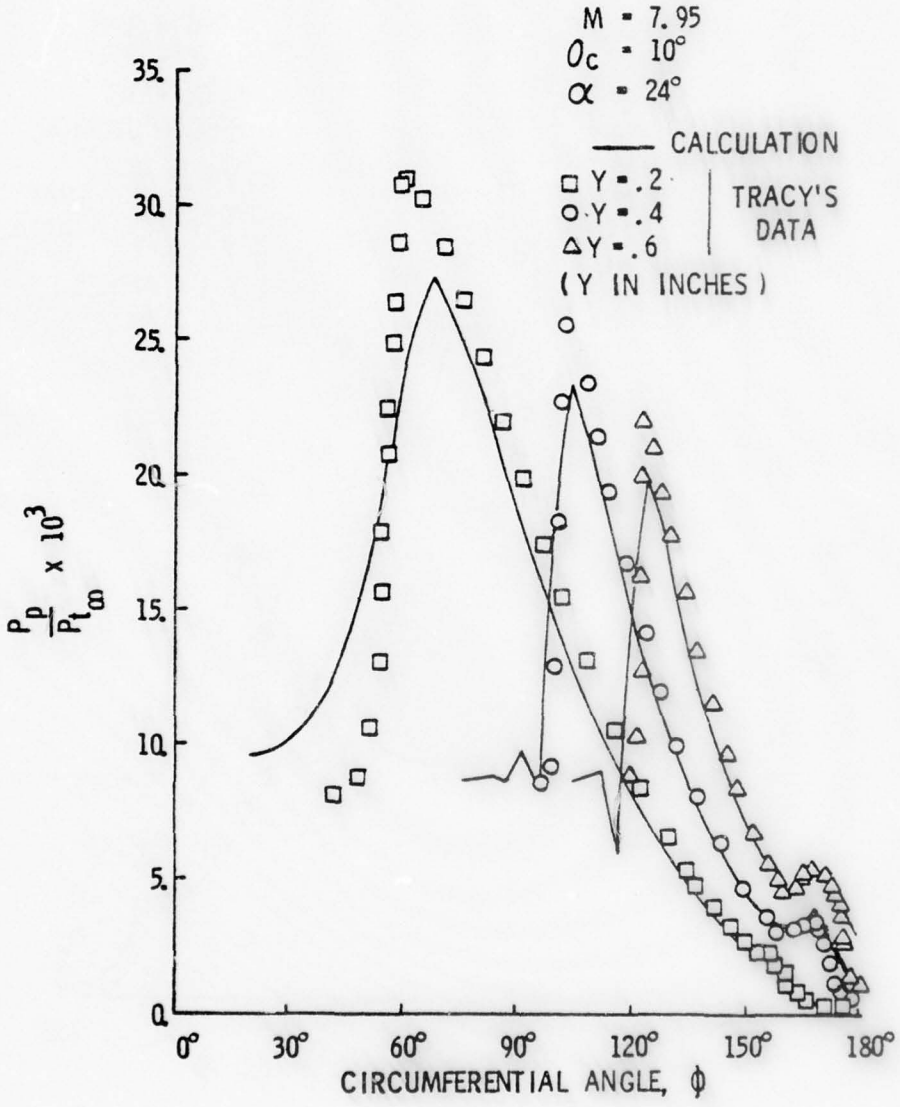


Figure 13. Comparison of Circumferential Pitot Pressure Surveys at Constant Height Above the Cone Surface at Tracy's Conditions, $\alpha = 24°$

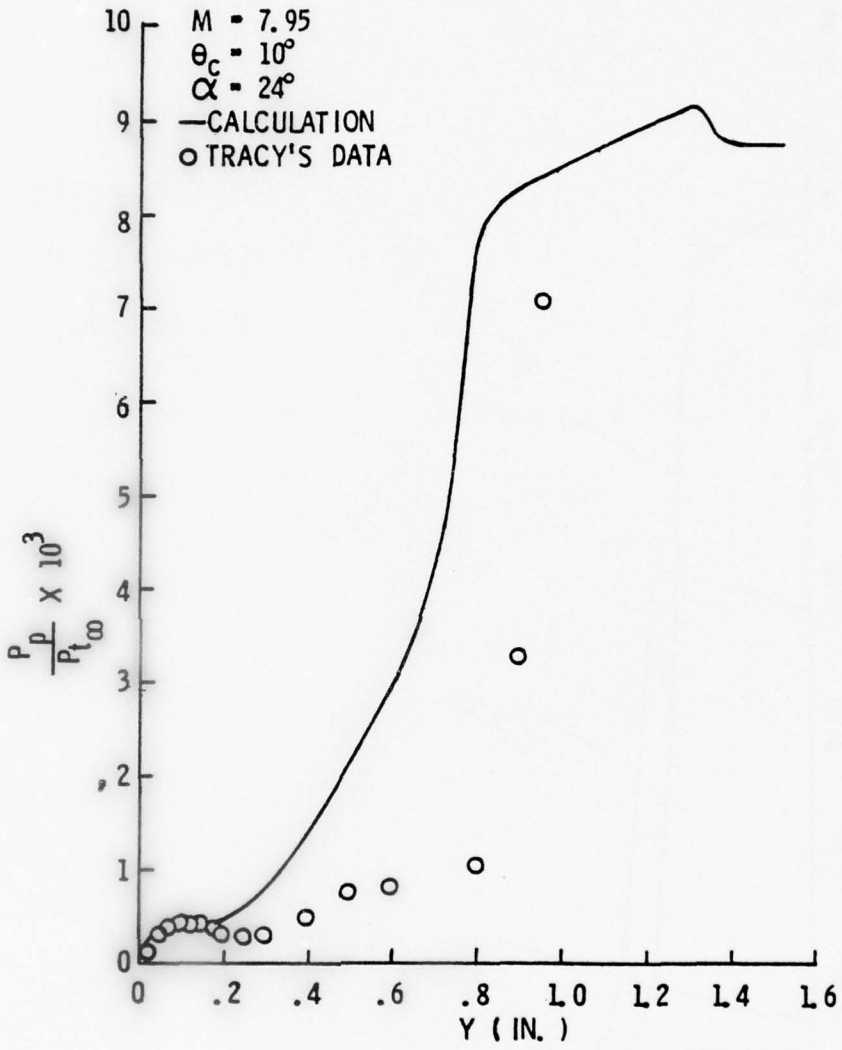


Figure 14. Comparison of Pitot Pressure Survey Along Lee Centerline (ϕ = 180°) at Tracy's Conditions, α = 24°

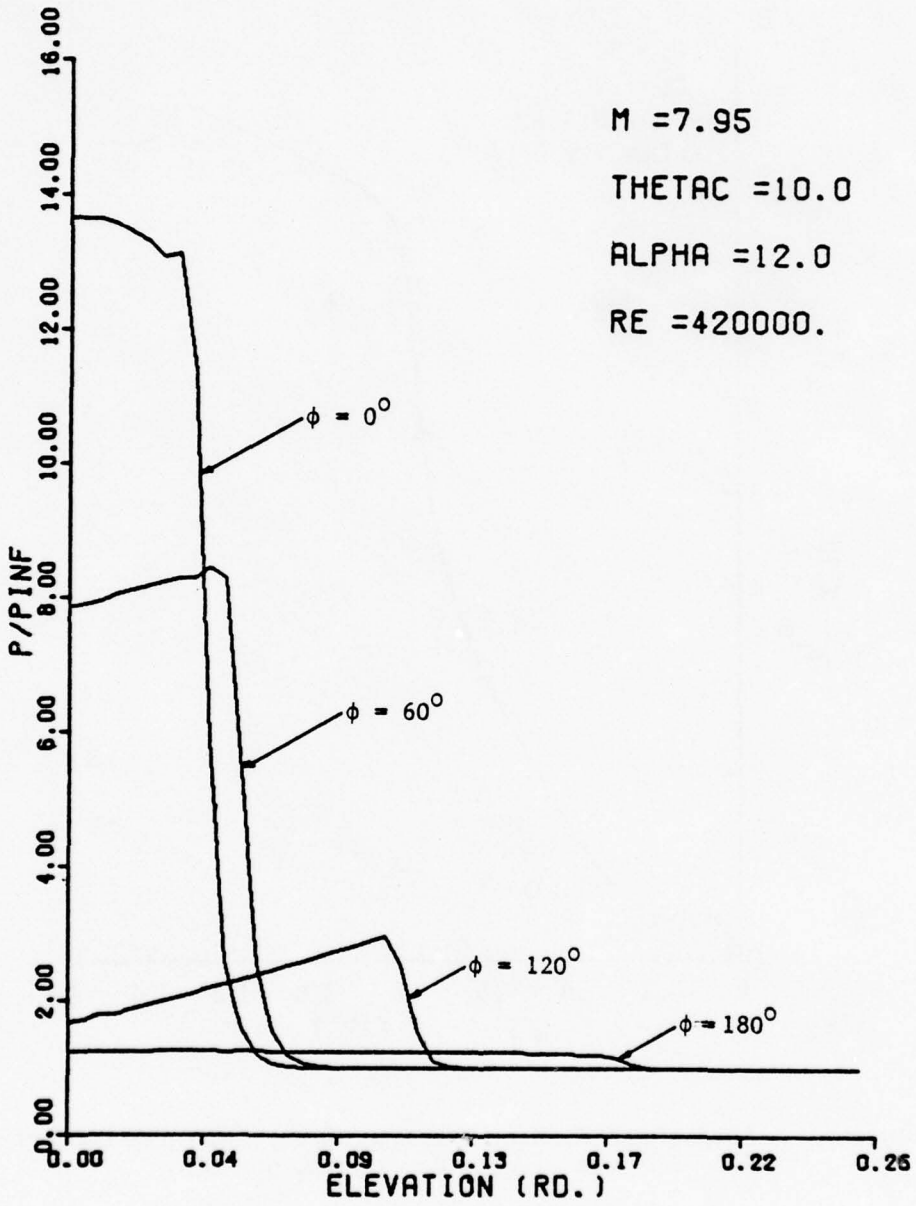


Figure 15. Calculated Static Pressure Along θ at 60° Circumferential Intervals at Tracy's Conditions, α = 12°

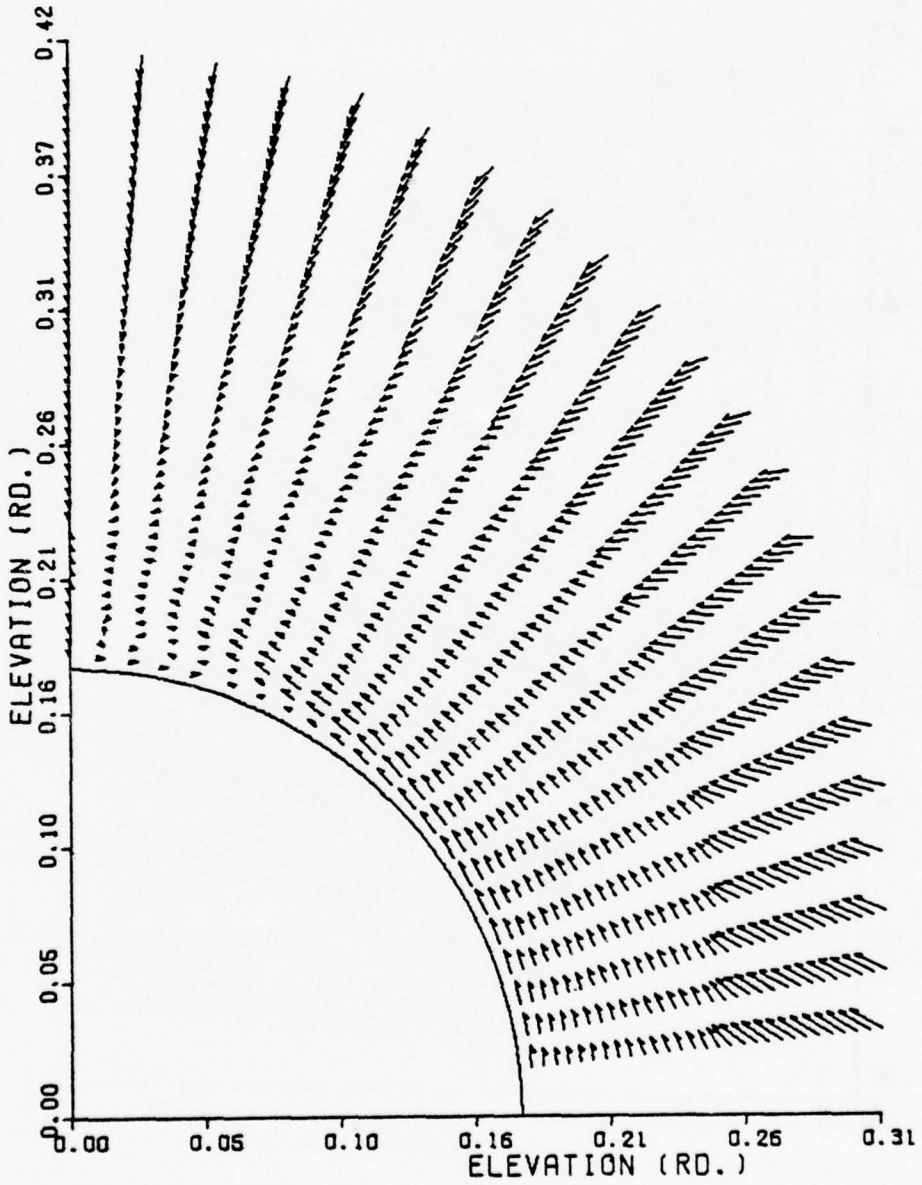


Figure 16. Cross-Flow Velocity Vectors Plotted as Seen on Spherical Surface at Tracy's Conditions, $\alpha = 12^{\circ}$

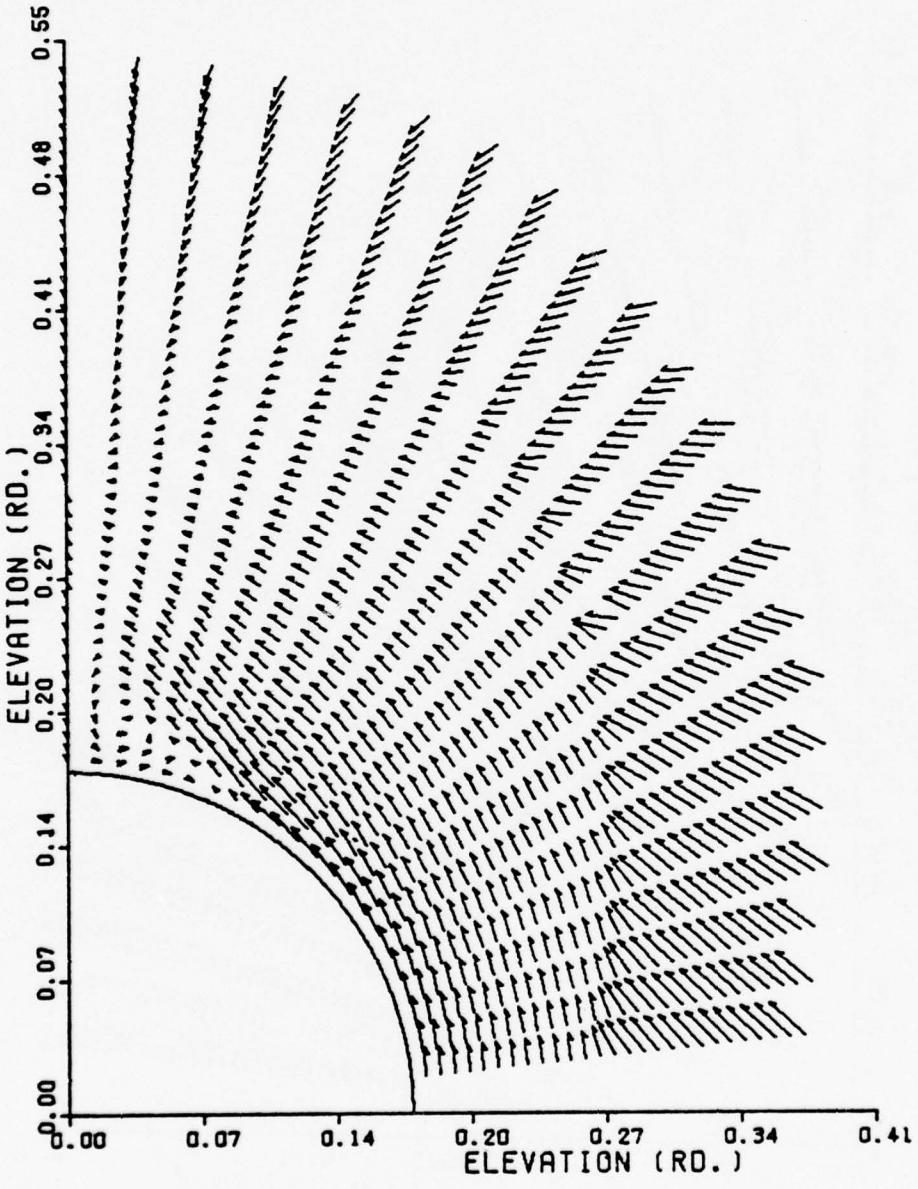


Figure 17. Cross-Flow Velocity Vectors Plotted as Seen on Spherical Surface at Tracy's Conditions, $\alpha = 20°$

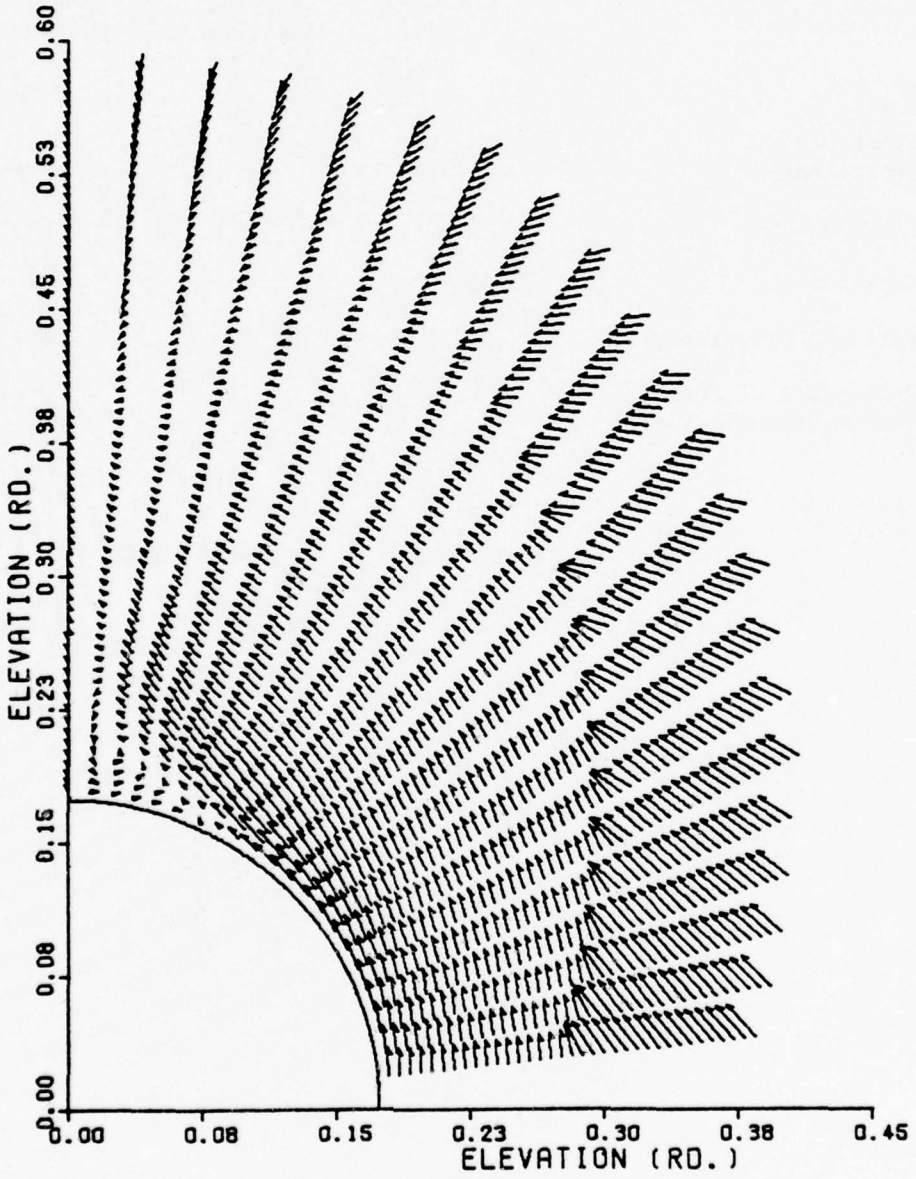


Figure 18. Cross-Flow Velocity Vectors Plotted as Seen on Spherical Surface at Tracy's Conditions, $\alpha = 24°$

$M = 7.95$, $\theta_c = 10^\circ$

	Tracy	Lubard, Helliwell	Present Calculation
Re_x	3.6×10^5		4.2×10^5
Shock Waves, Sonic Lines	●	○	———
Viscous Layer	◆	◇	- - - - - -
Separation	▲		^
Vortical Singularity			◊
Projection of Free Stream Velocity Vector			⊕

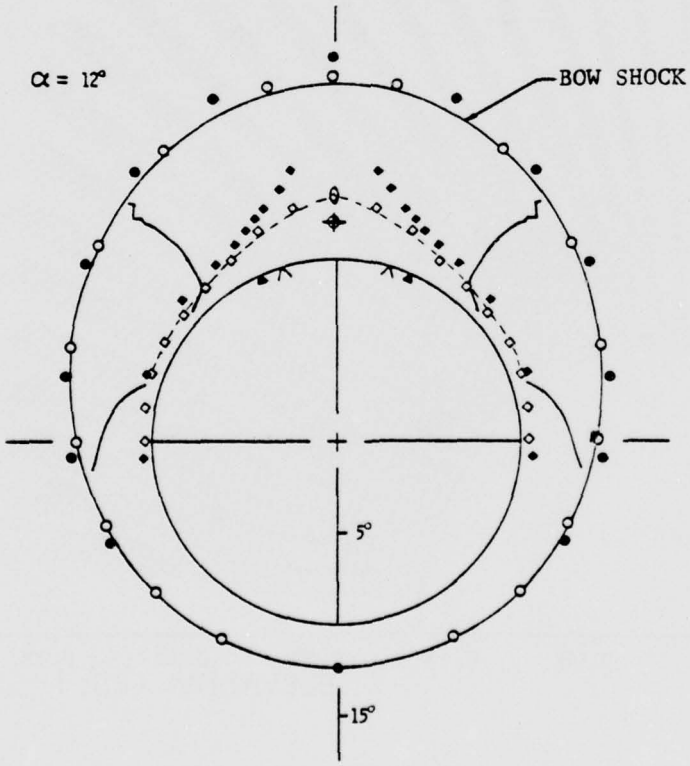


Figure 19. Comparison of Calculated and Experimental Flow Field Features at Tracy's Conditions, $\alpha = 12^\circ$

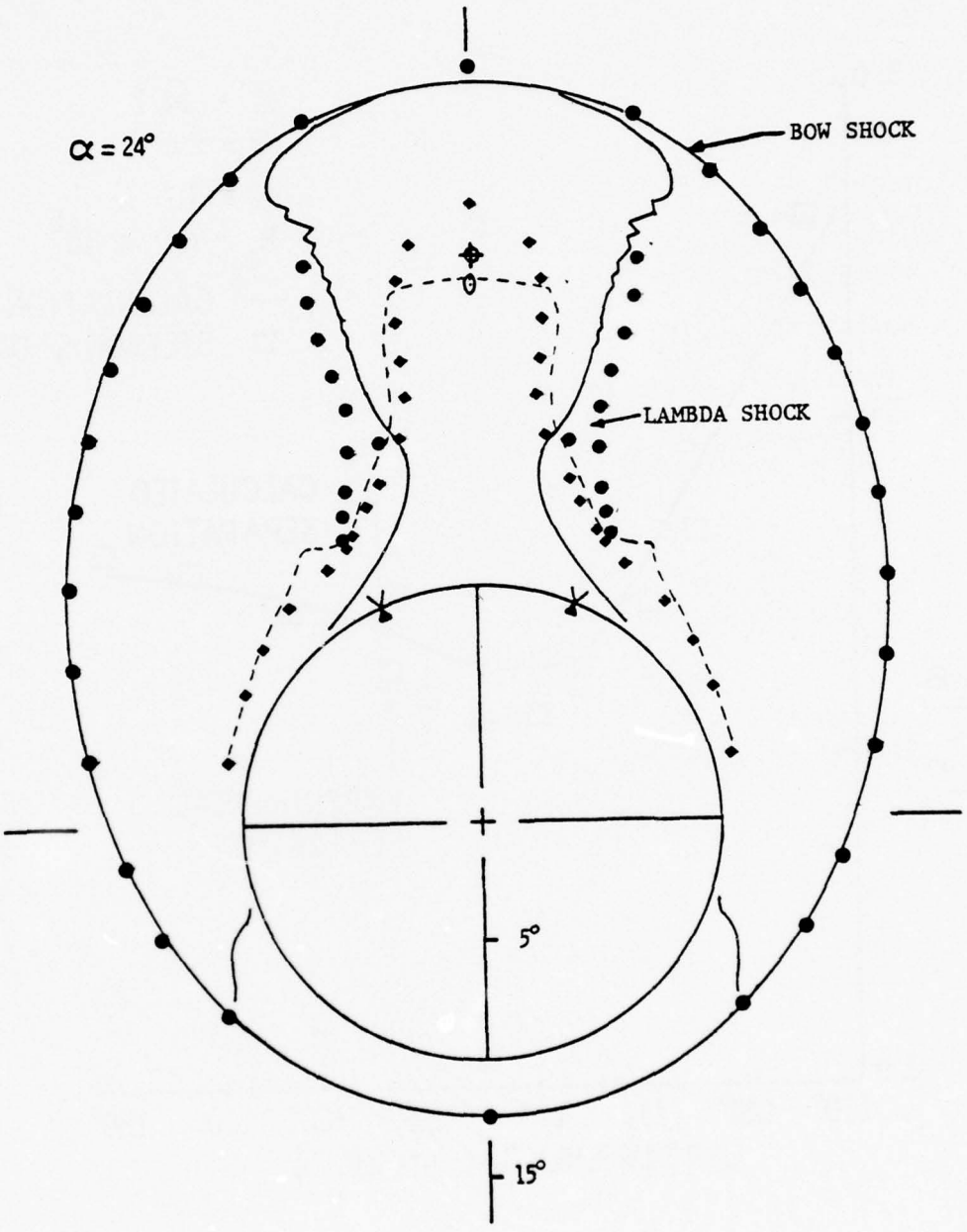


Figure 20. Comparison of Calculated and Experimental Flow Field Features at Tracy's Conditions, α = 24° (Legend Given in Figure 19)

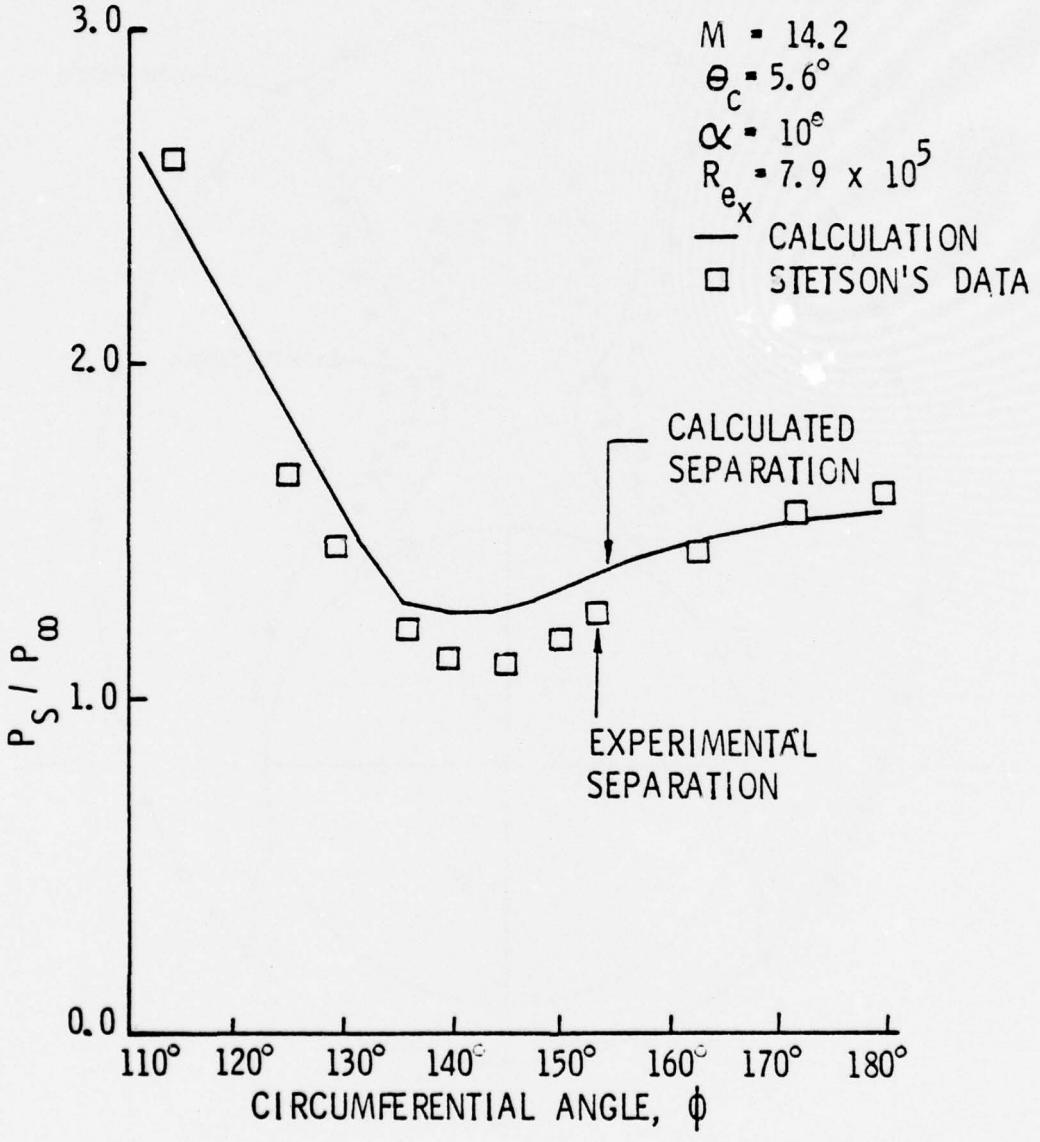


Figure 21. Comparison of Calculated and Experimental Surface Pressure at Stetson's Conditions

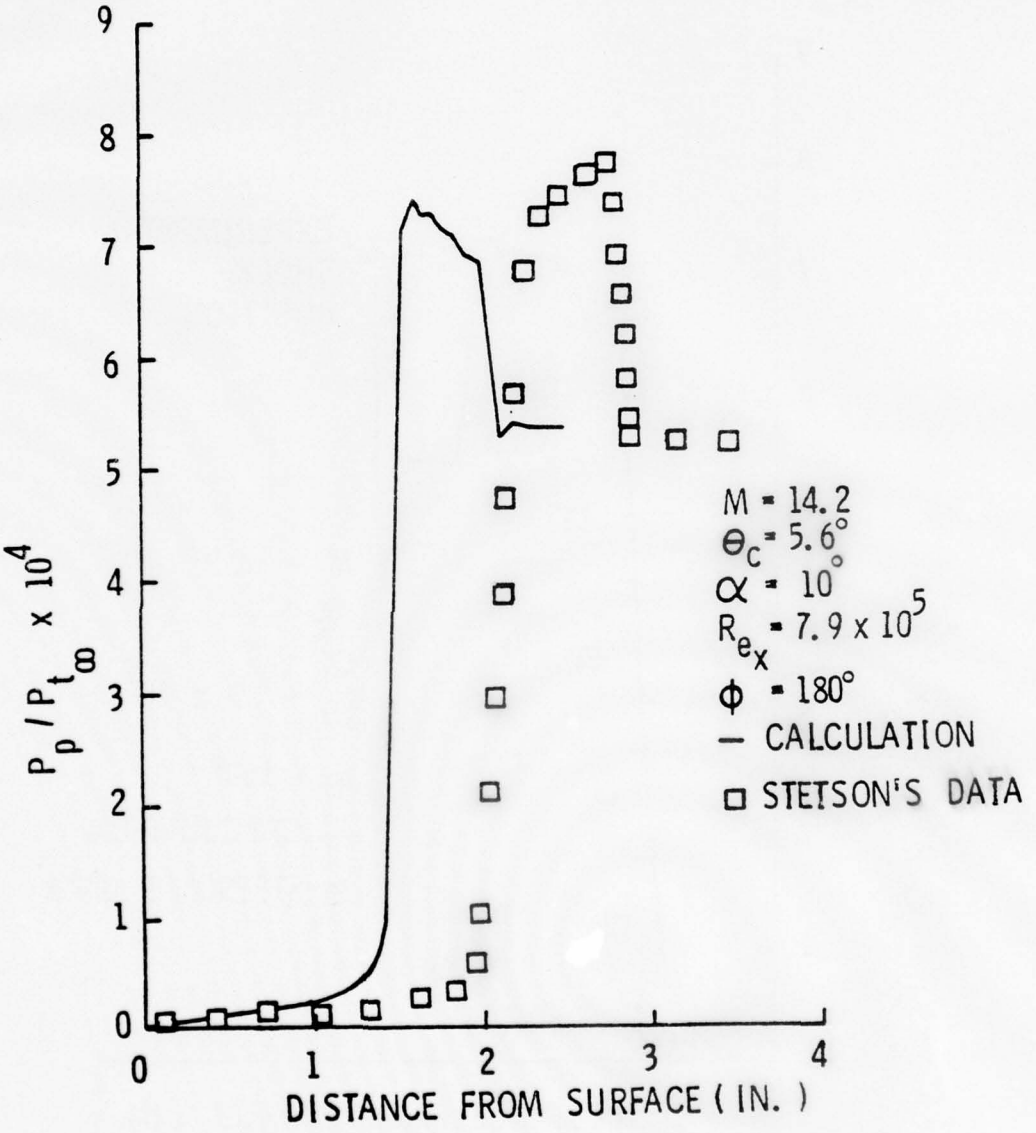


Figure 22. Comparison of Pitot Pressure Survey at Constant ϕ at Stetson's Conditions, $\phi = 180°$

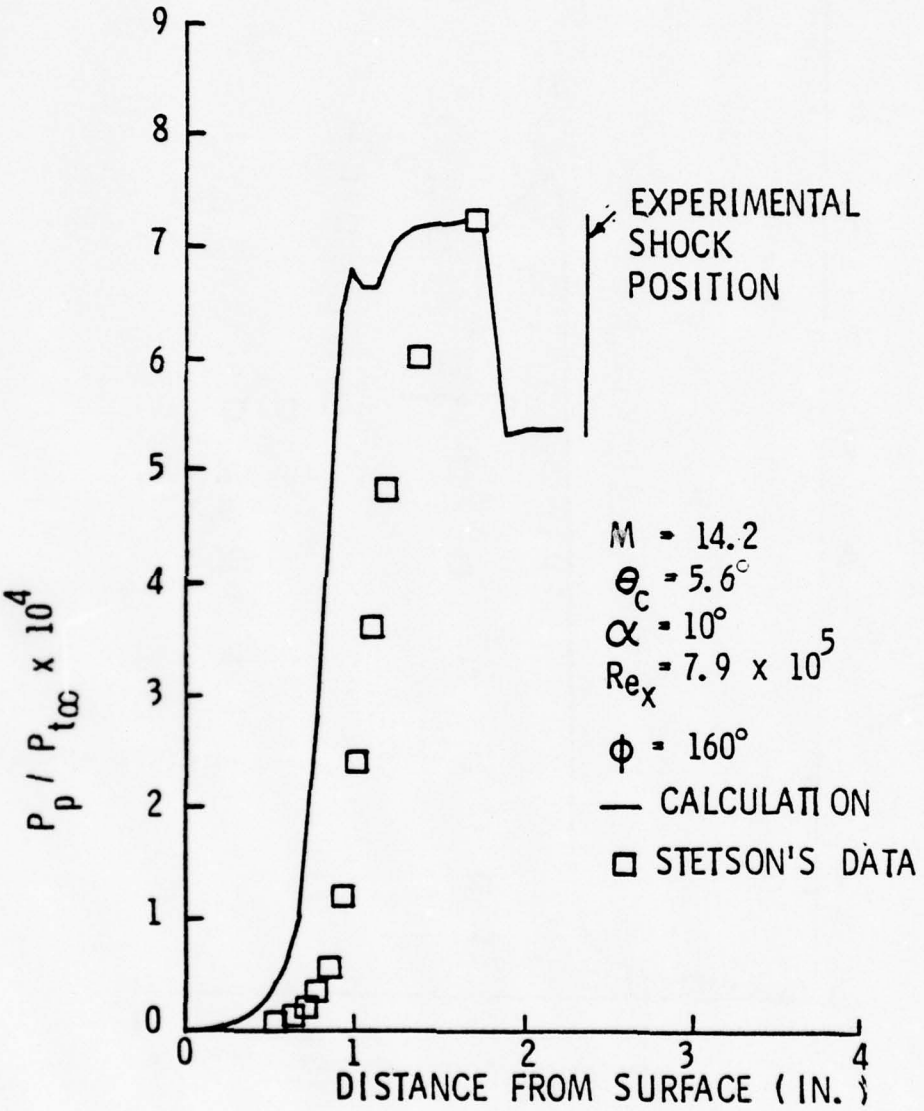


Figure 23. Comparison of Pitot Pressure Survey at Constant ϕ at Stetson's Conditions, $\phi = 160°$

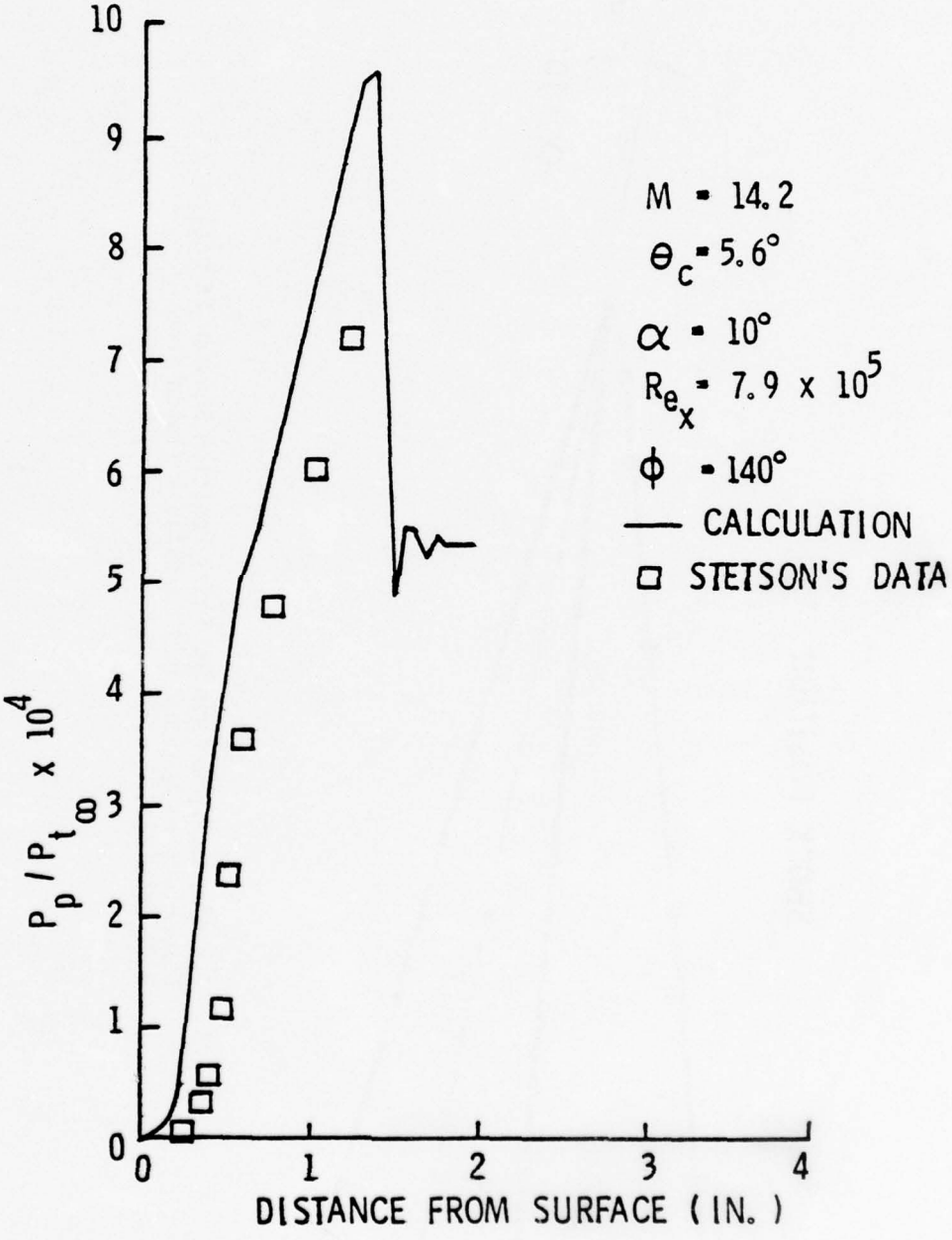


Figure 24. Comparison of Pitot Pressure Survey at Constant ϕ at Stetson's Conditions, ϕ = 140°

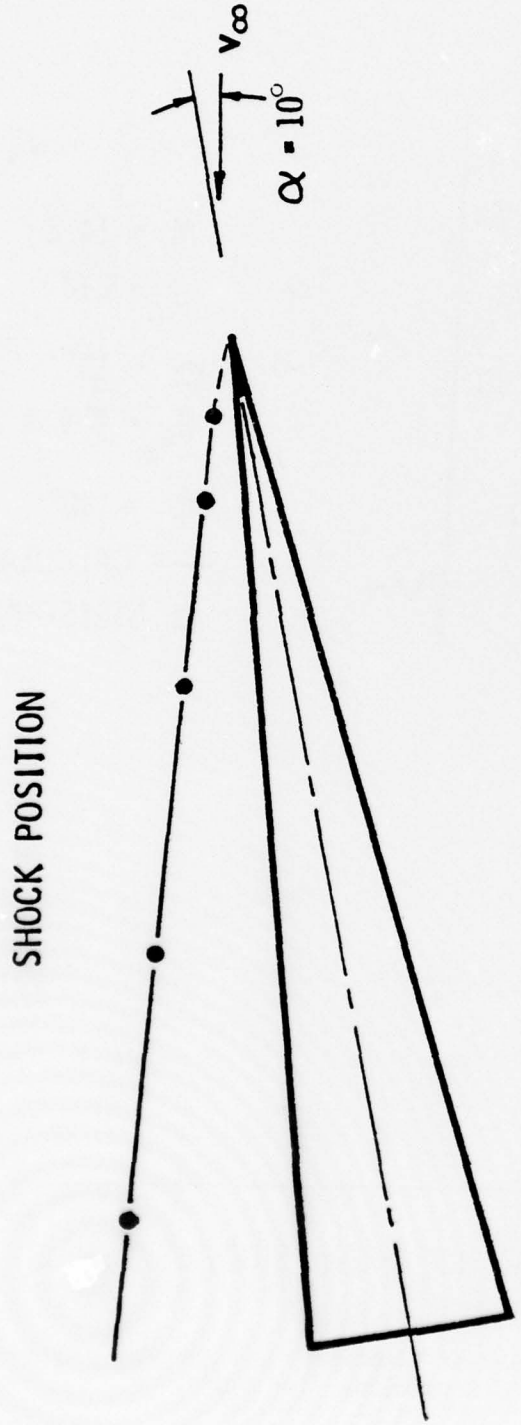


Figure 25. Experimentally Determined Shock Position Showing Effective Nose Blunting at Stetson's Conditions (Taken from Reference 22)

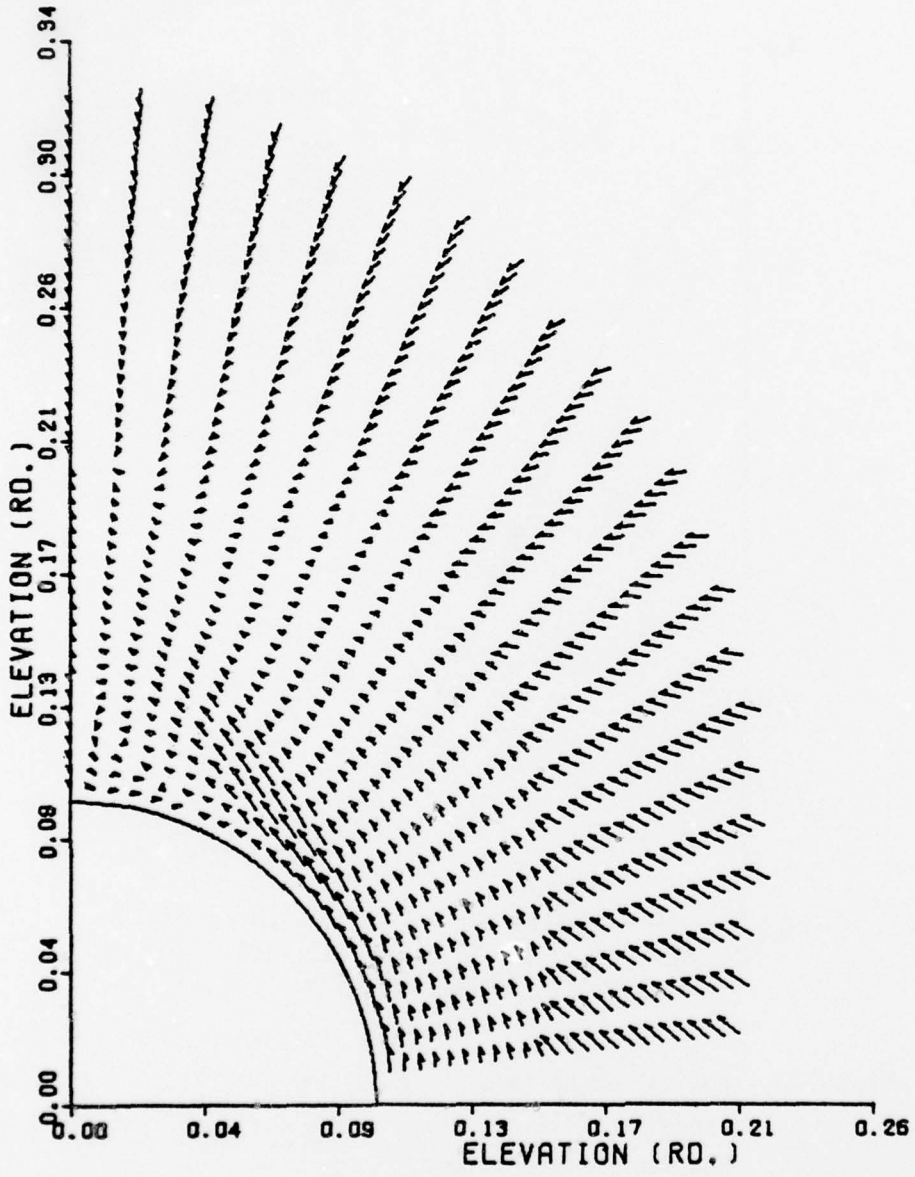


Figure 26. Cross-Flow Velocity Vectors Plotted as Seen on Spherical Surface at Stetson's Conditions

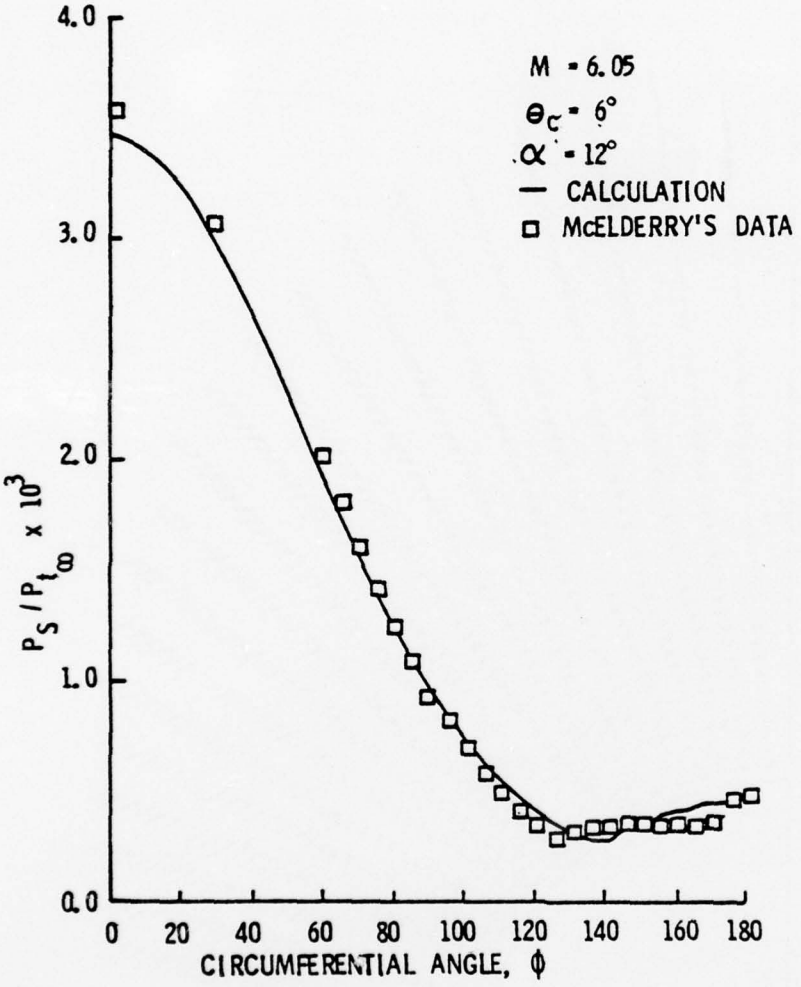


Figure 27. Conical Comparison of Calculated ($Re_x = 1.5 \times 10^6$) and Experimental ($Re_x = 15.0 \times 10^6$) Surface Pressure at McElderry's Conditions

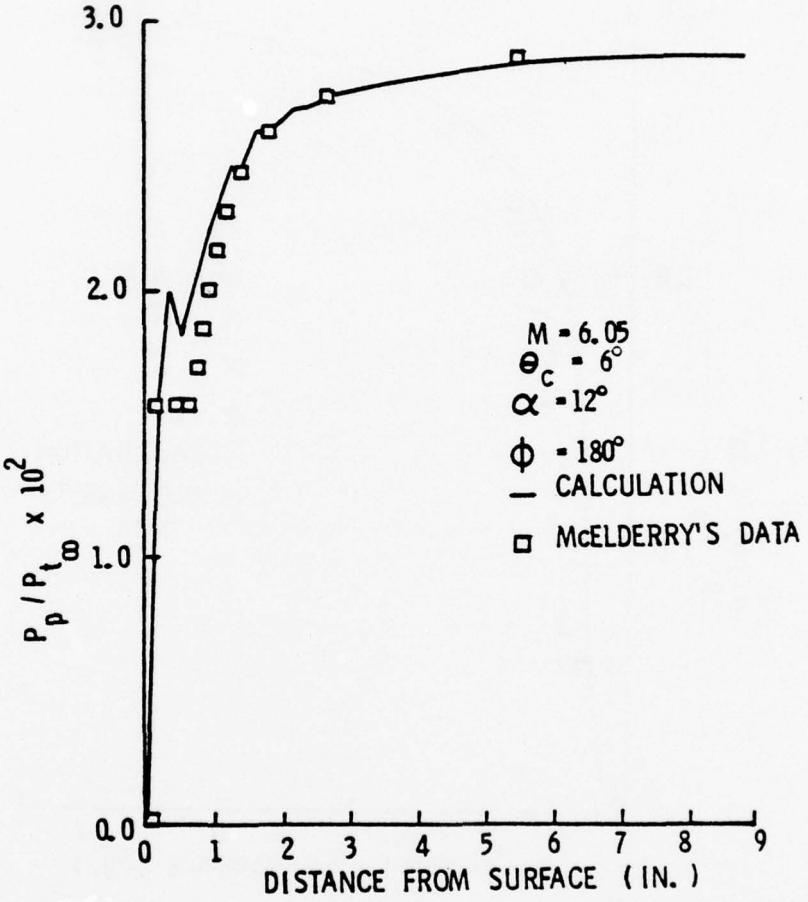


Figure 28. Conical Comparison of Calculated ($Re_x = 1.5 \times 10^6$) and Experimental ($Re_x = 15.0 \times 10^6$) Pitot Pressure Survey at Constant ϕ at McElderry's Conditions, $\phi = 180°$

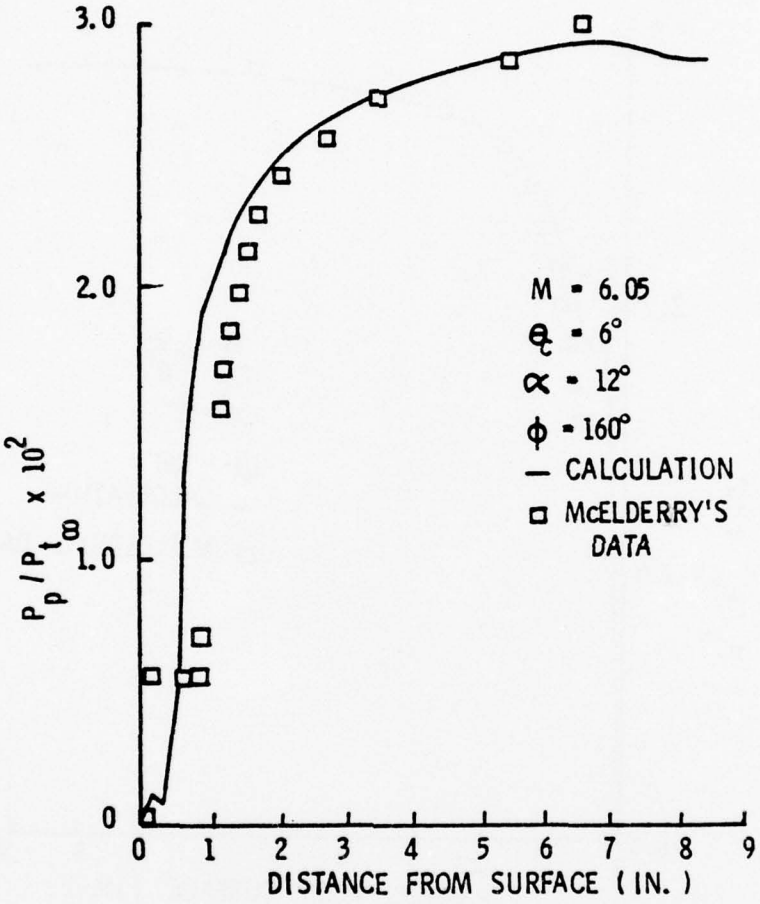


Figure 29. Conical Comparison of Calculated (Re_x = 1.5 x 10^6) and Experimental (Re_x = 15.0 x 10^6) Pitot Pressure Survey at Constant ϕ at McElderry's Conditions, ϕ = 160°

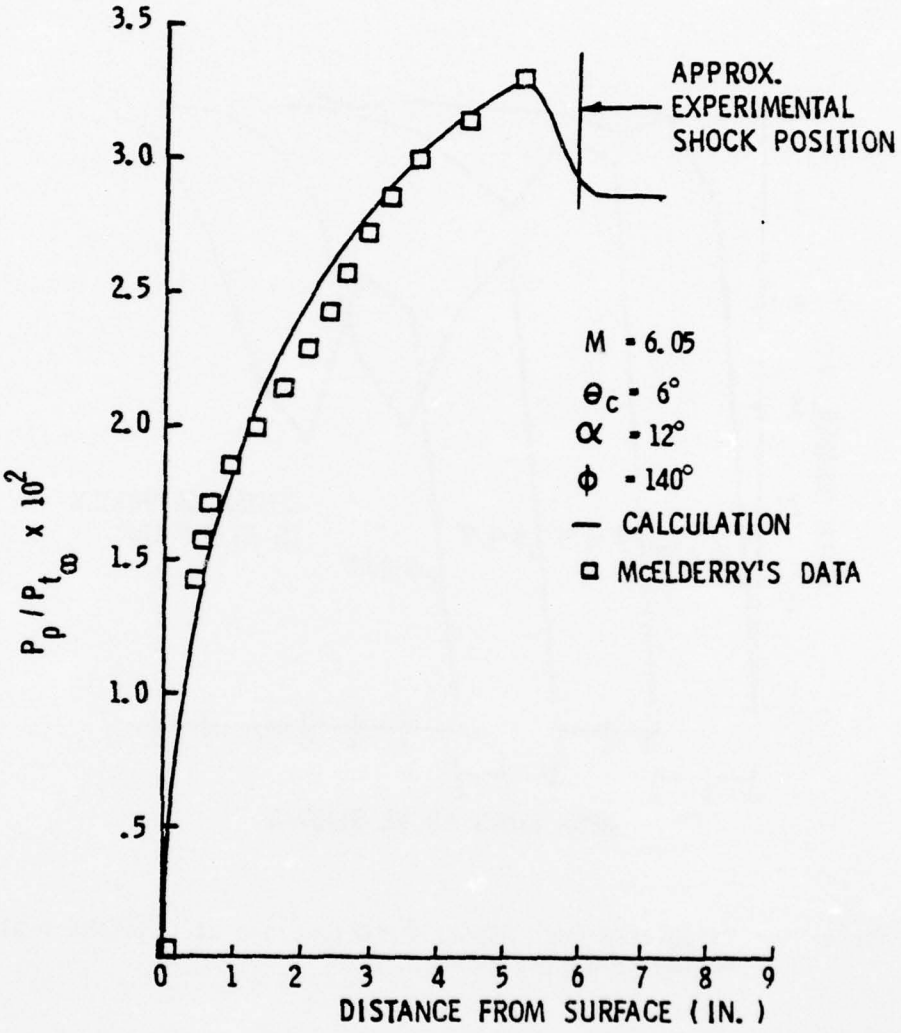


Figure 30. Conical Comparison of Calculated ($Re_x = 1.5 \times 10^6$) and Experimental ($Re_x = 15.0 \times 10^6$) Pitot Pressure Survey at Constant ϕ at McElderry's Conditions, $\phi = 140°$

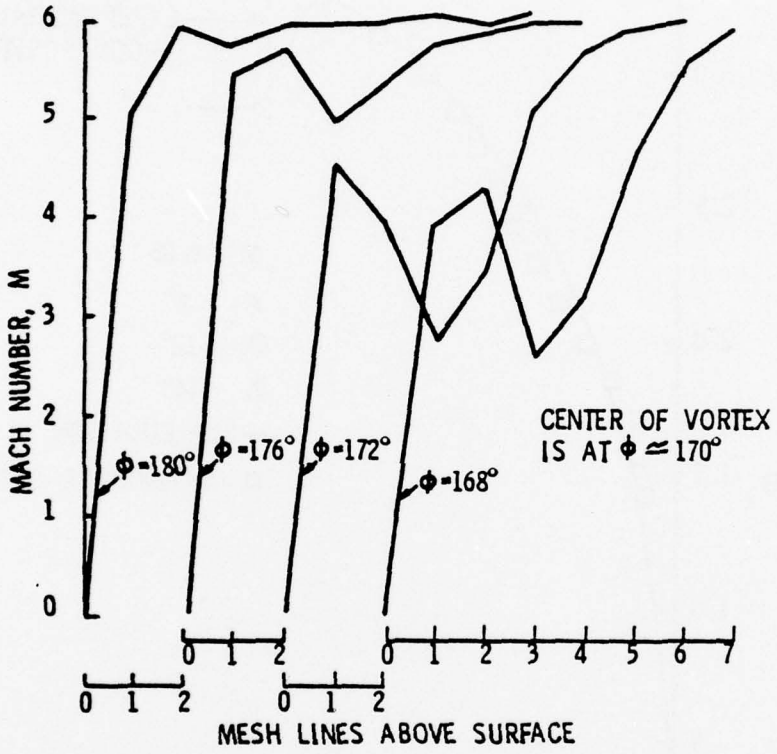


Figure 31. Calculated Mach Number Distributions at Constant ϕ at McElderry's Conditions

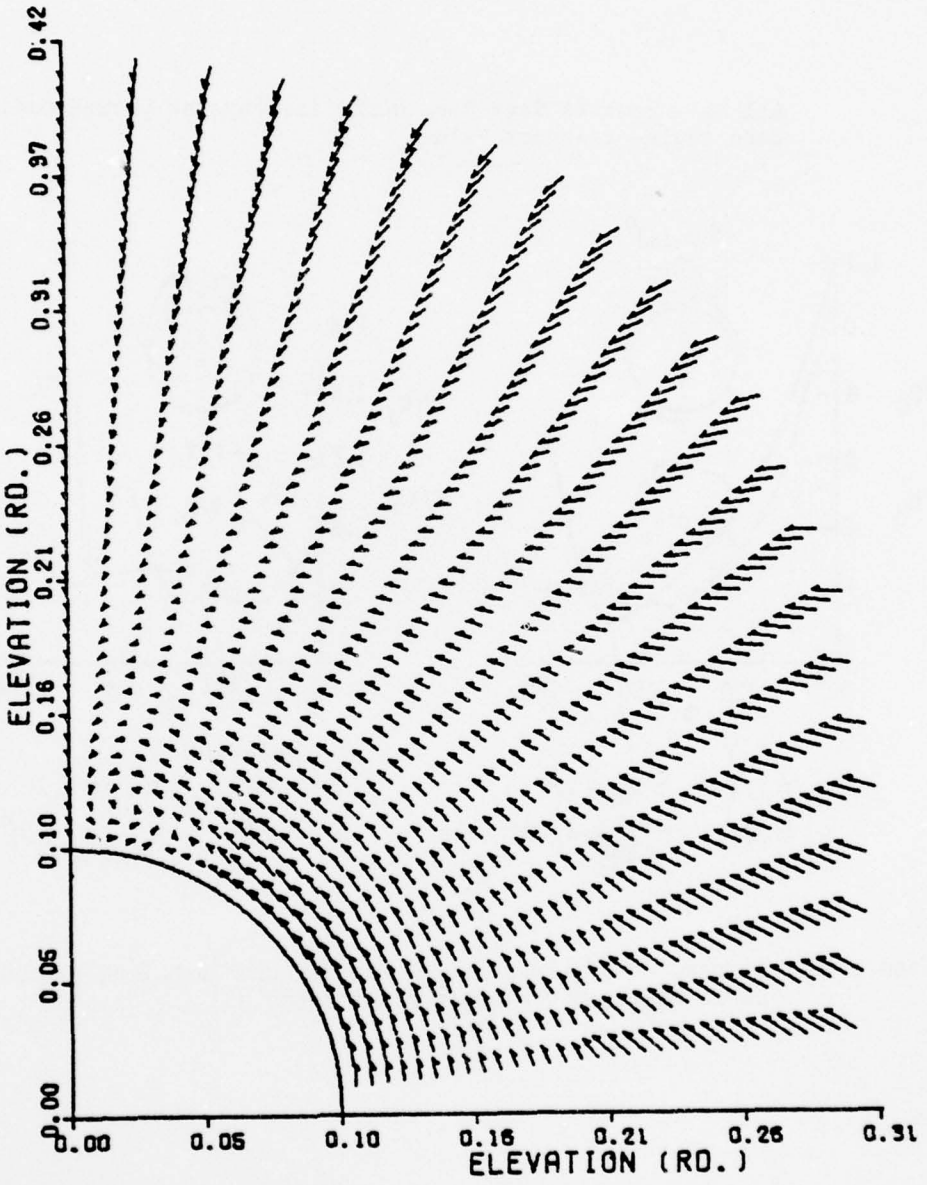


Figure 32. Cross-Flow Velocity Vectors Plotted as Seen on Spherical Surface at McElderry's Conditions

All Measurements Have Been Normalized by the Corresponding Zero Angle-of-Attack Value.

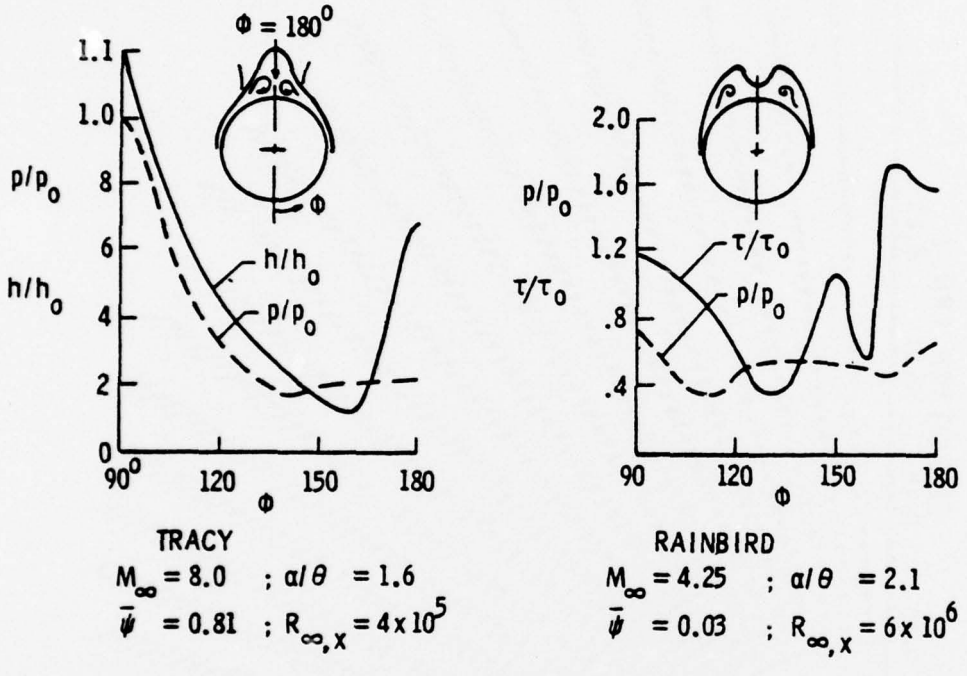


Figure 33. Comparison of Experimental Laminar and Turbulent Viscous Layer Features (Taken from Reference 33)

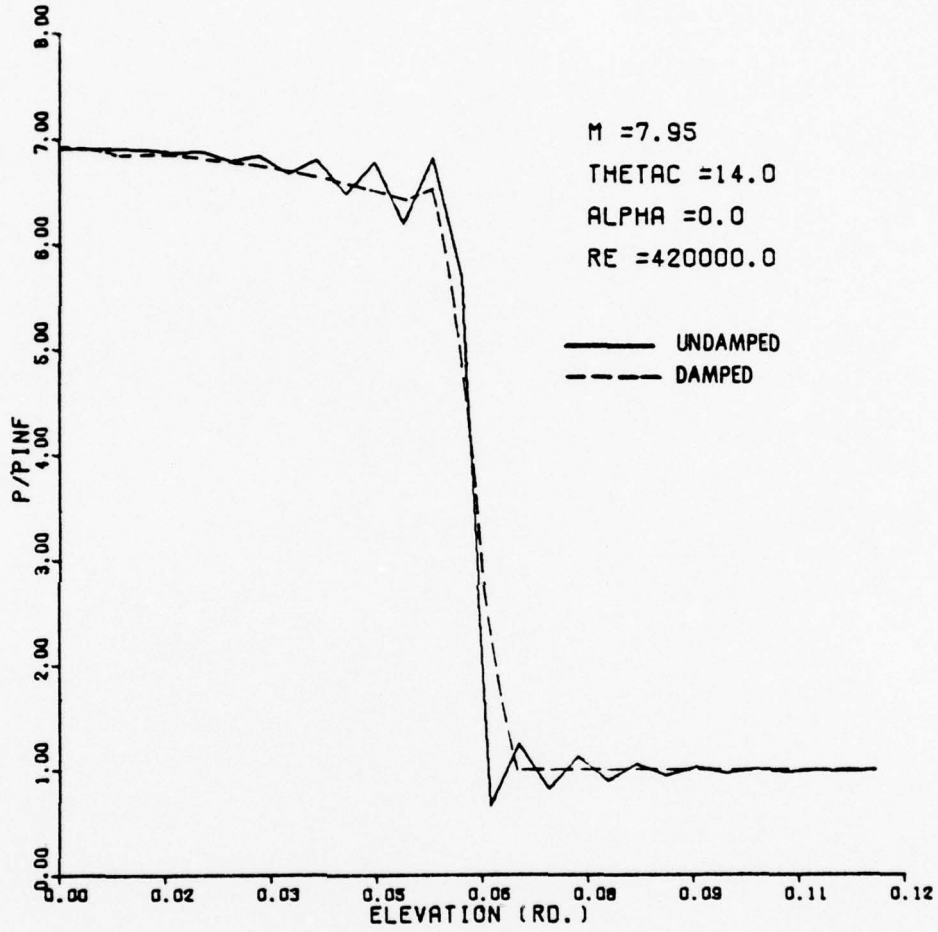


Figure 34. Demonstration of the Effect of Normal Stress Damping on Calculated Static Pressure Along θ, $\alpha = 0°$

APPENDIX A

BOUNDARY CONDITIONS

The solution of the Navier-Stokes equations by numerical methods is in reality a boundary value problem subject to the same requirements and constraints as the solution of the set by analytic techniques. However, the mathematical theory concerning existence and uniqueness of solutions for this equation set has not been resolved (Reference 35). This statement is especially true for compressible flows. The only course then open to the engineer is to presume a well posed problem exists when the known physically derived auxiliary conditions are imposed. If the integration of the equation set subject to these conditions yields a steady state solution (which of course is not guaranteed), then experimental results for these same conditions must be used to verify that the solution obtained is indeed the correct one. When this is done for several related sets of conditions with good results, confidence in the adequacy of the solution technique for use where experimental results are not available is increased. However, the user of the technique for this purpose must always take care to examine the solutions obtained for nonphysical features, as it is never possible to completely define initially the limits of usefulness of an equation set in any meaningful sense. The above procedure was followed in this study. The rest of this appendix will present the auxiliary conditions used and the manner in which they were imposed.

Examination of Figure 2 reveals that the finite difference mesh is a spherical surface with the inner edge bounded by the cone and the outer edge free. The mesh shown is 360° circumferentially in extent. Since two known lines of symmetry exist at $\phi = 0°$ and $\phi = 180°$, the extent of the surface can be readily reduced by one-half. This reduction can be made without increase in the number of boundary values necessary to the calculation by specifying an additional line of mesh points in the θ direction and at the required value of ϕ. The results of each sweep during the integration are then reflected symmetrically to these lines about the lines of symmetry. This causes the integration (at the line of symmetry) to perceive that a mirror image of the solution is evolving on the other 180° of the mesh (as it would

PRECEDING PAGE BLANK-NOT FILMED

be if the sweep were actually 360°). This procedure therefore requires no a priori knowledge of the flow quantities at the lines of symmetry and implies that the following conditions are being imposed at these lines of symmetry:

at $\phi = 0°$ and $\phi = 180°$

$$\frac{\partial u}{\partial \phi} = 0 \qquad \frac{\partial p}{\partial \phi} = 0$$

$$\frac{\partial v}{\partial \phi} = 0 \qquad \frac{\partial \rho}{\partial \phi} = 0$$

$$w = 0 \qquad \frac{\partial T}{\partial \phi} = 0$$

Note that these two conditions are imposed only at one line of symmetry. They are then derivable from the governing equations at the other.

Two boundaries therefore remain which must be dealt with.

Examination of the six equations (the Navier-Stokes equations, the continuity and energy equations, plus the equation of state) as modified reveals that all three velocity components and temperature appear as second derivatives in θ and ϕ with pressure and density appearing as first derivatives in θ and ϕ. A solution should then be obtainable through the specification of two boundary conditions for each of the velocity components and temperature and one each for pressure and density. (In reality, the algebraic equation of state eliminates the requirement for specifying both pressure and density.) This was done in the present study in the following manner:

at the cone surface $\theta = \theta_c$, $\phi = 0° \rightarrow 180°$

$$u = v = w = 0$$

$$T = T_w (\phi)$$

at the outer boundary (physically, the free stream)

$\theta = \theta$ outer, $\phi = 0° \rightarrow 180°$

$$u = u_\infty (\phi) \qquad p = p_\infty$$

$$v = v_\infty (\phi) \qquad \rho = \rho_\infty$$

$$w = w_\infty (\phi) \qquad T = T_\infty$$

a uniform free stream is assumed

Note that although the quantities are specified along a line of constant θ, the ϕ distribution is completely specified also. It should also be noted that the total internal energy was used in place of the temperature as a dependent variable. The connection is simply $e = C_v T + \frac{V^2}{2}$. These conditions are now sufficient to allow solution of the problem.

Since pressure and density at the cone surface remain free (and indeed must do so to prevent overspecification of the boundary conditions), they must be determined during the integration process. This was done in the present study by analytically evaluating the θ momentum equation at the cone surface conditions. The resulting equation is non-dimensionalized form solved for $\frac{\partial p}{\partial \theta}$ is:

$$\frac{\partial p}{\partial \theta} = \frac{1}{k \sin\theta} \left\{ \frac{4}{3} \left[\frac{\cos\theta}{Re} + \sin\theta \frac{\partial}{\partial \theta} \left(\frac{1}{Re}\right) \right] \frac{\partial v}{\partial \theta} + \frac{8}{3} \frac{\sin\theta}{Re} \frac{\partial u}{\partial \theta} + \frac{4}{3} \frac{\sin\theta}{Re} \frac{\partial^2 v}{\partial \theta^2} - \frac{2}{3} \frac{\partial}{\partial \theta} \left(\frac{1}{Re} \frac{\partial w}{\partial \phi}\right) + \frac{\partial}{\partial \phi} \left(\frac{1}{Re} \frac{\partial}{\partial \theta}\right) \right\}$$

This equation is approximated by one sided second-order accurate finite differences about the surface mesh point of interest. The resulting difference equation is solved for the surface pressure, the only quantity in the equation which has not been updated when the equation is applied after a sweep through the mesh of either the predictor or the corrector. This equation can be represented by:

$$p^i_{j,\eta} = \frac{-2\Delta\theta}{3k \sin\theta} f(u,v,w) + \frac{4}{3} p^i_{j+1,\eta} - \frac{1}{3} p^i_{j+2,\eta}$$

with $j = 1$, and i and η indicating time level and ϕ position in the mesh respectively. The density at the surface is found via the equation of state and all flow quantities are then known or have been determined at the cone surface.

To complete the specification of the auxiliary conditions, initial values of the flow quantities are required at all points in the mesh in

order to begin the calculation. In the present study, this was done by setting the mesh to free stream conditions including the mesh point above the cone surface with true surface boundary conditions plus free stream pressure and density imposed at the cone surface. The calculation was then begun which resulted in a so called "impulsive" start up. (i.e., the cone is brought from rest to free stream velocity instantaneously). The outer and inner boundary conditions were maintained throughout the calculation.

In summary, a means of reducing the field of calculation by half through symmetry has been discussed. The requirements for boundary conditions were shown and the manner in which these requirements were satisfied in the present study was presented. The use of the θ momentum equation to obtain the cone surface pressure was demonstrated and the initial conditions utilized were also discussed.

APPENDIX B

NORMAL STRESS DAMPING

Previous studies (References 13, 25) using shock capturing finite difference techniques have encountered oscillations in the vicinity of strong shock waves which can cause solution instabilities. To overcome this difficulty, artificial terms have been added to the governing equations to provide necessary damping. In the present study, using the viscous equations and shock capturing, oscillations were again encountered. This indicated that the natural viscous terms are inadequate to overcome the series truncation error at the existing mesh spacing. To damp these oscillations without additional programming complexity, the normal stress terms (which are in general large only near shock waves) were altered by increasing the second coefficient of viscosity ($\lambda \geq -2/3\mu$). This resulted in elimination or reduction of the oscillations where desired. In addition to improving the shock structure, it was found that normal stress damping was extremely effective in removing instabilities caused by starting transients which result from ill-suited initial conditions. The details of implementation and conditions for proper use of this technique are given below.

As shown in Equation 4, the normal stress terms contain:

$$\sigma_n = \lambda_{Re} (\nabla \cdot \vec{v}) = -\frac{2}{3Re} \left[2u \sin\theta + \frac{\partial}{\partial\theta}(v \sin\theta) + \frac{\partial w}{\partial\phi} \right] \qquad (16)$$

Normal stress damping results when $2u \sin\theta$ is removed and the remainder of the term is multiplied by an empirically determined factor β, where β is negative (i.e. $\beta\sigma_n$). (A positive β does not produce the damping effect and makes the calculation unstable except near $\beta = 1$). The damping terms occur both in the energy equation and in the $\vec{H}'$ matrix resulting from the coordinate transformation. It was found that the most accurate solutions resulted from use of the damping multiplier in the derivative term only ($\vec{F}_\theta$ or $\vec{G}_\phi$) of the momentum equation most nearly normal to the shock wave for which damping is desired. Inclusion

AD-A042 072 AIR FORCE FLIGHT DYNAMICS LAB WRIGHT-PATTERSON AFB OHIO F/G 20/4
THE CONICALLY SYMMETRIC NAVIER STOKES EQUATIONS: NUMERICAL SOLU--ETC(U)
MAR 77 D S MCRAE

UNCLASSIFIED AFFDL-TR-76-139 NL

2 OF 2
ADA042072



END
DATE FILMED
8-77

of the multiplier in the $\vec{H}'$ matrix or the energy equation produced some displacement of the solution. Also, it should be noted that in the steady limit,

$$\sigma_n = f(\nabla \cdot \vec{v}) = f(\vec{V} \cdot \frac{\nabla \rho}{\rho}) \tag{17}$$

(through use of the continuity equation). This implies that normal stress damping cannot be used in the vicinity of compressible flow boundary layers without regard for possible changes in the density gradients.

An example of the use of normal stress damping is given in Figure 34 for axisymmetric cone flow as calculated by the technique of this report. The plot is a comparison of the calculated static pressure in the θ direction at Tracy's free stream conditions with and without the inclusion of normal stress damping. In this case the damping is tailored in the θ direction by:

$$\beta = 1 - (\frac{P_s}{P_\infty})\, A1 - (\frac{P}{P_\infty})\, A2 \tag{18}$$

where the pressure ratio multipliers were empirically determined to be A1 = 9 and A2 = 2. The use of the damping multiplier (Figure 34) resulted in the reduction of the numerical oscillations near the shock wave. Although a small offset in pressure occurs outside the boundary layer, the surface pressure and shock position do not change appreciably when damping is applied.

For Tracy's cases, the damping multiplier β was unity over the lee 40° (ϕ = 140° - 180°) of the flow, where viscous effects predominate. It was then varied smoothly around the cone from ϕ = 140° in accord with the equation:

$$\beta_\phi = 1 - \beta' \left[\frac{P_s|_\phi - P_s|_{\phi = 140°}}{P_s|_{\phi = 0°} - P_s|_{\phi = 140°}} \right]^{1/2} \tag{19}$$

where s indicates body surface values and β' was empirically varied from 15 (α = 8°) to 130 (α = 24°). β was constant in the θ direction.

For Stetson's case, the very strong lee side expansion during start up made it necessary to use normal stress damping there. However, the damping in this region was removed after the solution development was sufficient for the expansion to become less strong. For the rest of the field ($\phi = 0° \rightarrow 140°$), a more sophisticated tailoring of the damping multiplier was used:

$$\beta_{\theta,\phi} = 1 - \left[\frac{P_s|_{\phi} - P_s|_{\phi = 140°}}{P_s|_{\phi = 0°} - P_s|_{\phi = 140°}}\right]^{1/2} \left[\frac{P|_{\phi = 0°}}{P|_{\phi = 140°}}\right]^{co1} - \left[\frac{P|_{\phi,\theta}}{P_\infty}\right]^{co2} \tag{20}$$

The value of co1 was 1.6 and of co2 was 1.1. This equation was based on experiments with the use of normal stress damping which showed that the effects could be improved by tailoring according to the local value of static pressure. An improvement was noted in the damping effect, but it was found that this equation did not always increase the magnitude of β quickly enough during initial start up. This was overcome by using a high initial magnitude of β for approximately the first 100 time steps of the run. The above equation was used for McElderry's case also. However, the value of β necessary on the lee side was more negative than the output of the above equation. The high initial magnitude was therefore used everywhere in the flow field.

In order that others who use normal stress damping may benefit from experience gained in the present study, the following observations and rules concerning this technique are offered:

(1) The most valuable and recommended use of normal stress damping is to reduce starting transients from ill-suited initial conditions. No permanent history of the use of damping for this purpose is seen in the flow after the removal of the damping and subsequent convergence.

(2) Normal stress damping has been used to allow capturing of shock waves with p_2/p_1 as high as 32. The only practical limit to shock strength which can be captured through use of this technique appears to be number of mesh points available for the smearing to take place over.

(3) Tailoring of the damping based on local static pressure was found to give reasonable results. Tailoring based on other quantities (such as temperature) gave unnecessary offset in the viscous layer.

(4) Large shifts of surface pressure or of static pressure behind shocks when damping is applied usually indicate that the magnitude of β is too high in that locale.

(5) The best results are obtained behind the shock wave when some oscillations are allowed to remain in the free stream.

(6) Care must be taken to ensure that the viscous stability limit is satisfied with β included in the manner shown in Appendix C.

(7) The items noted below are observed to cause undue displacement of the solution at high values of β:

(a) Inclusion of the β multiplier in terms resulting from coordinate transformations (i.e., the $\bar{H}'$ matrix).

(b) Inclusion of β in the energy equation.

The previous observations and rules should not be considered as axiomatic but are offered as guides for the use of this technique in other compressible flow problems.

Normal stress damping is a physically based technique which has proven beneficial in damping out starting transients and smoothing numerical oscillations in the vicinity of shock waves. The β contouring equations and levels used for the various cases were presented. Rules and observations were also given to guide future use of this technique.

APPENDIX C

STABILITY CRITERIA

In order to maximize computational efficiency, criteria should be used to determine the maximum permissible time step (Δt) as the integration progresses. As noted in Section III, criteria were not used during the calculations presented elsewhere in this report. Instead, Δt was fixed during each complete integration at Tracy's conditions and was fixed for the later parts of the integrations at Stetson's and McElderry's conditions. The value at which Δt was fixed was at first determined by increasing Δt until instability was encountered during the starting transient phase of the run. The run could then be continued to convergence by reducing Δt 10% to 15% from the unstable value. As experience was gained with the technique (and more was learned about the effect of normal stress damping on stability), it was found that for Tracy's conditions, stable values of Δt could be set initially without resorting to trial and error. These values were in general $0.6\Delta\theta$ to $0.7\Delta\theta$. The above procedure did not, however, allow for any possible increase in allowable Δt after the large transient phase of the calculation. Difficulty in determining allowable Δt was also encountered for Stetson's and McElderry's conditions due to use of normal stress damping in predominately viscous regions. To correct these two deficiencies, stability criteria for use during the integration were postulated and confirmed by a repeat of previous calculations. The remainder of this appendix will present this procedure and the observed changes in computational efficiency.

A complete stability analysis for MacCormack's method as applied to the Navier-Stokes equations has not been accomplished. However, useful estimates of allowable step sizes can be made through the use of linear theory and physical arguments. Claiming that the physical

propagation of information (i.e. fluid signals) cannot outstrip the numerical propagation results in the following Courant-Friedrich-Lewy (CFL) condition (Reference 36):

$$\Delta t_{cfl} \leq \frac{1.0}{\frac{|v|}{\Delta\theta} + \frac{|w|}{\sin\theta\,\Delta\phi} + c\frac{[\Delta\theta^2 + (\sin\theta\,\Delta\phi)^2]^{1/2}}{\Delta\theta(\sin\theta\,\Delta\phi)}} \tag{21}$$

This expression essentially determines allowable Δt in regions where viscous effects are negligible. The remaining task is to determine the effects on stability of the stress terms and of normal stress damping.

The maximum stable Δt in viscous regions is normally a function of the smallest physical step size there. In the present study $\Delta\theta << \Delta\phi$ for all cases calculated. This implied that the stress terms in the θ coordinate direction were the main determinant of allowable Δt and therefore that the stability analysis due to the stress terms was essentially a one-dimensional problem. In the case of finite difference operator time splitting, the stability analysis also has been shown to be a one-dimensional problem (Reference 25). An analysis similar to that of Reference 25 was therefore accomplished and is presented here.

Equation 22 is first written in nonconservation form:

$$[L][Z]_t + [M][Z]_\theta + [N][Z]_\phi + [W][Z]_{\theta\theta} + [Q][Z]_{\phi\phi} + [S][Z]_{\theta\phi} + [X][Z]_{\phi\theta} + [H'] = 0 \tag{22}$$

where $[Z] = \begin{bmatrix} \rho \\ u \\ v \\ w \\ p \end{bmatrix}$ and the subscripts indicate differentiation.

The remaining matrices will be defined as they are used. The final equation results when $[L]^{-1}$ is found and the coefficient matrices $[L]^{-1}[M]$, etc. are formed. By declaring the coefficient matrices to be locally constant, it can be shown that (References 37, 38) when each dimension is

considered separately $\nu \frac{\Delta t}{\Delta\theta} \leq 1.0$ (inviscid effect) and $\nu \frac{\Delta t}{\Delta\theta^2} \leq \frac{1}{2}$ (viscous effect). The symbol ν is in each case the maximum eigenvalue of the appropriate coefficient matrix (for example $[L]^{-1}[M]$). Equation 21 accounts for the inviscid effect on stability so that it is only necessary to consider the second inequality and obtain values of ν for the coefficient matrices of the second derivative terms involving θ in Equation 22.

The matrix $[L]^{-1}[W]$ is as follows:

$$[L]^{-1}[W] = \begin{bmatrix} 0 & 0 & 0 & 0 & 0 \\ 0 & \frac{1}{\rho Re} & 0 & 0 & 0 \\ 0 & 0 & \frac{2 + \frac{\beta\lambda}{\mu}}{\rho Re} & 0 & 0 \\ 0 & 0 & 0 & \frac{1}{\rho Re} & 0 \\ -\frac{2\gamma p}{2\rho^2 RePr} & 0 & 0 & 0 & \frac{\gamma}{\rho Re\ Pr} \end{bmatrix} \qquad (23)$$

The maximum eigenvalues of this matrix are $\gamma/(\rho Re\ Pr)$ and $(2 + \frac{\beta\lambda}{\mu})\ /(\rho Re)$. The second eigenvalue is included due to the undetermined (and sometimes large) value of the damping coefficient β.

Arguments must now be made regarding contribution of the $\theta\phi$ and $\phi\theta$ cross derivative terms in the equation set. The goal is to demonstrate that the eigenvalues of $[L]^{-1}[W]$ give a minimum Δt, so that the $\theta\phi$ and $\phi\theta$ terms can be dropped from consideration. First, assume that the contribution of these terms is $\nu \frac{\Delta t}{\Delta\theta^2} \leq \frac{1}{2}$. This effectively increases the contribution (results in a lower Δt) of these terms since $\Delta\theta << \Delta\phi$. As an example, the matrix $[L]^{-1}[X]$ is

$$[L]^{-1}[X] = \begin{bmatrix} 0 & 0 & 0 & 0 & 0 \\ 0 & 0 & 0 & 0 & 0 \\ 0 & 0 & 0 & \frac{\beta\lambda/\mu}{Re} & 0 \\ 0 & 0 & \frac{1}{\rho Re} & 0 & 0 \\ 0 & 0 & 0 & 0 & 0 \end{bmatrix} \qquad (24)$$

The maximum eigenvalue of this matrix is $(\beta\lambda/\mu)^{1/2}/(\rho Re)$ and is clearly less than the eigenvalue due to normal stress damping of the $[L]^{-1}[W]$ matrix. Since the$[L]^{-1}[S]$matrix is similar, it can be concluded that sufficient information is known to postulate a complete stability criteria. By substituting the eigenvalues into the appropriate stability criteria and labeling each resulting Δt as to its source, the following complete stability criteria is postulated:

$$\Delta t = m \min (\Delta t_{cfl}, \Delta t_{nsd}, \Delta t_{visc}) \tag{25}$$

where $m \leq 1.0$, Δt_{cfl} = min of results from Equation 21

$$\Delta t_{nsd} = \min \frac{\rho Re \ \Delta\theta^2}{2 \left| (2+\frac{\beta\lambda}{\mu}) \right|}$$

$$\Delta t_{visc} = \min \frac{\rho Re \ Pr \ \Delta\theta^2}{2 \gamma}$$

where min implies the minimum value of the quantity found by searching all mesh points in the flow field. The factor m is theoretically limited to a value of 1.0. However, uncertainties and approximations in the stability analysis sometimes result in an actual maximum value of m greater or less than 1.0.

The above procedure was tested at $\alpha = 0°$ for Tracy's conditions with good results. However, the real issue was whether the criteria would be adequate for high α with the use of large amounts of normal stress damping. Therefore, the $\alpha = 20°$ case at Tracy's conditions was repeated with the above criteria for determining Δt in continuous use. Use of the criteria reduced the number of time steps necessary for convergence to the fifth significant digit from 1700 to 960. The factor m for this run was 1.0 for the first 300 time steps and 1.2 thereafter. Instability of the solution occurred for m = 1.4. The values of the normal stress damping coefficient (β) were comparable with those used in the original run. In order to ensure that the viscous stability limit would not be violated when using very high values of normal stress damping, a run was

made at Tracy's conditions and $\alpha = 0°$ with $\beta = 4000$. This set of conditions was unstable at a value of Δt determined from Equation 21. However the use of the above criteria reduced the value of Δt sufficiently to allow the run to be continued (although at a very low Δt).

In summary, stability criteria were postulated and confirmed which reduced the number of time steps required for convergence by 44% in an example calculation. The procedure was also shown to account for the effects of normal stress damping on stability.

☆ U. S. GOVERNMENT PRINTING OFFICE: 1977 — 757-001/528